SOUTHWEST RESEARCH INSTITUTE®

6220 Culebra Road
San Antonio, Texas 78238
DUNS Number 00-793-6842

DIGITAL TWIN MODEL FOR ADVANCED MANUFACTURE OF A ROTATING DETONATION ENGINE INJECTOR

Principal Investigator (PI):

Shane B. Coogan
Lead Engineer
shane.coogan@swri.org
210-522-2774

Team Members:

Southwest Research Institute
Aerojet Rocketdyne
Georgia Institute of Technology

FINAL TECHNICAL REPORT
DOE Award FE0031644
SwRI Project No. 18-24185
Project Period: October 1, 2018 – September 30, 2021

Prepared for:

U. S. Department of Energy (DOE)
Office of Fossil Energy (FE)

December 17, 2021

Approved:

Ben H. Thacker, Ph.D., P.E.
Vice President
Mechanical Engineering Division

KEY CONTRIBUTORS

Key Contributors to the Project Listed Alphabetically by Last Name		
Name	**Organization**	**Responsibilities**
Shane Coogan	Southwest Research Institute	Principal investigator
Ron Daniel	Aerojet Rocketdyne	Additive manufacturing support
Sanam Gorgannejad	Georgia Institute of Technology	Material model development, microstructure characterization, and high cycle fatigue tests
John Macha	Southwest Research Institute	Metallurgical analysis of tensile test specimens
Rick Neu	Georgia Institute of Technology	Material model development, microstructure characterization, and high cycle fatigue tests
Carl Popelar	Southwest Research Institute	Additive manufacturing support and tensile tests
James Sobotka	Southwest Research Institute	Materials literature review
Jeffrey Stout	Aerojet Rocketdyne	RDE injector design, additive manufacturing support, and RDE test operations
Steve White	Southwest Research Institute	RDE injector design and RDE test operations

ACKNOWLEDGEMENT OF SUPPORT

This material is based upon work supported by the Department of Energy under Award Number(s) DE-FE0031644.

TABLE OF CONTENTS

LIST OF FIGURES

LIST OF TABLES

1. EXECUTIVE SUMMARY

A digital twin material model (DTMM) of an additive manufacturing (AM) process was created to advance the state of the art in rotating detonation engine (RDE) injector design. Current RDE injectors are designed with large pressure drops, enabling a stable and repeatable combustion process. However, this comes at the cost of system efficiency. For the technology to transition to commercial fossil-based power generation, it is important to develop injectors with reduced flow losses. Low-loss injectors are difficult to design and manufacture with conventional manufacturing techniques. AM enables new design options, but the AM manufacturing process must be thoroughly understood to result in a robust design. A DTMM provides the necessary insight by defining the cause-effect relationships between process parameters, microstructure features, and properties. Therefore, a DTMM to support the design and manufacturing process was developed and applied to the design of a new additively manufactured low-loss injector. The injector combustion behavior was characterized through hot-fire tests, and mechanical performance was compared to the DTMM predictions.

The two project goals were the successful development of the DTMM and the demonstration of an improved RDE injector design. The RDE injector design and DTMM developments occurred on parallel but dependent paths. The injector was designed to reduce pressure drop by increasing the cross-sectional flow area ratio between the injector air passages and the combustor annulus. This resulted in less structural material, raising the concern that thin members would be susceptible to high-cycle fatigue (HCF) under the periodic loading inherent to an RDE. It was most important for the DTMM to predict behavior in these features; therefore, the injector design concept guided the material thicknesses used in fatigue tests.

The DTMM development started by manufacturing a series of coupons over the range of possible AM process variations. A design-of-experiment approach was used to select which process variable combinations gave the most efficient coverage relevant to the injector design space. The microstructure in each of these coupons was characterized, and then computational methods were used to create a numerical model of the correlation between process variables and microstructure. Next, a set of HCF samples were tested to calibrate existing models that map microstructure to HCF performance. Together, these two links formed the DTMM that calculates HCF behavior from AM process variables.

Two injector prototypes were additively manufactured. The first injector design strategy aggressively pursued low-loss performance by substantially increasing the oxidizer flow area. The combination of manufacturing lead times and the fatigue testing schedule meant that the DTMM was not available when building this first prototype. Therefore, its process parameters were chosen based on a manual review of the available coupon data. This prototype was built successfully and evaluated in 58 combustion tests. Sustained detonation was achieved with remarkably reduced pressure loss, and some tests even displayed pressure loss characteristics similar to conventional gas turbine combustors. This achieved the project goal of improving RDE injector design.

The second injector was manufactured according to the optimized parameters predicted by the DTMM. The flow area modifications of this injector were less aggressive than the first injector since demonstrating low pressure loss was not an objective of the second hot-fire test series. Rather, the test objective was to cause high cycle fatigue failure in the part due to periodic loading from the rotating detonation wave. The observed number of cycles to failure was to be compared to the number predicted by the DTMM and thereby assess the utility of the DTMM in component design. However, the required level of vibration was not obtained during combustion. Therefore, high cycle fatigue was not experienced in the hot-fire tests of the second injector.

Fatigue data was obtained by further testing the second injector in a conventional HCF test apparatus. The injector demonstrated HCF strength above the DTMM prediction. In fact, it did not fail and testing was only discontinued due to reaching the end of the period of performance. This points to some success in the project's primary goal of successfully developing and applying the DTMM to a component design.

Implementing the DTMM recommendations for optimal processing parameters led to a part with acceptable properties. The DTMM was also shown to be an efficient correlator of data and to provide insight into the relationship between process settings, microstructure, and property performance. However, the failure of the DTMM prediction to match the experimental result of the injector fatigue test also points to the need to include significantly more data in the model development.

In this project, coupons made with identical processing parameters exhibited drastically different properties from each other and from the injector part, which clearly influences the accuracy of a model that predicts performance based on parameters. Uncertainties in the build process must be quantified to develop more robust models. A denser and broader matrix of coupon process and geometry variations, several repeated builds of every point, more in-situ build process measurements, and direct observation of tensile and HCF sample microstructure (as opposed to separate microstructure specimens) are recommendations to improve future AM modeling efforts.

2. INJECTOR DEVELOPMENT

A. DESIGN

Demonstrating the operation of a low-loss RDE injector was one of two project objectives. An RDE is a type of pressure gain combustion device. Unlike a conventional gas turbine combustor (Brayton cycle) where total pressure is reduced during combustion, an RDE uses detonation waves to increase the total pressure during combustion. A complete RDE consists of an isolator, injector, combustor, diffuser, and bypass mixer, as summarized in Figure 1. Historically, the gain in total pressure that occurs in the combustion chamber due to the detonation process is more than cancelled by the total pressure losses in the ancillary components upstream and downstream of the combustor itself. These other components must be improved to realize the promise of pressure gain combustion. A previous Department of Energy project led by Aerojet Rocketdyne made progress in the diffuser design. This project focused on reducing the pressure losses in the upstream injector component.

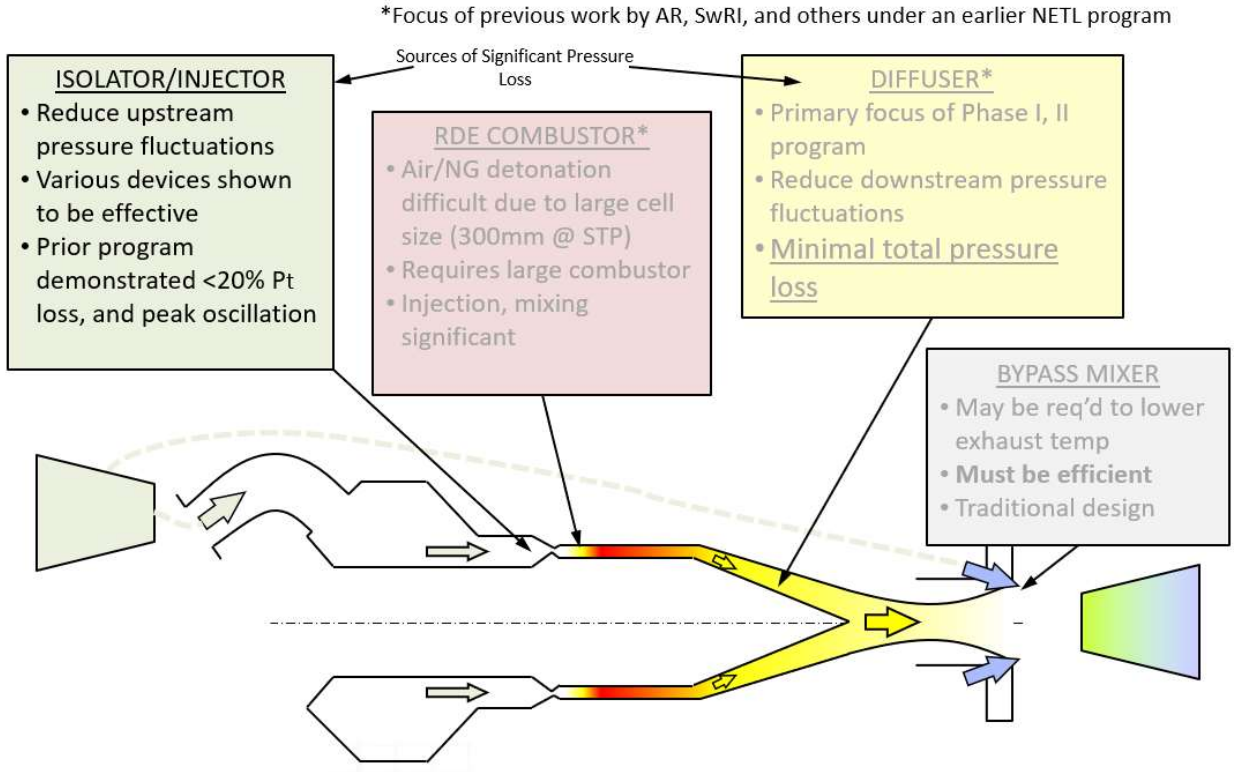

Figure 1. Components of a Rotating Detonation Engine (RDE)

The conceptual layout of the RDE is shown in Figure 2. Gaseous oxidizer (oxygen-enriched air in this project) and gaseous fuel (hydrogen in this project) are supplied to manifolds located in the upstream flange. These reactants then flow through injector passages that discharge into the annular combustion chamber in a manner that promotes detonation. In this project, the injector implemented aggressive mixing geometry that was enabled by additive manufacturing. The resulting design could not have been manufactured by conventional methods as a single part. These aggressive mixing features allow for a lower velocity oxidizer flow through the injector (as opposed to the choked flow of legacy designs) which in turn lowers the pressure losses. The detailed injector design is not being made public at this time, therefore further description is omitted from this report.

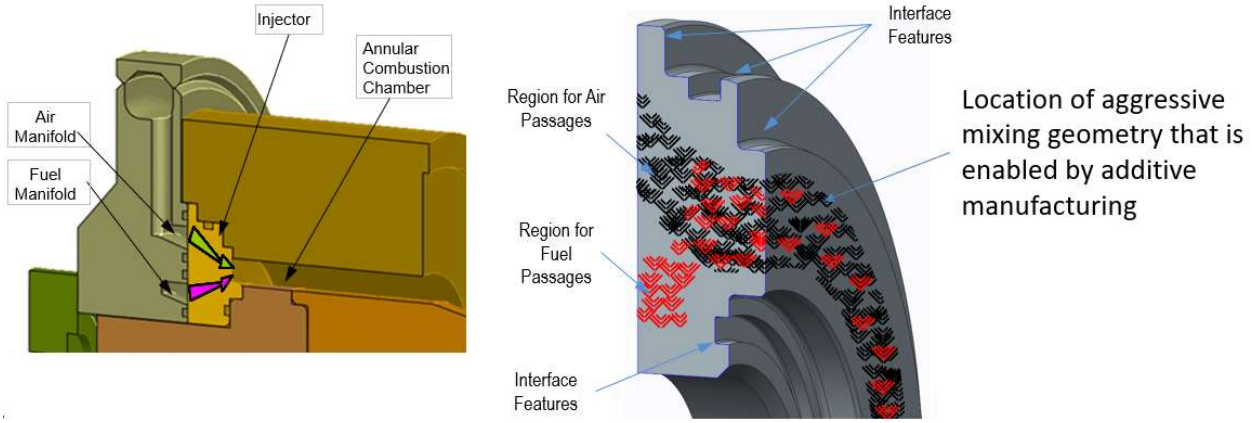

Figure 2. The RDE Injector Concept

The combustion process in an RDE is inherently periodic. One or more detonation waves spiral around the combustion annulus. When there is only one wave, this results in an unbalanced pressure impulse on the centerbody, as shown in Figure 3. The wobbling of the centerbody transfers a moment back to the injector that stresses features in the fuel and oxidizer passages. Furthermore, the detonation wave revolves at an approximate frequency of 5 kHz. An RDE rapidly accumulates load cycles, particularly in the context of long-term power generation. These factors combine to create a high cycle fatigue concern in the injector. Therefore, the material model discussed in section 3 focused on predicting fatigue strength.

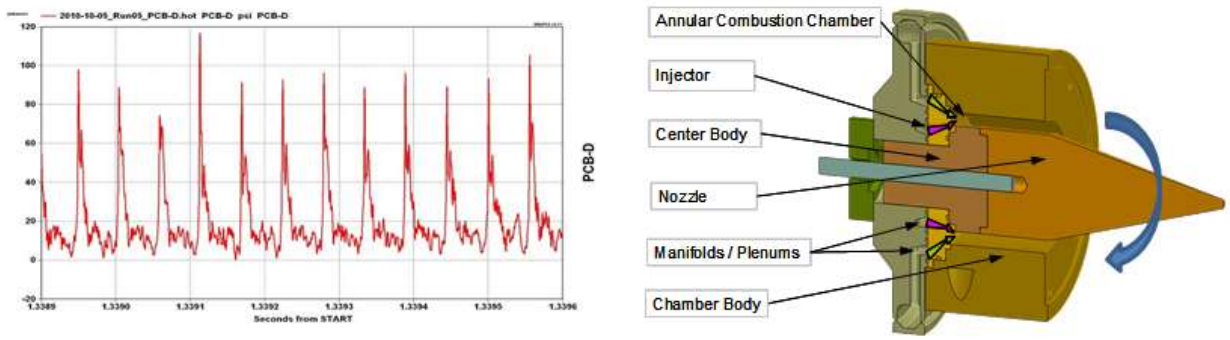

Figure 3. Unbalanced Pressure Oscillations in the RDE Create a High Frequency Wobbling Motion that Transmits Loads to the Injector

During the design process it was discovered that it is actually difficult to generate appreciable stress in the RDE injector from the centerbody wobble. This is because typical test hardware uses a thick-walled copper alloy part for thermal management purposes. The mass of this component lowers the structural natural frequency to such a degree that it filters out the high frequency forcing of the detonation wave, and little motion is actually transferred to the injector. Nonetheless, this project aimed to compare component performance to the material model prediction. Therefore, a fatigue condition was designed into the system by shortening and thinning the centerbody as shown in Figure 4. An adjustable tuning ring was also included to adjust the structural frequency and better align it with the detonation frequency.

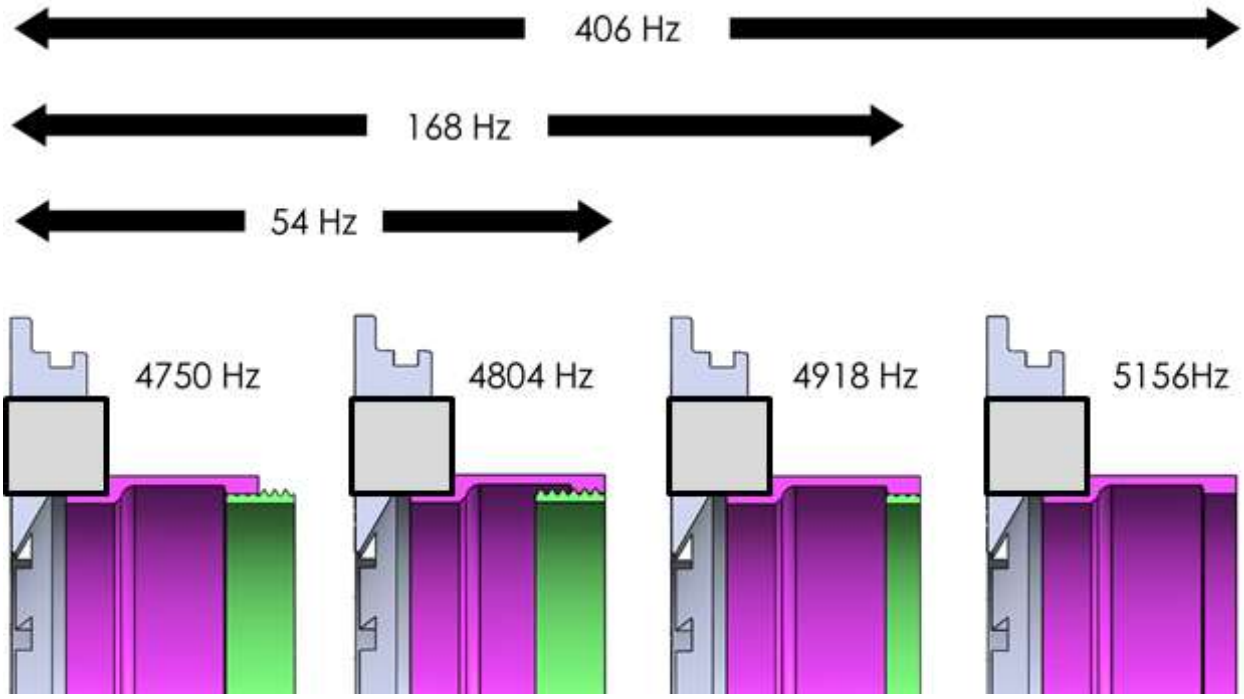

Figure 4. A Shortened Dynamic Centerbody with an Adjustable Tuning Ring Aligns the Structural Natural Frequency with the Detonation Frequency

The maximum principal stress in the injector occurred at a single well-defined point located in a transition fillet. As shown in Figure 5, the injector was designed to fail in fatigue within the planned hot-fire tests so long as the detonation frequency was aligned with the structural frequency, structural damping was less than or equal to 2%, and the fillet radius was less than or equal to 0.02 inches. Modal testing confirmed a damping ratio of less than 1%, and the injector design used a 0.02-inch fillet. Therefore, fatigue failure was anticipated during the hot-fire tests.

Two variants of the injector were designed to operate with the 10-cm diameter RDE provided by Aerojet Rocketdyne. Both implemented the same mixing architecture, but Injector #1 fully pursued low-loss performance while Injector #2 choked the oxidizer flow to possibly give more reliable detonation. The approach was to fire Injector #1 a few times to assess operability and pressure loss characteristics and thereby satisfy the objective of improving RDE injector design. Injector #2 was then to be fired repeatedly to develop high cycle fatigue damage for comparison to model predictions in order to satisfy the second objective of evaluating the material model.

The material for both injectors is a proprietary version of Inconel 625. Inconel 625 was selected as the material due to its suitability for combustion applications, its prevalence in the materials literature, and its availability at Aerojet Rocketdyne.

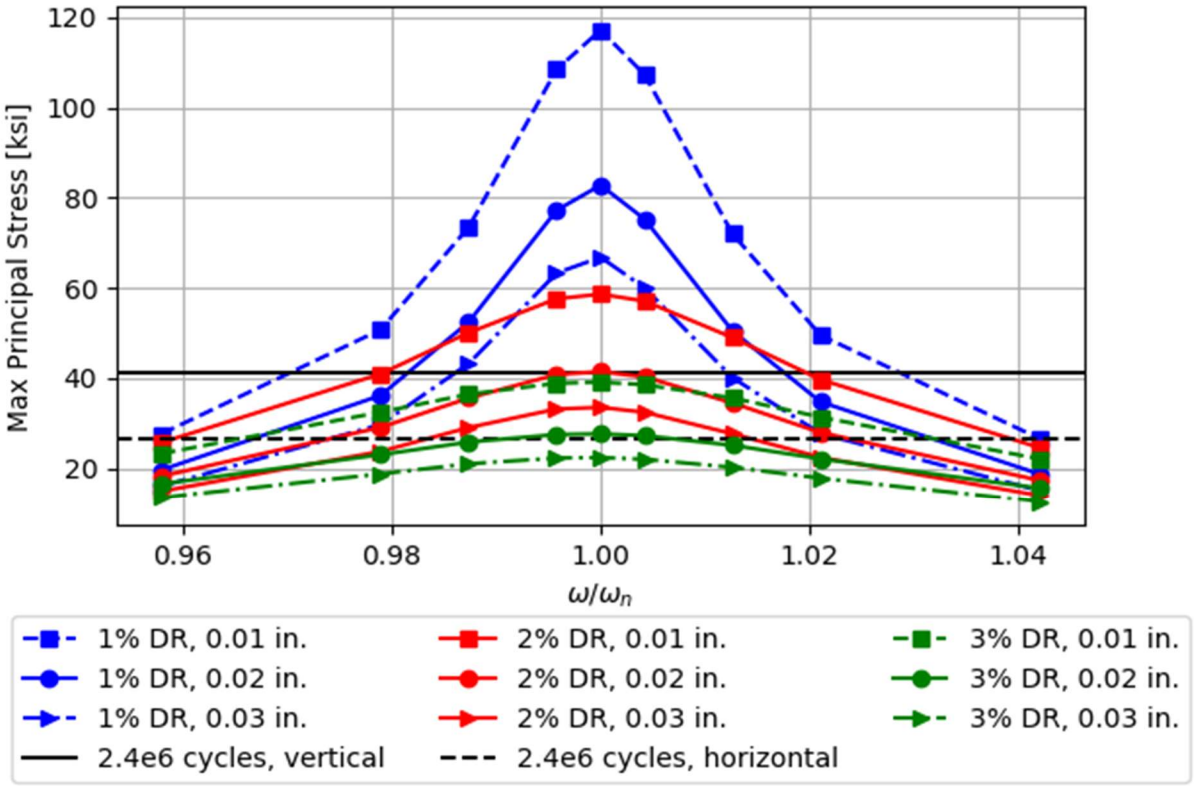

Figure 5. Stress was Estimated to Exceed the Fatigue Strength for the Anticipated Number of Hot-Fire Cycles when the Wobble Mode is Excited Near Resonance (Horizontal Lines are Estimates of Fatigue Strength for Different Build Directions)

B. MANUFACTURING

The two injector prototypes were manufactured on the Concept M2 machine at Aerojet Rocketdyne. Injector #1 was built first and used the process parameters from sample build 2 (see section 3.C of this report). These process parameters were selected based on a subjective review of the material property data available because the initial version of the DTMM was not yet complete. This was acceptable because the objective for the Injector #1 tests was to demonstrate performance and operability of the low-loss injector design.

Injector #2 was built after the hot-fire testing of Injector #1 and it used the process parameters from sample build 3. These parameters were selected based on the DTMM predictions for optimum fatigue strength (see section 3.K). Thus, the mechanical performance of Injector #2 is an indicator of the utility of the DTMM in component design.

The injectors were used in as-built condition, with clean-up machining only applied to mating surfaces. The as-built dimensions of key internal features were evaluated in Injector #1. The fillet radius that defined the expected fatigue location was within 0.002 inches of target (nominal dimension of 0.02 inches), and the internal fuel passage diameters were also within 0.002 inches of target. Injector #1 shrank considerably during the hot-isostatic-pressing (HIP) treatment, with global shrinkage around 8%. Therefore, mating features should be oversized in additive manufacturing builds to ensure that sufficient material remains for clean-up machining (the relevant features of the injector were appropriately oversized in this case).

While additive manufacturing enables more complex internal geometries, the removal of build supports was found to be a challenge. Part designs must carefully consider build support locations to avoid labor-intensive clean-up operations.

C. HOT-FIRE TESTS

C.1 INJECTOR #1

Hot-fire tests of Injector #1 were performed at the Southwest Research Institute (SwRI) RDE test facility during the week of March 8th. A total of 64 tests were attempted over 3 ½ days. Fifty-eight of the 64 tests achieved combustion, with three of the six failed ignitions known to be caused by faulty spark plugs that were replaced. The team demonstrated a high experimental throughput – up to 28 tests were performed in a single day.

The RDE operating with sustained detonation is shown in Figure 6 and Figure 7. The fuel was hydrogen and the oxidizer was oxygen-enriched air. While hydrogen-air flames are theoretically invisible, there are sufficient impurities in the system to illuminate the exhaust plume. Rotating shockwaves are visible against the backdrop of the static centerbody, particularly in the night view.

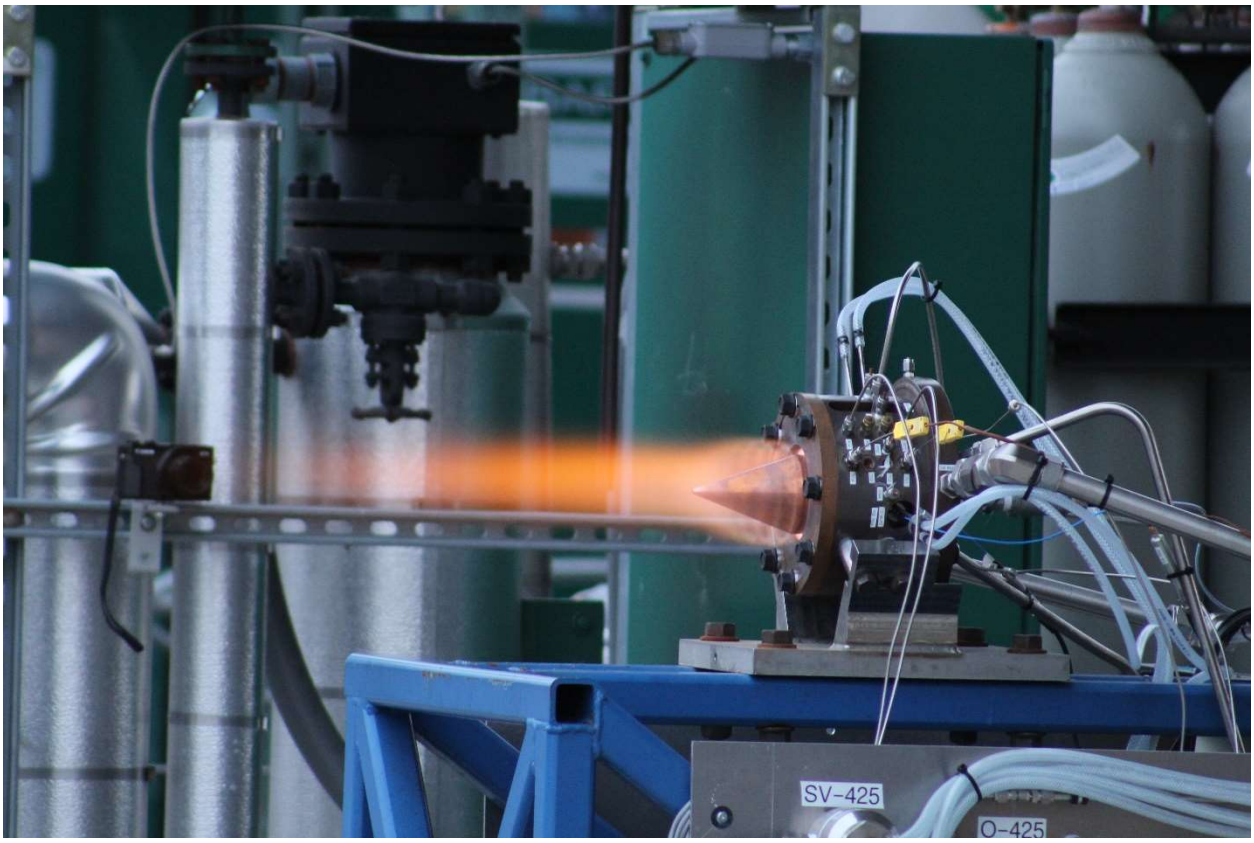

Figure 6. Exhaust Plume of a Hot-Fire Test of Injector #1, Day View

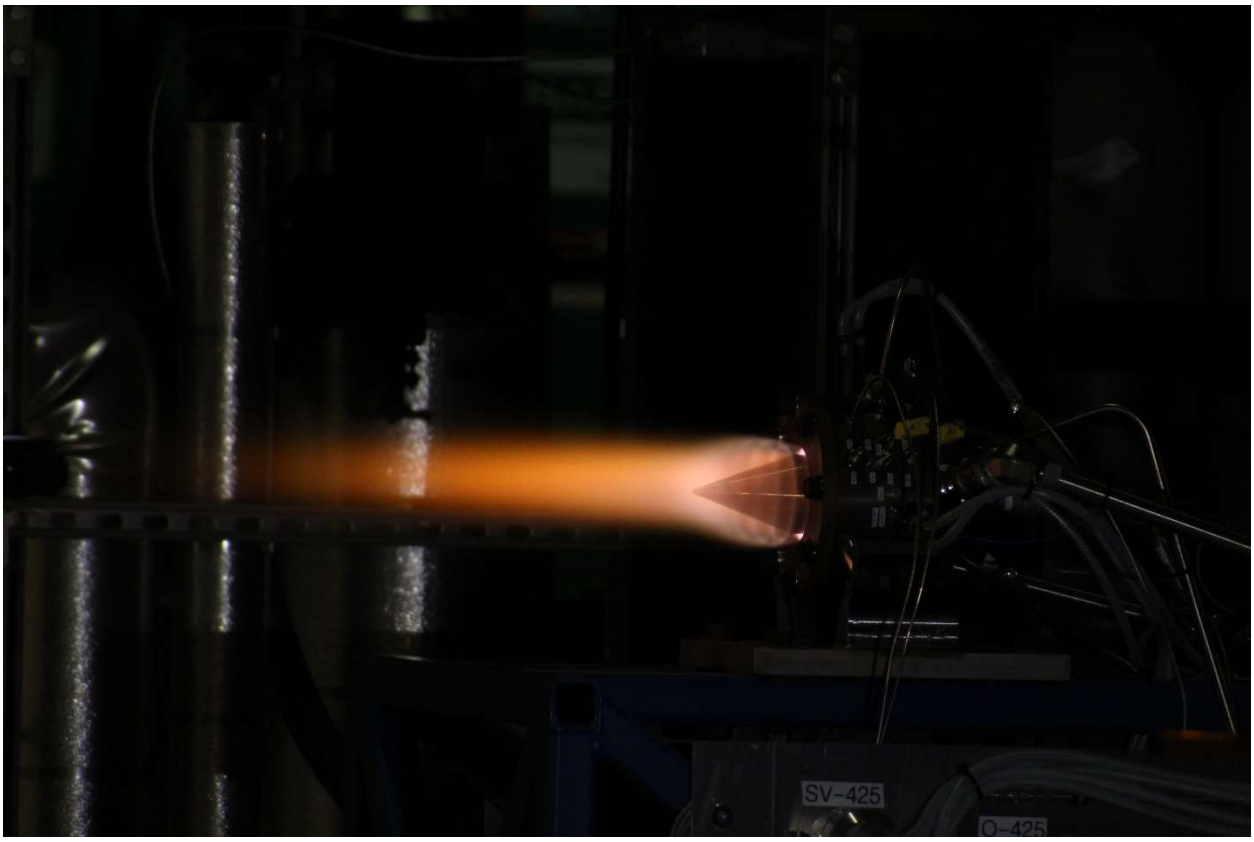

Figure 7. Exhaust Plume of a Hot-Fire Test of Injector #1, Night View

The test matrix varied the total mass flux, oxygen concentration in the oxidizer, equivalence ratio, and area contraction ratio of the nozzle backpressure plate. The dynamic pressure data from each test were reviewed to classify the combustion as detonation or deflagration. Single-wave detonation generates sharp, evenly spaced pressure pulses. This is in stark contrast to deflagration or possibly irregular detonation, where the oscillation in the pressure signal appears random and of relatively small amplitude.

The RDE is only considered operable at test points with sustained detonation, as this is what generates the gain in total pressure across the combustion chamber. Of the 58 combustion tests, 62% (i.e., 36 of 58) achieved sustained detonation, with the remainder burning through deflagration. The large number of detonation points confirms that the low-loss design is a viable RDE injector. Of the 36 tests with detonation, 72% (i.e., 26 of 36) operated with a single wave. Single-wave operation was desirable in this program because the unbalanced pressure pulse was needed to excite the wobble mode in the dynamic centerbody.

The injector pressure loss was calculated from the difference of the oxidizer manifold static pressure and the average of two static pressure measurements in the combustion chamber. Every test gave a different absolute and relative value of pressure loss across the injector due to the varying conditions between tests. The injector pressure recovery ratio, which is the ratio of chamber pressure to manifold pressure, is used as the performance metric; this value should be as close to unity as possible.

A pressure recovery ratio of 0.7 was selected as the low-loss threshold. Any performance above this value is considered low-loss because the injector is not choked, meaning the oxidizer flow is always subsonic and influenced by downstream pressure oscillations. All detonation points exceeded this performance goal with the data centered around a value of 0.90. While the pressure loss varied with configuration, the lowest pressure loss test with detonation had a pressure ratio of 0.964 (only a 3.6% pressure loss). In summary, Injector #1 was demonstrated to be operable with low pressure losses, and in some cases the pressure loss was minimal and comparable to a conventional gas turbine injector.

The desired vibration of the injector was not demonstrated in the hot-fire testing of Injector #1. Some tests caused notable deflection in the dynamic centerbody as measured by a proximity probe, but this vibration occurred at four times the detonation frequency. The tendency for the RDE to subharmonically excite shell modes is illustrated in Figure 8. This thought experiment assumes that the detonation pressure pulse is located at top center at the initial time, and this corresponds to a downward deflection of the centerbody shell. The next frame shows the location of the pressure pulse at a time that is one half period later in the structural mode oscillation. It is evident that harmonic excitation of shell modes is self-cancelling. If the pressure pulse is at a trough at the initial time, it is at a peak at a later time, and there is negative interference. In contrast, subharmonic excitation, specifically at a fraction that is one over the number of lobes, consistently aligns the pressure pulse with the trough. The trough rotates around the circumference at the same rate as the detonation wave, and the proximity probe sees an oscillation at 4x the detonation frequency as four peaks and four troughs move past its location in one revolution of the detonation wave.

In conclusion, hot-fire testing of Injector #1 only excited high frequency shell modes, and did not excite the primary wobble mode. These shell modes do not generate stress in the injector.

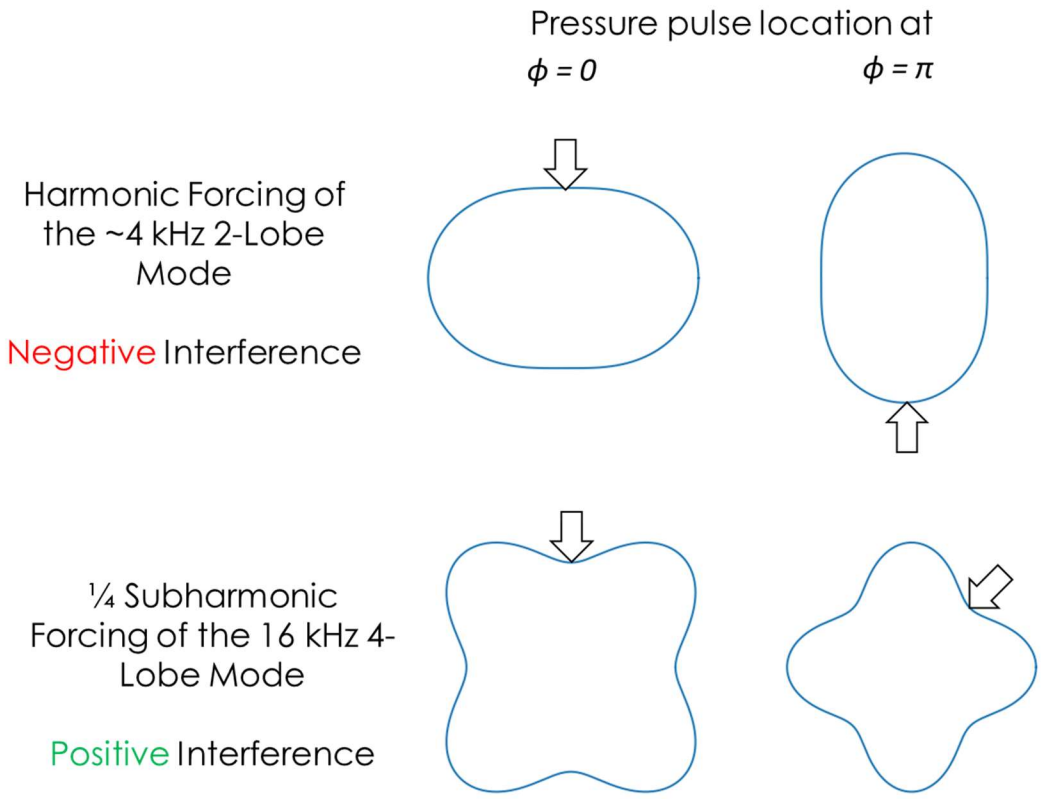

Figure 8. Mode Excitation Potential of Harmonic Forcing of a 2-Lobe Mode Compared to ¼ Subharmonic Forcing of a 4-Lobe Mode

C.2 INJECTOR #2

Hot-fire tests of Injector #2 were performed at the SwRI RDE test facility during the week of August 9th. The primary objective was to align the detonation frequency with the natural frequency of the wobble mode and generate fatigue damage through repeated runs at this condition. Life of the part was then to be compared to DTMM predictions. The assembled RDE with Injector #2 is shown in Figure 9.

A total of 28 tests were attempted over 1 ½ days. Twenty-five of the 28 tests achieved combustion, with two of the three failed ignitions known to be caused by an incorrect setting of a pressure regulator. As with Injector #1, the team demonstrated a high experimental throughput – up to 22 tests were performed in a single day. The injector could have been forced through a very large number of cycles over the planned two-week testing effort. However, hot-fire tests were discontinued after the second day due to inadequate vibration.

The vibration measured by the proximity probe indicated that the wobble mode was harmonically excited at the detonation frequency, as intended. However, the measured deflection amplitude of 0.0009 inches was less than the 0.0036 inches required to fatigue the injector within the hot-fire test budget. This difference may be due to the structural damping or pressure loading diverging from assumptions. Therefore, further hot-fire tests were discontinued in favor of a conventional fatigue test of the injector, which is described in section 3.M of this report.

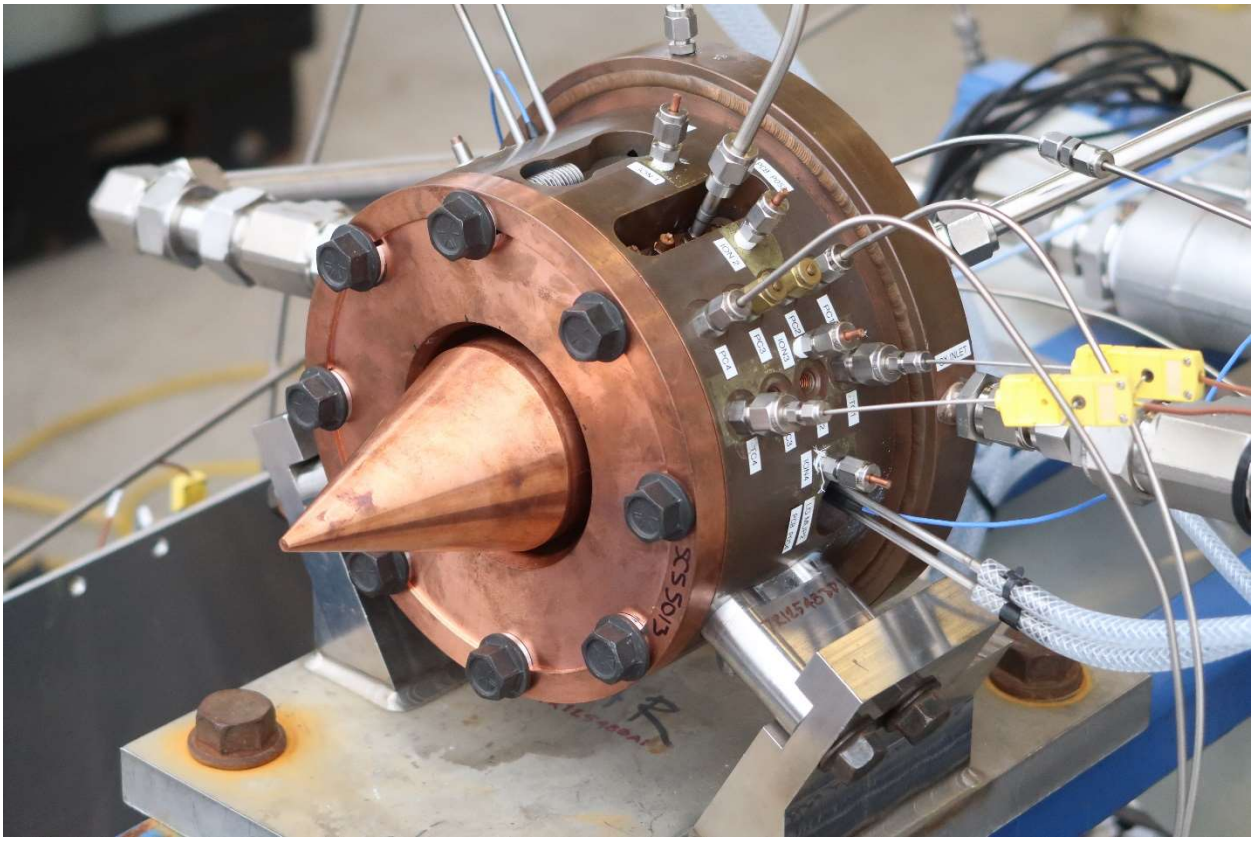

Figure 9. RDE Assembled for Hot-Fire Testing of Injector #2, View of the Exhaust Side

3. MATERIAL MODEL DEVELOPMENT

A. OVERVIEW

The Digital Twin (DT) concept was formulated by the systems engineering community with the basic premise that a complex physical system can be completely represented by a digital informational construct. This virtual digital system represents all aspects of the physical system itself, from the fabrication and assembly of the individual components, to the continuing exchange of data with the real system during the entire life cycle of the system, i.e., "cradle to grave," and all the elements needed for Product Lifecycle Management (PLM). Through modeling and simulation of the virtual digital system, operators can understand the behavior of the physical system and get insights on the future behaviors and maintenance needs.

The key element of a DT of a component is the material model to provide an assessment of the damage state in each zone of a component. A DTMM consists of several transfer functions that link the processing attributes to the structure features, and the structure features to properties or damage model. The DTMM is evaluated locally in every assessment zone of the component, often with emphasis near the hot spots where degradation is of upmost concern.

The DTMM describes the response of every material point based on the complete processing and in-service history and outputs relevant performance metrics for the operator to make decisions that can be used for fatigue assessment by linking process to structure and the structure to the HCF strength, as highlighted in yellow in Figure 10. It involves acquiring digital structure data and transforming this data to a form amendable for machine learning (ML) algorithms. In addition, if the loading within the zone being assessed in the component is known, a prediction of the cycles to failure or damage state can be determined.

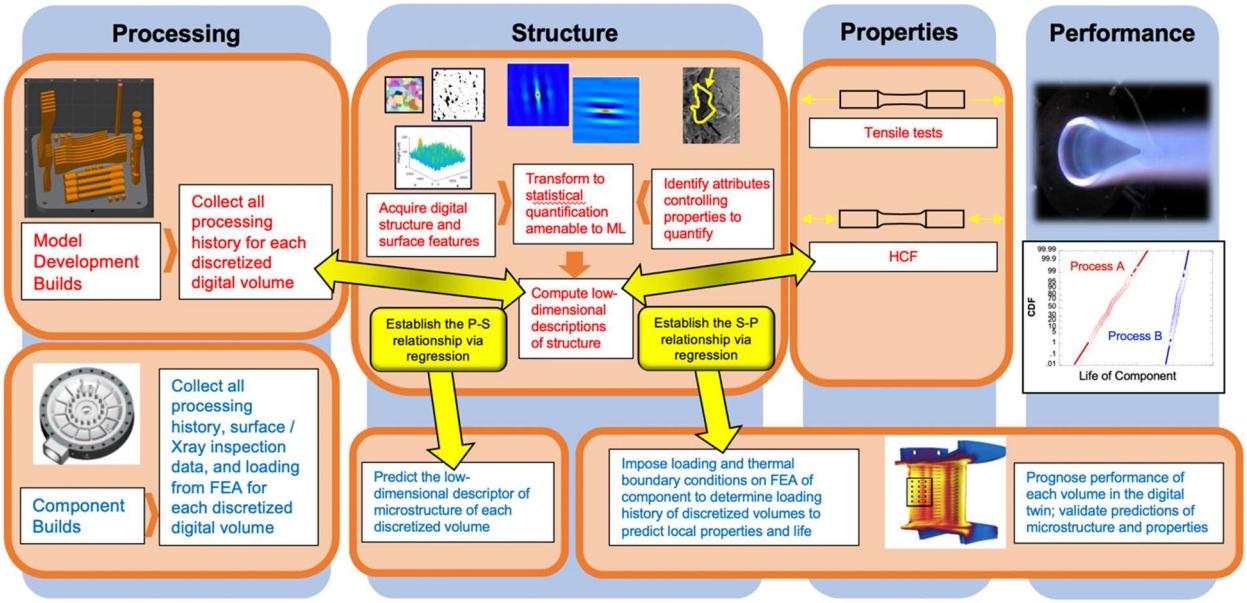

Figure 10. Holistic Application of a DT of a Component and Role of the DTMM

B. LITERATURE REVIEW OF ADDITIVELY MANUFACTURED INCONEL 625

The number of additive manufacturing process variables precluded an exhaustive experimental characterization of the possible build options. The literature was used to select a subset of parameters that should be varied in the coupon builds that inform the DTMM, and to select good values for those parameters that are to be held constant. Results from the literature review are summarized below.

B.1 MECHANICAL PROPERTIES

Inconel 625 is a nickel-based super-alloy often used in aerospace applications. It has a typical elemental composition (%) as follows.

Table 1. INCONEL alloy 625 Typical Composition (%)

Ni	Cr	Mo	Nb	Fe	C	Si	Al	Ti	Mn	S
61	21.5	9	3.6	2	0.05	0.20	0.20	0.20	0.20	0.001

One potentially important variant of Inconel 625 is the LCF variant alloy (as in low-cycle fatigue). This alloy limits carbon to 0.03% max, silicon to 0.15% max, and nitrogen to 0.02% max, and it has a different melting method and annealing practice. This variant of Inconel 625 has superior low-cycle fatigue strength.

The US Department of Defense (DoD) Military Handbook contains basic material property information for this alloy in wrought and cast forms. Inconel 625 is expected to have similar elastic properties for additively manufactured material and wrought material. In the open literature, Poulin et al. (2018) measure a $\pm 5\%$ variation of Young's modulus for AM Inconel 625 relative to the wrought value. They indicate that hot isostatic pressing (HIP'ing) increases Young's modulus and attribute this increase to lower porosity and the dissolution of carbide particles resulting in more Mo and Nb atoms in the matrix. Koutiri et al. (2018) measure a 13% reduction in Young's modulus for AM Inconel 625 vs. wrought material. Their process introduced porosity that may result in the lower value for Young's modulus. In both references, it is unclear if the authors followed the appropriate ASTM standard to measure Young's modulus, and the wrought value may provide an appropriate level of accuracy for engineering purposes. At room temperature for annealed material, the US DoD handbook sets a design value for Young's modulus of 206 GPa and a design value of Poisson's ratio of 0.28. For annealed material, the modulus decreases by approximately 50% as the temperature increases from room temperature to 900°C. The Special Metals data sheet for Inconel 625 also shows a reduction in modulus with temperature, but the decrease is only 29% at a temperature of 871°C. Poisson's ratio increases by approximately 20% as the temperature increases over the same range for both the DoD and Special Metals sources.

Debroy et al. (2018), list the modulus for Inconel 625 as well as Haynes 230, another nickel alloy, and show a strong dependence on build orientation, with the transverse (X-Y) orientation having a modulus that is on average 28% lower than the longitudinal orientation. However, these measurements for Inconel 625 employed a non-standard geometric specimen. Furthermore, these specimens were not heat-treated to remove residual stress from the specimens. Finally, the authors of the original study (Yadroitsev et al. 2007) highlight that the transverse samples featured numerous defects, and they attribute the reduced value of Young's modulus to these defects. HIP'ing specimens may mitigate the effect of defects on Young's modulus, and close the gap between the transverse and longitudinal build directions.

Table 2. Young's Modulus for Additively Manufactured Nickel Alloys, reproduced from Debroy et al. (2018)

Alloy	Process	Post-Processing	Orientation	Young's Modulus (GPa)
Inconel 625	SLM	AF	X-Y	141
Inconel 625	SLM	AF	Z	202
Haynes 230	SLM	AF	X-Y	152
Haynes 230	SLM	AF	Z	205
Nomenclature				
SLM	Selective Laser Melting	X-Y	Transverse Orientation	
AF	As Fabricated	Z	Build Orientation	

AM parts typically feature higher yield stress values than similar wrought/cast material. The US DoD Military handbook recommends a design yield strength of 414 MPa based on annealed material. This value may underestimate yield strength in the AM material, but it should lead to a conservative prediction for yielding.

Alexandre et al. (2004) show that fatigue lives for Inconel 718 (a sister alloy of Inconel 625) decrease with increased grain size. This trend is expected to hold for Inconel 625 as well. Material porosity is also expected to have a strong influence on AM material fatigue life. Grain size and porosity will be a function of AM processing history. Unfortunately, no fatigue data were found in the open literature that directly addresses the processing history of the material in this project. The next section will show information for as-built and annealed parts, but these parts lack the important HIP'ing step.

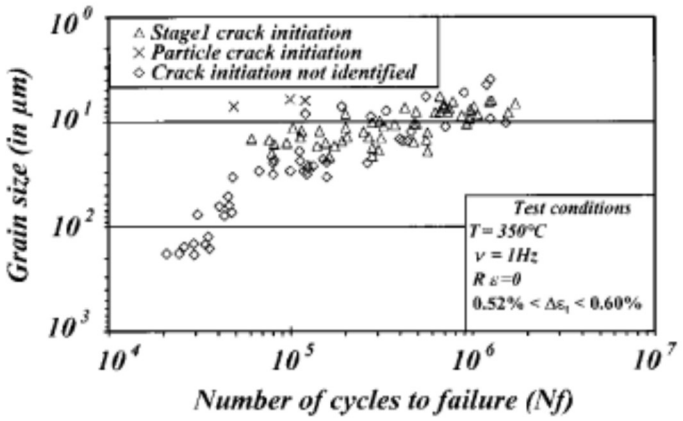

Figure 11. Fatigue Life decreases with increased Grain Size in Inconel 718, reproduced from Alexandre et al. (2004)

Anam (2018) summarizes mechanical property data from the literature for additively manufactured Inconel 625. Table 3 shows the effect of process, post-processing, and orientation on yield strength, ultimate tensile strength, and elongation. The nominal performance for the two machines used in this project, the Concept M2 and Renishaw 250, are also included (Renishaw results are for 30 and 60 micron powder layer thicknesses). Note that both of these machines use the selective laser melting (SLM) process. Most specimens have yield strength values at or above the DoD design value of 414 MPa. However, a few SLM specimens have yield strength values below the design value. The minimum yield stress is 360 MPa, and it includes an annealing step and HIP'ing. The strong dependence of mechanical properties on processing history is easily seen in the graphical presentation of some of the data from Table 3. Figure 12 shows the

large variability in ultimate tensile strength and elongation to failure for AM Inconel 625 samples. This clearly motivates the DTMM development so that material properties may be determined given a set of processing parameters.

Table 3. Summary of Mechanical Property Data for Additively Manufactured Inconel 625, reproduced from Anam (2018)

Author	Year	Process	Post Processing	Orientation	0.2% Yield Strength, MPa	Ultimate Tensile Strength, MPa	% Elongation
Xue	2007	LDED	AF	X-Y	477	744	48
Xue	2007	LDED	AF	Z	518	797	31
EOS	2010	SLM	AF	X-Y	725	990	35
EOS	2010	SLM	AF	Z	615	900	42
Betts	2011	SLM	AF	X-Y	384	898	60
Betts	2011	SLM	AF	Z	376	883	57
Yadroitsev	2009	SLM	AF	X-Y	720	1070	9
Yadroitsev	2009	SLM	AF	Z	800	1030	9
Optomec	2012	LDED	AF	X-Y	694	1052	33
Optomec	2012	LDED	AF	Z	490	829	43
Murr	2011	EBM	AF	X-Y	300	590	53
Murr	2011	EBM	AF	Z	410	750	44
Murr	2011	EBM	A+HIP	Z	330	770	69
Murr	2011	EBM	A+HIP	Z	230	610	70
Rombouts	2012	LDED	AF	X-Y	480	882	36
Rombouts	2012	LDED	AF	Z	656	1000	24
Amato	2012	SLM	A+HIP	X-Y	380	900	58
Amato	2012	SLM	A+HIP	Z	360	880	58
EOS	2011	SLM	SR	X-Y	720	1040	35
EOS	2011	SLM	SR	Z	650	930	44
Concept M2	2017	SLM	?	X-Y	713	1061	41
Concept M2	2017	SLM	?	Z	661	932	31
Renishaw (30)	2017	SLM	AF	X-Y	767	1055	34
Renishaw (30)	2017	SLM	A	X-Y	633	1020	39
Renishaw (30)	2017	SLM	AF	Z	676	964	42
Renishaw (30)	2017	SLM	A	Z	598	955	43
Renishaw (60)	2017	SLM	AF	X-Y	667	922	18
Renishaw (60)	2017	SLM	A	X-Y	600	1005	31

Author	Year	Process	Post Processing	Orientation	0.2% Yield Strength, MPa	Ultimate Tensile Strength, MPa	% Elongation
Renishaw (60)	2017	SLM	AF	Z	536	770	11
Renishaw (60)	2017	SLM	A	Z	583	985	32
Dutta	2011	LDED	-	Z	598	795	14
MMPDS		AMS	A	Z	414	827	30

Nomenclature			
LDED	Laser Direct Energy Deposition	HIP	Hot-Isostatic Press
SLM	Selective Laser Melting	SR	Stress Relief
EBM	Electron Beam Welding	A	Anneal
AMS	Aerospace Material Specification	X-Y	Transverse Orientation
AF	As Fabricated	Z	Build Orientation

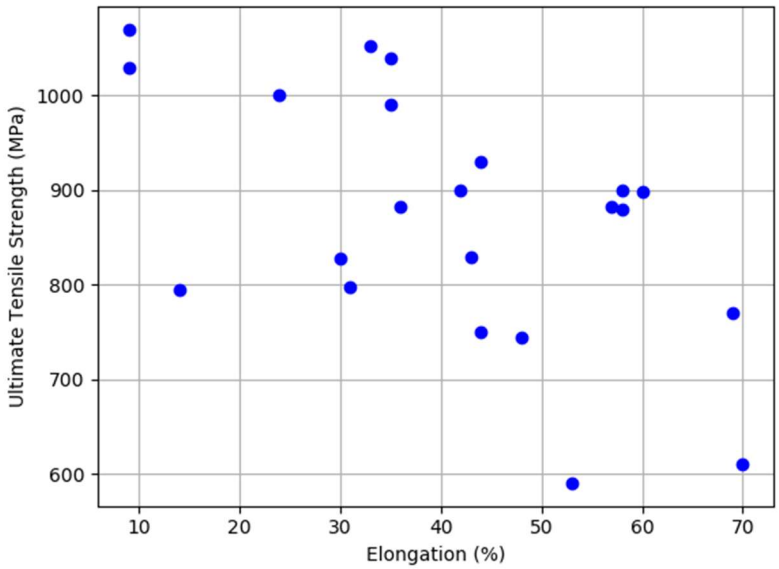

Figure 12. The Large Variation in Strength and Ductility of Additively Manufactured Inconel 625

The literature review results were used to assume the room temperature properties that were used in the preliminary injector design. These assumptions are stated in Table 4. Portions of the injector will not operate at room temperature conditions. Mechanical properties were adjusted for temperature based on the trends presented in the Special Metals material data sheet.

Table 4. Room Temperature Mechanical Properties to Assumed in the Preliminary Injector Design

Property	Value	Source
Yield strength	414 MPa	US DoD Military Handbook design value for wrought/cast products (AM material usually exceeds this)
Elastic modulus, longitudinal build orientation	206 GPa	US DoD Military Handbook design value for wrought / cast products that was found to be similar to data for the longitudinal build direction
Elastic modulus, transverse build orientation	185 GPa	90% of the longitudinal value based on the expectation that HIP'ing will remove some of the transverse orientation defects
Poisson's ratio	0.28	US DoD Military Handbook design value
Fatigue strength	Design curves from the US DoD Military Handbook and Special Metals data sheets	

B.2 PROCESS PARAMETERS

Several parameters control the additive manufacturing process. The definition of each parameter considered in this review is given in Table 5. The objective of the literature review is to determine the combination of parameters that results in the highest fatigue strength. Two observable indicators of higher fatigue strength are small grain size (see Figure 11) and low porosity, and these are used as the primary material quality metrics.

Table 5. Definition of Additive Manufacturing Process Parameters

Parameter	Definition
Laser power	Strength of the laser that is used to melt the powder material
Laser speed	How fast the laser moves across the powder bed surface
Hatch spacing	The distance between parallel rows of laser passes
Scan strategy	The path the laser takes to fully cover the cross-sectional area of a layer, and the difference in this path from one layer to the next
Laser spot size	Diameter of the laser beam when it is incident on the powder bed surface
Layer thickness	Depth of powder that is melted during a pass of the laser
Energy density	Applied laser energy per unit volume of powder. This is a dependent quantity that is a result of the other laser parameters.
Substrate preheating	Temperature of the powder bed prior to laser application

Montgomery (2015) provides process maps for Inconel 625. These maps likely employ a powder thickness of 60 microns, though it is not explicitly stated in the paper. The authors state that the powder thickness has a limited impact on the results in the thickness range that they examined. This statement relies on experimental measurements and numerical simulations of the powder. Overall, the melt pool is maximized

and keyholing is prevented using the following combinations of source power (W) and velocity (mm/s): (70,200); (110,400); (145,600); and (185,800) (the red line of Figure 13). In this context, keyholing indicates a high-energy mechanism that forms deep but slender melt pools. These melt pools encourage the development of porous regions with a spherical base and a long slender extension in the build direction. Pores produced by keyholing are especially susceptible to fatigue initiation and are difficult to correct through HIP'ing. Similar process parameter combinations will also prevent keyholing, but they result in smaller melt pools that would prolong the build time. The red line indicates the largest melt pools that do not produce keyholing.

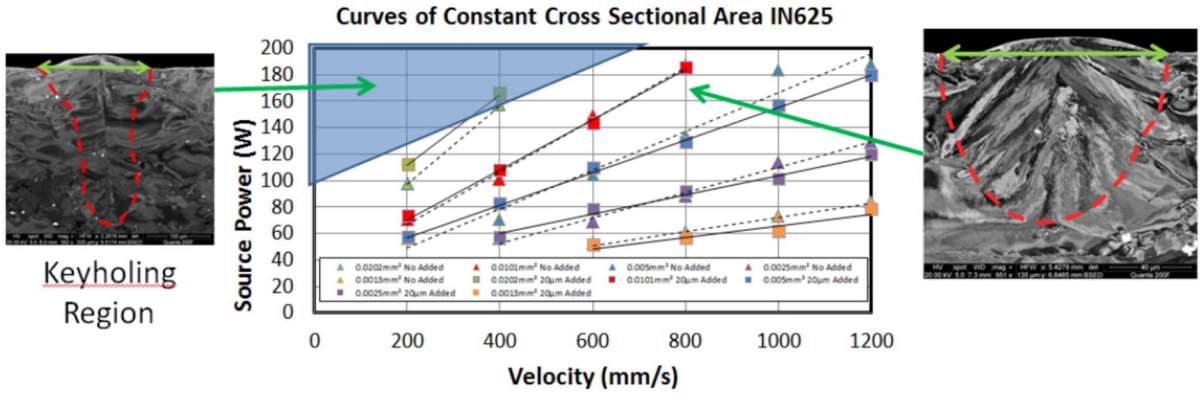

Figure 13. Experimental Curves of Constant Cross-Sectional Area for IN625 and an Annotation for the Keyholing Region. Colors represent a Constant Cross-Sectional Area of the melt pool, reproduced from Montgomery (2015)

Arisoy et al. (2016) investigated the influence of scan strategy and process parameters on additively manufactured Inconel 625. They varied the stripe scan pattern (rotations of 90° per consecutively built layers vs 67° per consecutively built layers); laser power (169W, 182W, and 195W); scan velocity (725 mm/s, 800 mm/s, and 875 mm/s); and hatch distance (0.09 mm, 0.1 mm, and 0.11 mm). They measured average grain size, grain size deviation, and grain growth direction (to measure anisotropy). The 67-degree scan pattern rotation is of interest since this approach tended to promote smaller grain sizes. Table 6 below shows the measurements of average grain size and grain size deviation. For reference, the average grain size of annealed Inconel 625 is on the order of 50-230 microns depending on the annealing heat treatment. As-drawn Inconel has an average grain size of approximately 80 microns. Key processing parameter sets that result in minimum grain sizes have been highlighted.

Table 6. Grain Diameters for different Process Parameters, reproduced from Arisoy et al. (2016)

Coupon #	Rotation strategy SSR (°)	Laser power P (W)	Scan velocity v_s (mm/s)	Hatch distance h (mm)	Energy density E (J/mm^3)	Average grain diameter D_{avg} (μm)	SD of grain diameters SD_{avg} (μm)
2	67	169	725	0.1	116.6	0.52	0.12
3	67	195	725	0.1	134.5	0.52	0.11
5	67	169	800	0.09	117.4	0.57	0.09
7	67	182	800	0.1	113.8	0.60	0.08
10	67	182	725	0.11	114.1	0.73	0.13
11	67	169	875	0.1	96.6	0.50	0.09
13	67	195	800	0.09	135.4	0.62	0.09
19	67	195	875	0.1	111.4	0.48	0.21
22	67	182	800	0.1	113.8	0.39	0.13
24	67	182	800	0.1	113.8	0.55	0.15
25	67	195	800	0.11	110.8	0.50	0.09
26	67	182	875	0.09	115.6	0.51	0.07
27	67	182	725	0.09	139.5	0.44	0.15
28	67	182	875	0.11	94.6	0.39	0.06
30	67	169	800	0.11	96.0	0.61	0.14
31	67	195	800	0.1	121.9	0.76	0.14

Arisoy et al. (2016) also provide information on grain growth orientations as shown in the following figure. This table shows grain growth direction measured in the XZ plane. Since the grains grow semi-randomly, some of them grow along a positive angle (relative to the Z or build axis) and some grow along a negative angle. The authors break these angles up. They then bin the positive and negative angles into 10-degree bins. The column marked $\theta +$ and $\theta -$ indicate the bin where most of the angles are located. For example, coupon 13 has most of its grains oriented in +10-degree bin and -10-degree bin. There are still grains oriented in other directions, but most grains are oriented in the 10-degree bin. The columns marked mean and standard deviations refer to values within the bin itself and do not include orientations outside of the bin. Aligning the growth direction angles with the build direction (making them close to zero) may strengthen parts in the build (Z) direction. Since the YS and UTS tend to be low in the Z-direction, this may be an appropriate design target to reduce anisotropy. Specimens with minimum grain growth orientations have been highlighted below.

Table 7. Grain Direction for different Process Parameters, reproduced from Arisoy et al. (2016)

Coupon #	Laser power P (W)	Scan velocity v_s (mm/s)	Hatch distance h (mm)	Energy density E (J/mm^3)	θ+ (°)	Mean of θ+ (°)	SD of θ+ (°)	θ− (°)	Mean of θ− (°)	SD of θ− (°)
2	169	725	0.1	116.6	10	9.6	2.9	0	−0.6	2.7
3	195	725	0.1	134.5	10	10.2	2.6	0	2.6	2.0
5	169	800	0.09	117.4	10	11.7	2.3	−10	−9.2	2.9
7	182	800	0.1	113.8	20	19.0	2.8	−10	−9.9	2.7
10	182	725	0.11	114.1	20	19.6	3.0	−20	−20.1	2.8
11	169	875	0.1	96.6	20	19.9	2.3	−20	−19.5	2.4
13	195	800	0.09	135.4	10	10.1	2.7	−10	−10.4	2.4
19	195	875	0.1	111.4	0	−3.6	1.4	−10	−12.1	2.2
22	182	800	0.1	113.8	10	12.3	2.0	0	4.4	0.5
24	182	800	0.1	113.8	20	19.3	3.0	10	12.1	2.0
25	195	800	0.11	110.8	30	28.5	1.7	−10	−11.5	2.4
26	182	875	0.09	115.6	30	27.9	1.7	−10	−11.4	2.7
27	182	725	0.09	139.5	30	28.0	1.8	−20	−20.7	2.9
28	182	875	0.11	94.6	10	10.5	2.8	−20	−19.5	2.7
30	169	800	0.11	96.0	30	28.2	1.6	−20	−19.9	3.5
31	195	800	0.1	121.9	0	−2.7	2.0	−30	−27.8	1.5

These experimental results lead to the development of a multi-objective optimization. For a 67° scan pattern, they predicted that the minimum grain size could be achieved using a power of 195W, a scan velocity of 865.9 mm/s, and a hatch spacing of 0.11 mm. Furthermore, the resulting response surface predicts minimum grain growth direction angles for a power of 195W, a scan velocity of 835.6 mm/, and a hatch spacing of 0.1 mm. They summarize their findings as follows:

- Increasing energy density tends to result in larger grain sizes based on a statistical analysis by the authors. This relationship is not perfect. The average grain size tends to increase with higher power and tends to decrease with higher scan velocities. The average grain size tends to increase with the hatch distance for a 67-degree rotation and tends to decrease with a 90-degree rotation.
- Finer grain sizes can be obtained when process parameters are optimized using a scan strategy rotation of 67°.
- Growth directions are less influenced by laser power and scan velocity when a scan strategy rotation of 67°is used.
- A combination of medium-high scan velocity and medium hatch distance is seen as ideal for growth aligning in the build direction and resulting in an isotropic build. For a 67-degree rotation, the optimum parameters are P=195 W; v=835.6 mm/s; and h=0.0996 mm. For a 90-degree rotation, the optimum parameters are 169W; v=786 mm/s; and h=0.09 mm. These results are based on an optimized response surface.

In a later paper by the same group, Criales et al. (2017) investigated the effect of process parameters on melt pool shape and size. During this work, the authors measured density relative to a fully dense part. Denser measurements suggest less porosity and higher fatigue lives due to fewer internal voids to drive fatigue crack initiation. Their results are shown in Table 8 with the highest density result highlighted.

Table 8. Material Density for different Process Parameters, reproduced from Criales et al. (2017)

Laser Power, P [W]	Scan Velocity, v_s [mm/s]	Hatch Distance, h [mm]	Energy Density, E [J/mm^3]	Relative Density (SSR=67°), ρ_{rel} [%]	Relative Density (SSR=90°), ρ_{rel} [%]
169	875	0.10	96.57	95.23	96.00
195	875	0.10	111.43	98.30	98.70
182	875	0.09	115.56	97.03	97.40
182	725	0.11	114.11	95.97	96.17
195	800	0.11	110.80	98.47	98.52
182	725	0.09	139.46	97.14	97.29
182	800	0.10	113.75	98.10	98.21
182	800	0.10	113.75	98.05	98.19
195	725	0.10	134.48	97.50	97.74
182	800	0.10	113.75	98.13	98.30
182	875	0.11	94.55	96.50	96.75
169	725	0.10	116.55	96.38	96.52
169	800	0.09	117.36	97.50	97.91
169	800	0.11	96.02	96.60	96.78
195	800	0.09	135.42	99.01	99.23
195	800	0.10	121.88	98.64	98.86
195	800	0.10	121.88	98.53	98.75
195	800	0.10	121.88	98.69	98.81

In general, the scan-stripe rotation of 90° leads to slightly more dense material than the 67° rotation strategy. Parts with density in excess of 99% may be achieved with a power of 195W, a scan velocity of 800 mm/s, and a hatch distance of 0.09 mm. The authors of this report did not provide a similar response surface optimize processing parameters. These scan parameters would lead to larger grains and non-optimal anisotropic grain growth based on the earlier work.

Marchese et al. (2016) investigated the effect of processing parameters on Inconel 625. For selective laser melting, they fixed the scan rotation at 67° and varied power, velocity, and hatch distance. Their design of experiment is summarized in Table 9.

Table 9. Parameters used in the Marchese et al. (2016) Design of Experiment

Parameter	Values
Laser power [W]	175, 185, 195
Laser speed [mm/s]	600, 900, 1200
Hatch spacing [mm]	0.07, 0.09, 0.11
Layer thickness [μm]	20
Substrate temperature [°C]	80°C
Laser spot size [mm]	0.10

Supplemental information shows porosity and hardness from these parameter settings. Most porosity values are less than 1%. Sample S7 showed the lowest porosity, and it was built using a scan speed of 900 mm/s, a laser power of 185 W, and a hatching distance of 0.07 mm. However, similar porosity levels develop using the parameter set from S5, S12, S21, and S25.

Table 10. Residual Porosity for different Process Parameters, reproduced from Marchese et al. (2016)

Sample	P [W]	v [mm s^{-1}]	h_d [mm]	E_D [J mm^{-2}]	Residual porosity [%]	Brinell hardness [HBW]
S1	185	1200	0.07	2.20	0.050 ± 0.014	287 ± 3
S2	185	600	0.11	2.80	0.069 ± 0.024	282 ± 3
S3	175	900	0.11	1.77	0.063 ± 0.011	290 ± 4
S4	185	600	0.09	3.43	0.046 ± 0.008	287 ± 3
S5	185	900	0.09	2.28	0.039 ± 0.007	289 ± 4
S6	185	1200	0.11	1.40	0.084 ± 0.021	275 ± 2
S7	185	900	0.07	2.94	0.036 ± 0.009	288 ± 4
S8	175	1200	0.11	1.33	0.122 ± 0.038	273 ± 2
S9	195	600	0.11	2.95	0.058 ± 0.009	283 ± 2
S10	175	600	0.07	4.17	0.048 ± 0.011	284 ± 4
S11	175	1200	0.09	1.62	0.084 ± 0.018	279 ± 2
S12	175	1200	0.07	2.08	0.045 ± 0.013	289 ± 3
S13	185	1200	0.09	1.71	0.062 ± 0.008	283 ± 3
S14	175	900	0.09	2.16	0.053 ± 0.011	283 ± 4
S15	185	600	0.07	4.40	0.061 ± 0.025	284 ± 4
S16	195	1200	0.11	1.48	0.199 ± 0.025	266 ± 4
S17	195	900	0.11	1.97	0.089 ± 0.016	276 ± 4
S18	195	600	0.09	3.61	0.057 ± 0.015	281 ± 6
S19	195	900	0.07	3.10	0.048 ± 0.012	286 ± 5
S20	185	900	0.11	1.87	0.059 ± 0.017	284 ± 6
S21	195	900	0.09	2.41	0.045 ± 0.013	290 ± 2
S22	175	600	0.11	2.65	0.111 ± 0.023	279 ± 2
S23	195	1200	0.07	2.32	0.046 ± 0.012	292 ± 5
S24	175	600	0.09	3.24	0.070 ± 0.025	275 ± 3
S25	175	900	0.07	2.78	0.039 ± 0.015	293 ± 4
S26	195	600	0.07	4.64	0.064 ± 0.020	286 ± 4
S27	195	1200	0.09	1.81	0.064 ± 0.014	285 ± 3

Anam (2018) investigated the influence of laser power and scan speed on the melt pool depth to width ratios. He states that a ratio of 0.5 ± 0.1 is optimal to produce parts with a minimum number of defects. This study provides a map showing the combinations of laser power and laser speed and the resulting melt pool depth to width ratios.

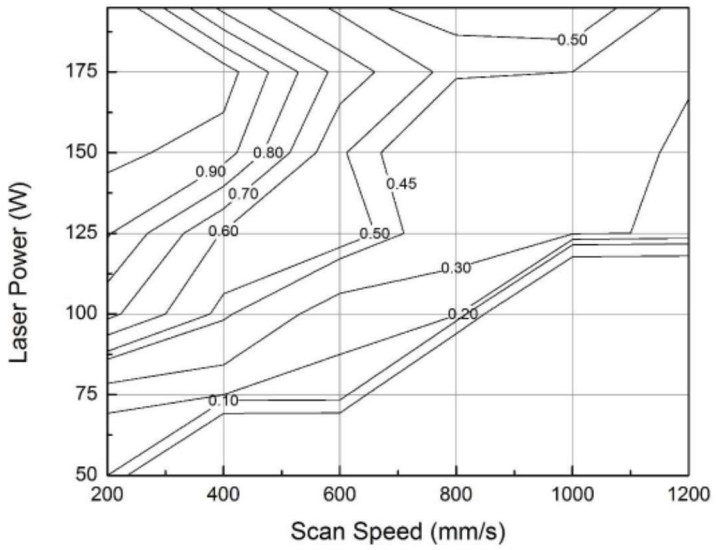

Figure 14. Melt Pool Depth to Width Ratios for Combinations of Laser Power and Laser Speed, reproduced from Anam (2018).

Anam also provides micrographs of polished cross-sections showing porosity of cubes produced using various scan parameters. The micrographs are shown in Figure 15 and the corresponding quantitative measurements are given in Figure 16. Low porosity is obtained with higher laser power. For a given power, porosity at first decreases with increasing scan speed, reaches a minimum and then begins to increase. The maximum scan speed tested, 1200 mm/s, is not fast enough to show the range of increasing porosity for the highest laser power.

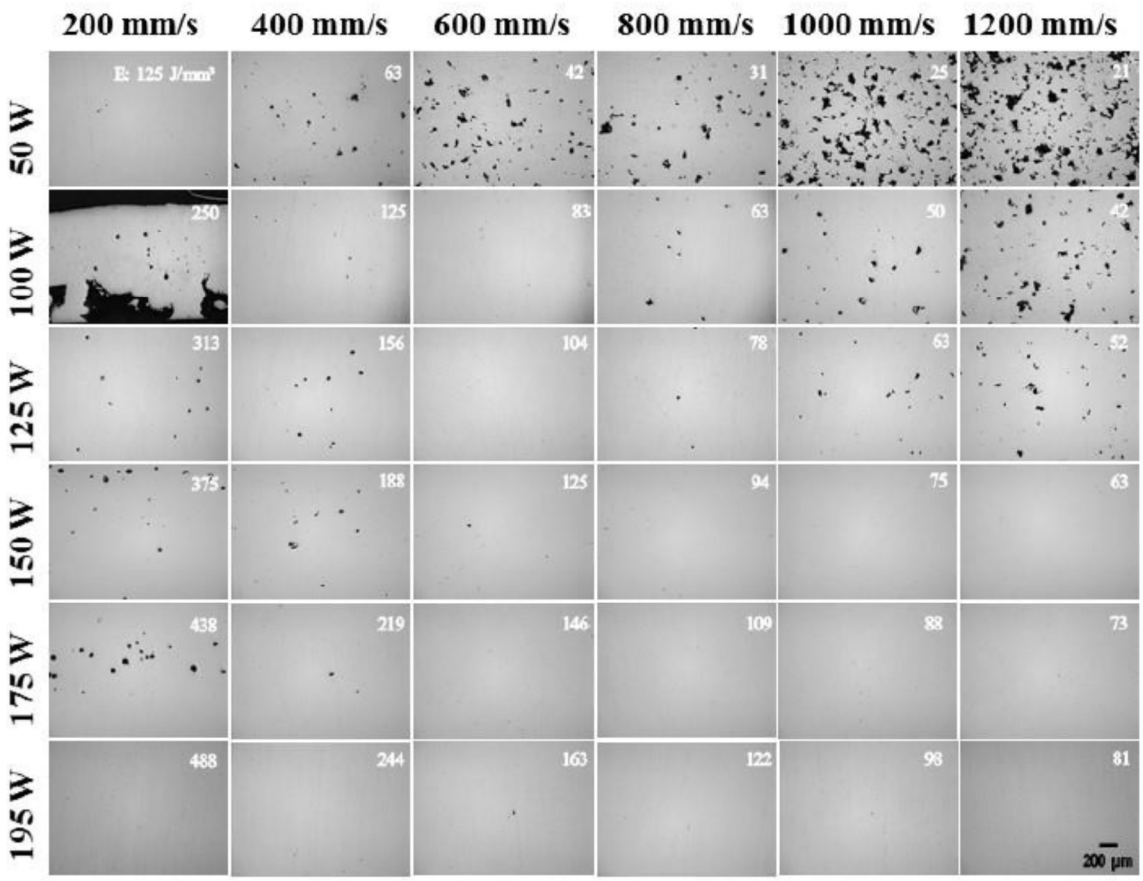

Figure 15. Micrographs of Additively Manufactured Inconel 625 show Porosity for Combinations of Laser Power and Speed, reproduced from Anam (2018).

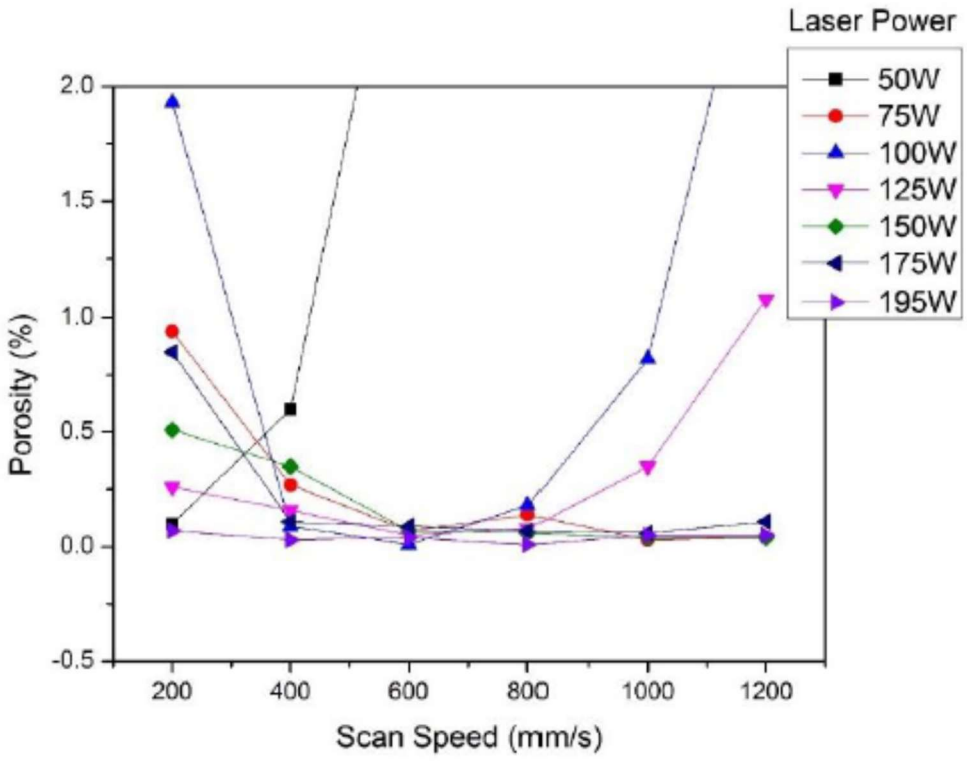

Figure 16. Quantitative Measurements of Porosity as a Function of Laser Power and Speed that Correspond to the Micrographs of Figure 15, reproduced from Anam (2018).

Additional studies by Anam investigate the effect of build orientation and scan strategy rotation on the tensile mechanical properties for a laser power of 195W, scan speed of 800 mm/s, layer thickness of 20 microns, and hatch spacing of 0.1 mm. In general, Inconel 625 shows some anisotropy with these build parameters that cannot be reduced by heat treatment. However, heat treatment is recommended to increase elongation.

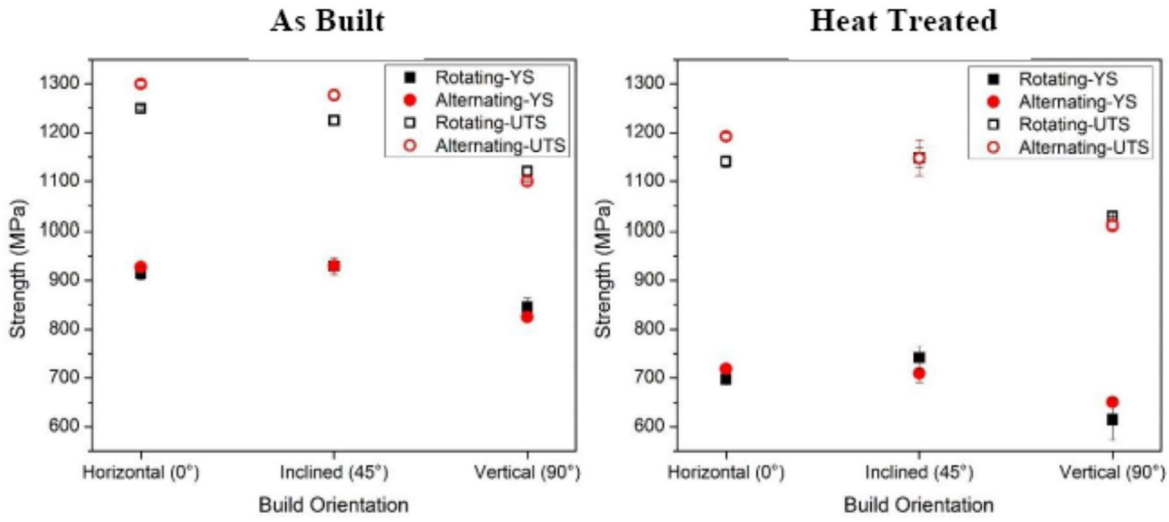

Figure 17. The Effect of Build Orientation and Heat Treatment on the Tensile Strength Properties of Additively Manufactured Inconel 625, reproduced from Anam (2018)

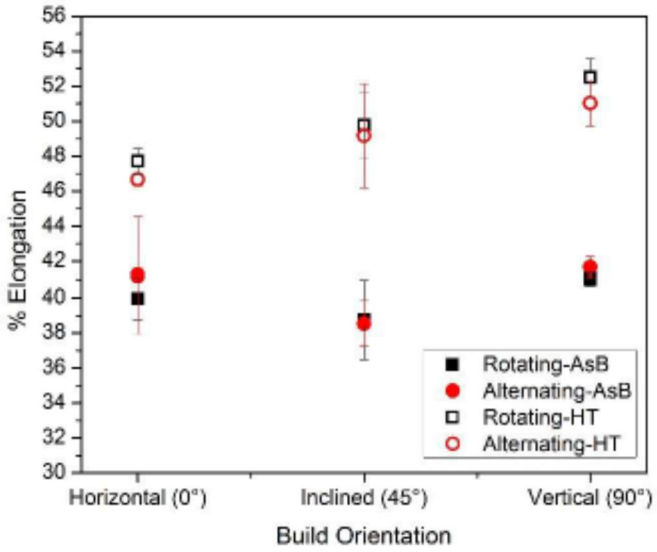

Figure 18. The Effect of Build Orientation and Heat Treatment on the Elongation to Failure of Tensile Specimens of Additively Manufactured Inconel 625, reproduced from Anam (2018)

Anam also investigated cyclic fatigue life for Inconel 625. They varied the build orientation and heat treatment. It is assumed that the heat treatment is an annealing heat treatment, not HIP'ing. However, Anam is not clear on this point. In any case, the heat treatment had limited impact on the fatigue life. The build direction was more important to fatigue lives. Building along the Z-axis (in the axial direction of tensile specimens) lead to lower fatigue lives than building normal to the Z-axis. Anam attributed this to defects in the material normal to the build direction. That is, the AM process introduces preferentially aligned pores into the material.

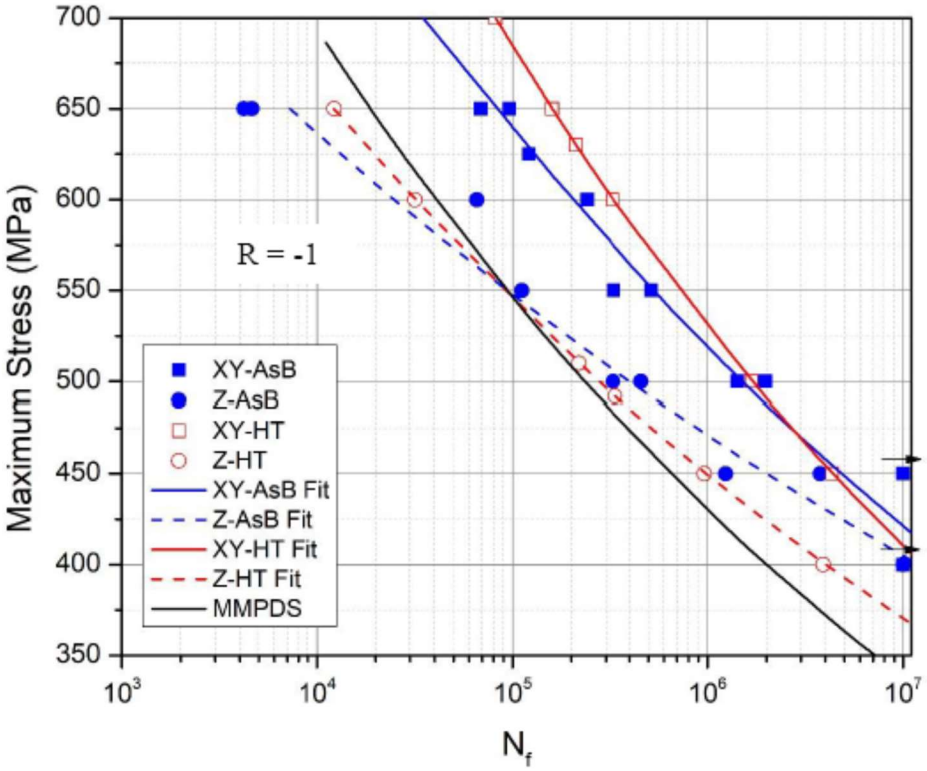

Figure 19. Fatigue Strength vs. Cycles to Failure for Additively Manufactured Inconel 625 Tensile Specimens Built in the Z and X-Y Orientations and with and without Heat Treatment, reproduced from Anam (2018)

Koutiri et al. (2018) investigated surface finish, porosity rate, and fatigue behavior of as-built Inconel 625 parts. They investigated contour parameters that control melting on the part surface and hatching parameters that control melting on the part interior. Table 11 shows the surface roughness results, where the general trend is that it was minimized as power increased (i.e., increased volume energy density).

Table 12 shows the observations for porosity. Generally speaking, they are consistent with earlier measurements that show limited porosity for energy densities in the range of 45-90 J/mm^3 for the lower power settings (P<200W), though there is one outlier (specimen 25). Higher power and velocity settings than are supported by the Concept M2 and Renishaw machines at Aerojet Rocketdyne and SwRI may produce low porosity builds.

As shown in Figure 20, polishing the specimen removes surface initiation sites and forces initiation to develop at interior anomalies. These interior anomalies may be minimized by HIP'ing the specimen. However, polishing was not an option for the injector component built in this project based on the geometry of the design.

Table 11. Surface Roughness of As-Built Components for different Process Parameters, reproduced from Koutiri et al. (2018)

Number of specimen		θ (°)	Contour parameters			VED (contour))	Hatching parameters			Roughness*
			P (W)	V (m/s)	D (μm)	J/mm^3	P (W)	V (m/s)	D (μm)	Sa (μm)
Tests for Surface roughness	1	10	100	0.5	70	52	175	0.6	70	**11**/14
	2	10	140	0.5	70	72.8	175	0.6	70	**7.5**/11.8
	3	10	180	0.5	70	93.6	175	0.6	70	**5.9**/6.2
	4	35	100	0.5	70	52	175	0.6	70	**11**/16.5
	5	35	140	0.5	70	72.8	175	0.6	70	**7.5**/20.5
	6	35	180	0.5	70	93.6	175	0.6	70	**10.6**/23
	7	0	400	1	70	104	400	1	70	**10.5**
	8	0	400	1.4	70	74.3	400	1.4	70	**12.3**
	9	0	400	1.8	70	57.8	400	1.8	70	**12.4**
	10	0	400	2	70	52	400	2	70	**9.5**
	11	0	400	1	160	19.9	400	1	160	**21**
	12	0	400	1.4	160	14.2	400	1.4	160	**18.9**
	13	0	400	1.8	160	11.1	400	1.8	160	**17.1**
	14	0	400	2	160	10	400	2	160	**15.2**
	15	0	400	1	240	8.8	400	1	240	**21**
	16	0	400	1.4	240	6.3	400	1.4	240	**20.3**

(* **bold** = **upper surface**, normal = lower surface).

Table 12. Porosity of As-Built Components for different Process Parameters, reproduced from Koutiri et al. (2018).

Set of SLM Parameters and porosity ratios.

	Test	θ (°)	Contour parameters			Hatching parameters			VED (hatching)	Porosity
			P (W)	V (m/s)	D (μm)	P (W)	V (m/s)	D (μm)	J/mm^3	(%)
Tests for porosity	7	0	400	1	70	400	1	70	104	0,51 ± 0.05
	8	0	400	1.4	70	400	1.4	70	74.3	1,17 ± 0.4
	9	0	400	1.8	70	400	1.8	70	57.8	1,85 ± 0.34
	10	0	400	2	70	400	2	70	52	2,43 ± 0.9
	11	0	400	1	160	400	1	160	19.9	0,36 ± 0.09
	12	0	400	1.4	160	400	1.4	160	14.2	0,91 ± 0.12
	13	0	400	1.8	160	400	1.8	160	11.1	2,96 ± 0.8
	14	0	400	2	160	400	2	160	10	2,7 ± 0.4
	15	0	400	1	240	400	1	240	8.8	1,16 ± 0.09
	16	0	400	1.4	240	400	1.4	240	6.3	1,30 ± 0.6
	17	0	400	1.8	240	400	1.8	240	5,1	5,06 ± 0.2
	18	0	400	2	240	400	2	240	4,6	7,20 ± 0.3
	19	0	180	0,5	70	175	0,6	70	79,3	1,44 ± 0,4
	20	0	140	0,5	70	175	0,6	70	79,3	0,7 ± 0,16
	21	0	140	0,5	70	175	0,7	70	68	1,29 ± 0,22
	22	10	140	0.5	70	150	0.6	70	68	0.2 ± 0.08
	23	10	140	0.5	70	200	0.6	70	90,7	0.37 ± 0.18
	24	10	140	0.5	70	175	0.7	70	68	2.1 ± 0.51
	25	10	140	0.5	70	175	0.8	70	59,5	6.32 ± 1.26
	26	35	140	0.5	70	150	0.6	140	17	0.36 ± 0.04
	27	35	140	0.5	70	200	0.6	140	22,6	0.12 ± 0.02
	28	35	140	0.5	70	175	0.7	140	17	0.66 ± 0.06
	29	35	140	0.5	70	175	0.8	140	14,8	1.61 ± 0.30

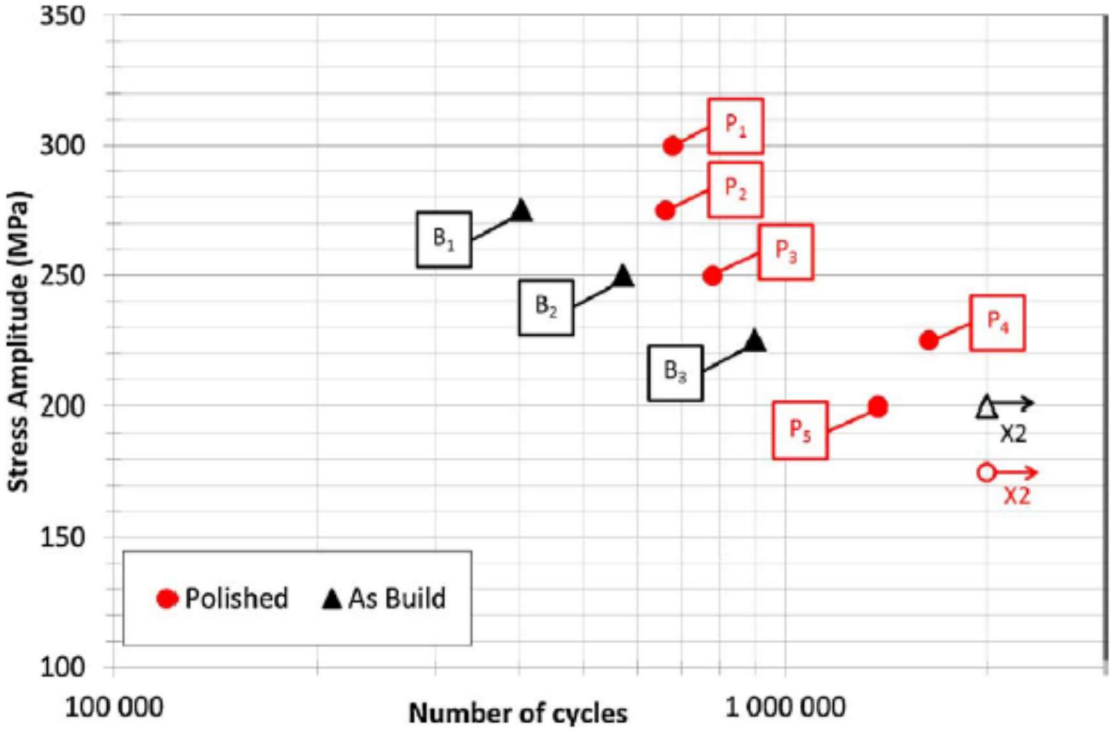

Figure 20. Fatigue Strength is increased by Polishing the Component Surface, reproduced from Koutiri (2018)

Grabill et al. (2018) summarize the effect of heat treatment on various nickel-based alloys. For Inconel 625, HIP'ing has a modest impact on yield strength. The annealing heat treatment has a more pronounced effect on yield strength and elongation.

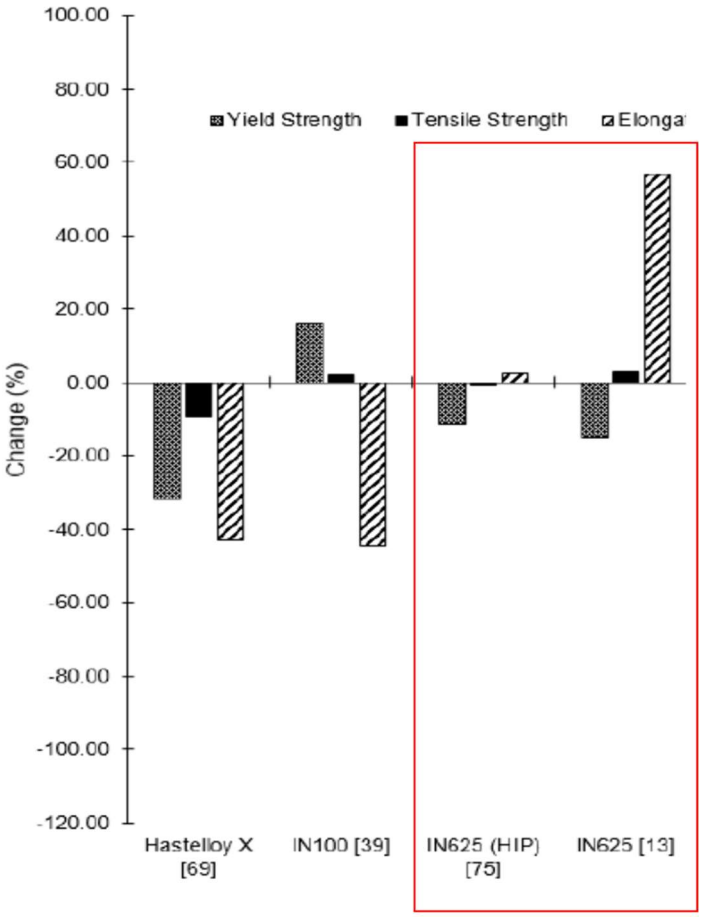

Figure 21. The Effect of Heat Treatment on Additively Manufactured Inconel 625 Tensile Properties, reproduced from Grabill et al. (2018)

Lass et al. (2017) of NIST indicate the formation of a delta-phase in Inconel 625 using the standard industry stress-relief anneal of 1 hour at 1143 K. This phase adversely impacts fracture toughness, ductility, and other mechanical properties. They suggest an alternate stress relief of 4 hours at 1073 K to mitigate delta-phase formation.

Zhang et al. (2018) also noticed the formation of delta-phase in Inconel 625 during the standard anneal cycle. Figure 22 below shows SEM micrographs after 0.5 hours, 1 hour, 4 hours, and 8 hours of heat treatment. White lines indicate the delta phase. They attribute the rapid formation of the delta-phase to elemental segregation during additive manufacturing. They suggest a homogenization heat treatment to remove the delta phase.

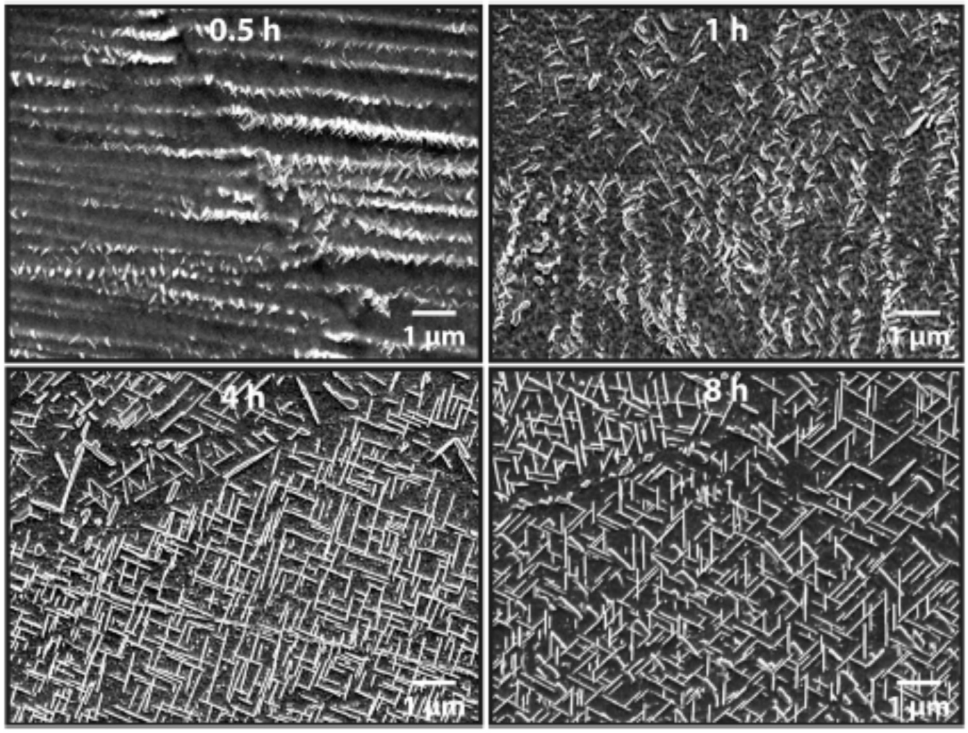

Figure 22. The Formation of Undesirable Delta-Phase in Additively Manufactured Inconel 625 after various Exposures to Industry Standard Annealing Conditions, reproduced from Zhang (2018)

B.3 FINDINGS

Based on the preceding information from the literature, the following range of processing parameters are recommended for the design of experiment used to generate data for the DTMM:

- Laser power between 175 W and 200 W, preferably near 200 W
- Laser speed between 800 mm/s and 900 mm/s, preferably near 900 mm/s
- Hatch spacing between 70 µm and 100 µm
- Scan strategy rotation of 67° was originally selected because it is expected to produce smaller grain sizes, which would correlate with improved fatigue performance. However, the Concept Laser M2 machine at Aerojet Rocketdyne only supports 90° rotation.
- Alternating laser paths
- Layer thickness of 40 microns
- Laser spot size between 70 microns and 100 microns
- Preheating the substrate to 80°C

These processing parameters are intended to produce a nearly fully dense part in the as-built configuration with an isotropic material response. The trade-off is that these parameters will promote larger grain sizes. Larger grain sizes often are associated with reduced yield strength and lower fatigue lives from persistent slip band formation. However, the grain size expected from these processing parameters should still be less than the as-drawn grain size of wrought Inconel. Furthermore, the major concern with an additively manufactured component for fatigue applications is fatigue initiation from pre-existing voids. Denser material will have fewer voids, and those voids should be more spherical if keyholing and lack-of-fusion defects are prevented.

It is also recommended to perform additional heat-treatment post build. These heat-treatments should include HIP'ing to further reduce voids in the part and/or annealing. It may be useful to heat treat the part at anneal cycle recommended by Lass et al. at NIST to mitigate delta-phase formation.

C. DATABASE DEVELOPMENT

Since data on the process-structure-HCF property of Inconel 625 available in the literature was not sufficient to establish the model, an extensive experimental program was undertaken to generate this data. Flat dog-bone HCF specimens were fabricated using a laser powder bed fusion (L-PBF) process with post-processing, including stress-relief and hot isostatic pressing (HIP). Several builds were fabricated, each containing multiple additively manufactured HCF specimens and microstructure samples, shown in Figure 23. Two sizes of specimens and two orientations (Z-direction, XY-direction) were fabricated. In addition, two HCF specimens of each type were further processed with a surface finishing step involving grinding and polishing the surfaces within the gage section to quantify the influence of surface finish on fatigue strength.

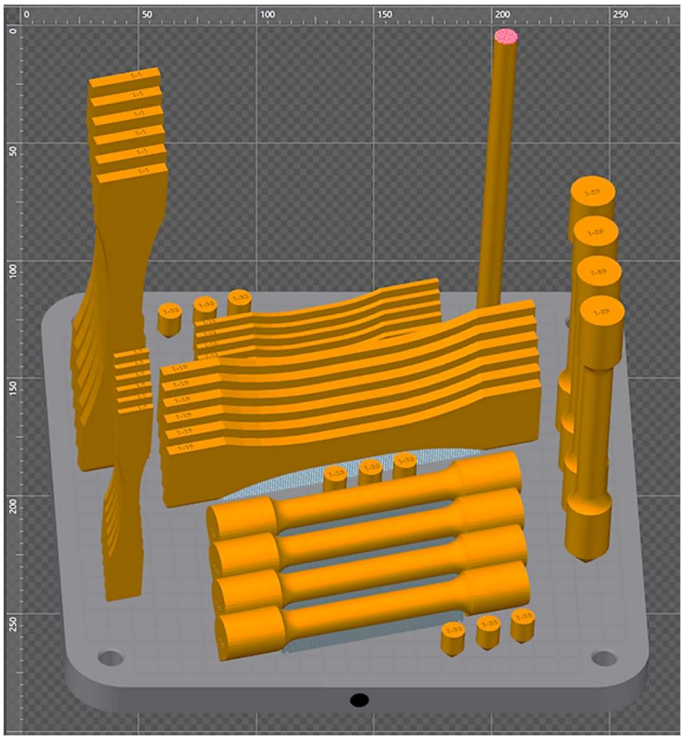

Figure 23. Specimen Configuration on the Build Plate Setup, Including "Dog-Bone" HCF Samples at Two Scales and Small Cylindrical Microstructure Samples

The number of builds was constrained by the project budget. To make the most of the available builds, a design of experiment approach was used with a 2^{4-1} factorial design. The design variables were laser velocity, hatch spacing, machine, and heat treatment. The design confounded the machine with the other three variables. This design also randomized the order of tests conducted on the same machine. Energy density is listed for reference in the test matrix, shown in Table 13, but is not an independent parameter. Some of the process parameters were held constant across all builds in order to satisfy the build number constraint. Based on the literature review, these settings were selected as most likely to result in high quality builds and were originally selected for use in all builds:

- Layer thickness of 40 microns
- Laser power of 195 W (original plan)

- Substrate preheating of 80 °C
- Alternating laser path with scan rotation per layer of 90° (angle is set by the Concept M2 machine that only supports 90° rotation)

However, an early build attempt on the Concept M2 machine at Aerojet Rocketdyne revealed that the energy density delivered by a laser power of 195 W was unworkable. The energy density of this test build, 67 J/mm^3, was sufficient to drive curling of the material as the machine built the support layer underneath the specimen geometry. This distorted material poked upwards, extending well above its nominal layer. Therefore, some solid material remained above the powder surface even after recoating with fresh powder for the next layer, as shown in Figure 24. This excessive material ultimately interfered with the recoater operation, prompting the machine operator to terminate the build in order to prevent damaging the machine. It was also evident that no usable test specimens would have been generated from these build settings. The laser power was subsequently reduced across all builds:

- Laser power of 110 W (revised)

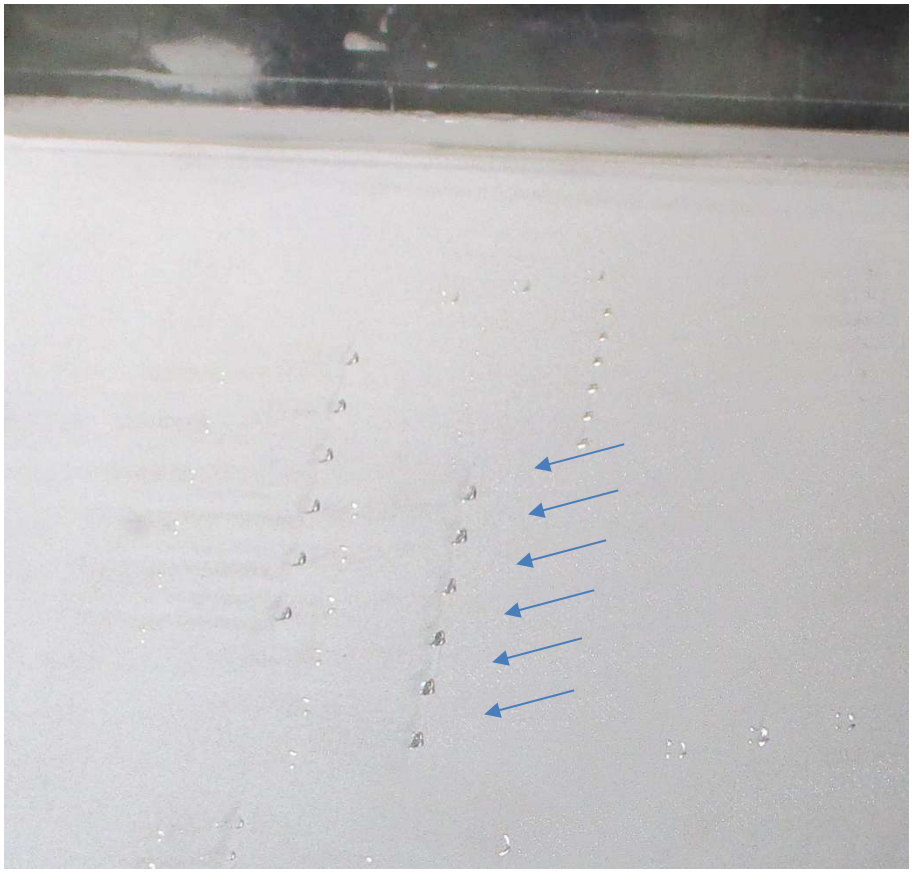

Figure 24. Solid Material from the Previous Build Layer Protrudes through the Fresh Powder Layer, Indicating the Formation of Severe Flaws that Interfere with Recoater Operation

The following parameters were varied in the design of experiment:

- Laser speed between 800 mm/s and 900 mm/s with a center point of 850 mm/s
- Hatch spacing between 70 microns and 100 microns with a center point of 85 microns

- Two machines with different laser processes: the Concept M2 at Aerojet Rocketdyne (continuous laser) and the Renishaw AM250 at SwRI (discrete laser)
- Two different heat treatment cycles

In the build matrix, the heat treatment cycle is described as either SR + HIP or NSR + HIP. This shorthand notation refers to:

- SR+HIP – Standard stress-relief and anneal (1,600 F for one hour) followed by hot isostatic pressing
- NSR+HIP – Alternative NIST stress-relief and anneal (1,475 F for four hours) followed by hot isostatic pressing

In all cases, the hot isostatic pressing (HIP) was performed at 2,050 F and 14,750 psi for a period of four hours.

Table 13. Design of Experiment

Build No.	Pattern	Scan Speed (mm/s)	Hatch Spacing (µm)	Heat Treat Cycle	Machine	Energy Density (J/mm^3)
1	---	800	70	SR+HIP	Concept M2	49.1
2	++-	900	100	SR+HIP	Concept M2	30.6
3	+-+	900	70	NSR+HIP	Concept M2	43.7
4	-++	800	100	NSR+HIP	Concept M2	34.4
5	Center Point	850	85	SR+HIP	Concept M2	38.1
6	++-	900	100	SR+HIP	Concept M2	30.6
7	+++	900	100	NSR+HIP	Renishaw AM250	30.6
8	-+-	800	100	SR+HIP	Renishaw AM250	34.4
9	Center Point	850	85	SR+HIP	Renishaw AM250	38.1
10	+--	900	70	SR+HIP	Renishaw AM250	43.7
11	--+	800	70	NSR+HIP	Renishaw AM250	49.1
SR = Standard stress-relief; NSR = Alternative NIST stress-relief; HIP = hot isostatic pressing						

The DTMM structure database targets two key attributes that influenced HCF strength based on fracture surface observations:

1. Internal porosity
2. Surface roughness measured in the gage section of the HCF specimens

The characteristics of the internal porosity include number, size, morphology, and spatial distribution of the pores. This data was acquired from the microstructure samples using standard metallurgical methods (i.e., destructively section, mount, grind, polish, and observe in microscopes). This data served as a surrogate to represent the porosity of the HCF specimens in each build which could not be sectioned before testing.

The surface roughness was measured using an areal scan of surfaces within the gage section of the HCF specimens before they were tested.

Quantitative microstructure characterization maps microstructural quantities to a digital form amendable to machine learning. In a conventional approach, one would selectively describe the state of a structure with

measures such as phase size distribution, volume fraction, morphology, etc. intuitively, relying on the previous knowledge of the materials system. In addition to the enhanced likelihood of considerable loss of microstructural information in the adoption of such ad-hoc approaches, employment of traditional characterization methods, such as linear intercept, leads to a tedious and inefficient microstructure quantification. Therefore, the adoption of a universal systematic and statistically robust methodology is of paramount importance to provide a distinctly reliable estimate of the microstructure for digital-based methods.

In this program, we use n-point correlation functions, also known as n-point statistics, as a statistical tool, which has shown to address the above hurdles [Fullwood, 2010; Cecen, 2016]. The n-point correlation functions are hierarchical statistical microstructure descriptors, which systematically provide more information as the order of the statistics increases. For instance, the fundamental 1-point statistics, $f(h)$, captures the probability associated with finding a phase of interest, known as the local state (h), in a random discrete point of microstructure and it clearly corresponds to the volume fraction of the selected phase. At the next hierarchical level, 2-point statistics, $f(h, h'|\boldsymbol{r})$, captures the correlation between every two points that are separated by vector $\boldsymbol{r}$. Mathematically, 2-point correlation function computes the probability density of locating specific phases (h and h') at the discretized head and tail of a vector $\boldsymbol{r}$ randomly thrown into the microstructure. The complete set of n-point correlation functions provides a thorough microstructure representation.

In the development of the DTMM, 2-point statistics, the first-order spatial correlation, has proven to encompass all the required information to uniquely reconstruct microstructure with high precision. Some interpretable information can be readily gained from the 2-point correlation results. For instance, if the microstructure possesses a prevailing shape, the average morphology and orientation can be captured. Before delineating the details of the 2-point correlation function, terminologies that will be referred to in later sections must be introduced. "Local state" corresponds to the entire attributes that describe the material locally. The attributes can be a combination of composition, crystal lattice structure, and phase identifier. Therefore, the definition of the local state is tied to the length scale and in literature is denoted by h. For instance, the microstructure of a Ni-base superalloy demonstrated in Figure 25(a) in the given length scale comprises two local states, the cuboidal dark shaded γ′ precipitates and the bright γ channels. The interpretation of the microstructure can be given by "microstructure function", $m(x, h)$, which defines the probability density of identifying the unique local state h in position x. Knowing that the acquired structure images are often in digital and discretized format, local states are labeled as n = 1,2, … in a discrete grid on spatial bins.

The 2-point correlation function in a discretized domain is expressed by

$$f_t^{hh'} = \frac{1}{S}\sum_{s=0}^{s=1} m_s^h \, m_{s+t}^{h'} \tag{1}$$

where S represents the total number of discretized bins or voxels, m_s^h denotes the discretized microstructure function that reflects the volume fraction of phase h in voxel s (the probability density of locating phase h at bin s), and t bins the vector space, enumerates the spatial bins and specifies the size of the prescribed vector. The schematic of a simplified discretized structure with two phases is depicted in Figure 23(b). By assigning 0 and 1 to the white and gray phases, the example values of microstructure functions become $m_{(1,2)}^0 = 1$ and $m_{(1,2)}^1 = 0$. Fullwood et al. [Fullwood, 2010] established an efficient procedure for fast computation of 2-point correlations by employing a fast Fourier transform (FFT) approach that is important for dealing with large datasets. It is important to recognize that the correlation function is denoted as auto-correlation if $h = h'$ (e.g., f_t^{11}) in the equation above and cross-correlation (e.g., f_t^{12}) otherwise.

For an illustration, an artificial periodic honeycomb structure with two local states and its corresponding auto-correlation function is displayed in Figure 25. Niezgoda et al. [Niezgoda, 2008] demonstrated that for a given microstructure with H number of total local state, $H - 1$ spatial correlation functions suffice to fully

represent microstructure, which is essentially the number of independent correlation functions. Therefore, only the demonstrated autocorrelation carries adequate structural information. In such a structure with a dominant feature shape and periodicity, the morphology and feature spacing is promptly recognized in the correlation function map.

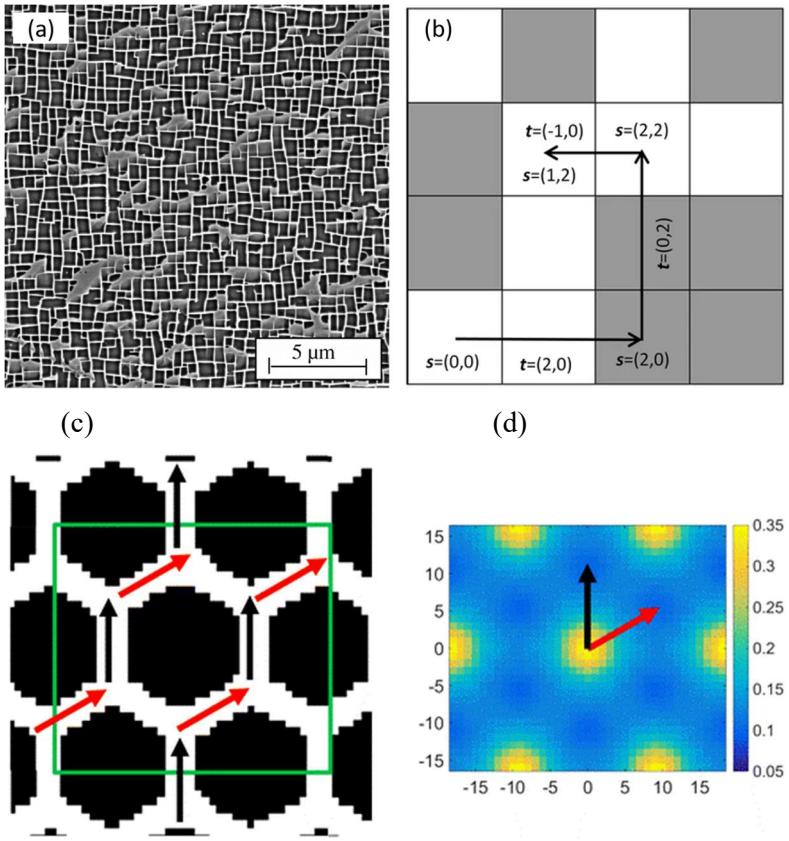

Figure 25. (a) SEM image of the two-phase CMSX-8 single-crystal Ni-base superalloy, (b) schematic of a binned structure displaying indexing and vector notations, (c) artificial periodic honeycomb structure to demonstrate a discretized two-local state periodic structure, and (d) the corresponding autocorrelation of white phase [Cecen, 2016].

These 2-point statistics are still high-dimensional. Therefore, methods to reduce the order so that features can be extracted from the structure is one approach. The most common method, often the basis of many ML methods, and the one employed here, is principal component analysis (PCA). PCA is a linear transformation technique that projects an ensemble of multivariate, correlated variables to a space with an orthogonal uncorrelated basis. The important information is extracted and represented by a new small set of variables called principal component (PC) scores.

In theory, the PCs are directions along which the variation of the data is maximized and are identified sequentially so that they are provided in descending order by the extent of the variation each explains. In practice, the mathematical algorithm of PCA involves implementing Singular Value Decomposition (SVD) on the matrix $F_r^n = [f_r^n]_{n \times p}$ in which each row is comprised of the vectorized 2-point statistics of each microstructure. Hence, for microstructure n, the PCA decomposes the descriptor vector with the entries of 2-point correlation function to the following linear combination,

$$f_r^n = \sum_{i=1}^{p-1} \alpha_i^n \, \phi_{ir} + \tilde{f}_r \tag{2}$$

where α_i^n is the coordinate of microstructure n in the new space denoted as weights or PC scores, $\emptyset_{ir}$ is the corresponding orthogonal basis vectors, $\widetilde{f_r}$ is the ensemble average of the 2-point correlations of all microstructures with the vector size r and p is the selected number of bases of the new space. Essentially, in this equation, PC scores signify the weight of the spatial pattern demonstrated by their associated basis vectors.

D. INTERNAL POROSITY – DATA ACQUISITION AND ANALYSIS

It is essential to recognize that the overall pore structure status, comprising of porosity type, shape, and spatial distribution, is the foremost contributing factor to fatigue crack formation. Characterizing porosity state only by volume fraction is inadequate in incorporating critical information for robust model linkages between structure and fatigue strength. Ideally, one would conduct an X-ray computed tomography (CT) of the critical section of the component, or in this case the gage section of the HCF specimens. However, while feasible, this is time-consuming and expensive, at least at this time, and outside the scope of this project. Instead, microstructure samples were metallurgically characterized to serve as representations of the porosity in the gage section of the fatigue specimens. The microstructure samples were sectioned in the longitudinal (build) direction so that the variation in the degree of porosity along the building direction could be examined on the exposed cross-section. In total, ten images were captured along the build direction from bottom to top, each with 1.8 × 1.3 mm field of view. Figure 26 depicts the schematic of the imaging strategy. The images were later stitched together, representing an area of 23.4 mm^2. A sample image of the pre-HIP'ed porosity structure is shown in Figure 26.

In order to quantify the revealed features, the 2-point correlation statistics framework described above is used. Figure 27 elaborates on the transformation of a sample raw image to the corresponding stitched image statistical representation. It consists of four steps:

1. Conversion of RGB images to grey-scale
2. Improvement in the contrast of the images using adaptive histogram equalization (AHE). The feature edges and contrast are enhanced locally in the adaptive approach.
3. Binarization of the grey-scale images by adaptive image binarization framework. It involves choosing a local threshold based on the first-order statistics (local mean intensity) at the neighborhood of each pixel. The pixels associated with porosities are assigned as zero, and the dense matrix pixels are set as one.
4. Removal of the detected surface features and porosities smaller than the specified threshold. The pores with a diameter lower than 20 μm are eliminated since their influence on the HCF properties is insignificant relative to the larger pores. Furthermore, the artifacts that might be introduced to the surface due to polishing and sample preparation are treated as well.

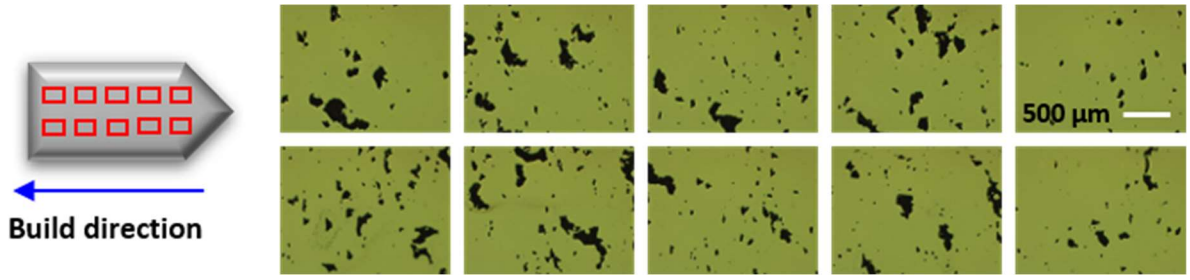

Figure 26. Optical imaging strategy of the Inconel 625 microstructure specimens at 50 × magnification and ten equally-spaced locations.

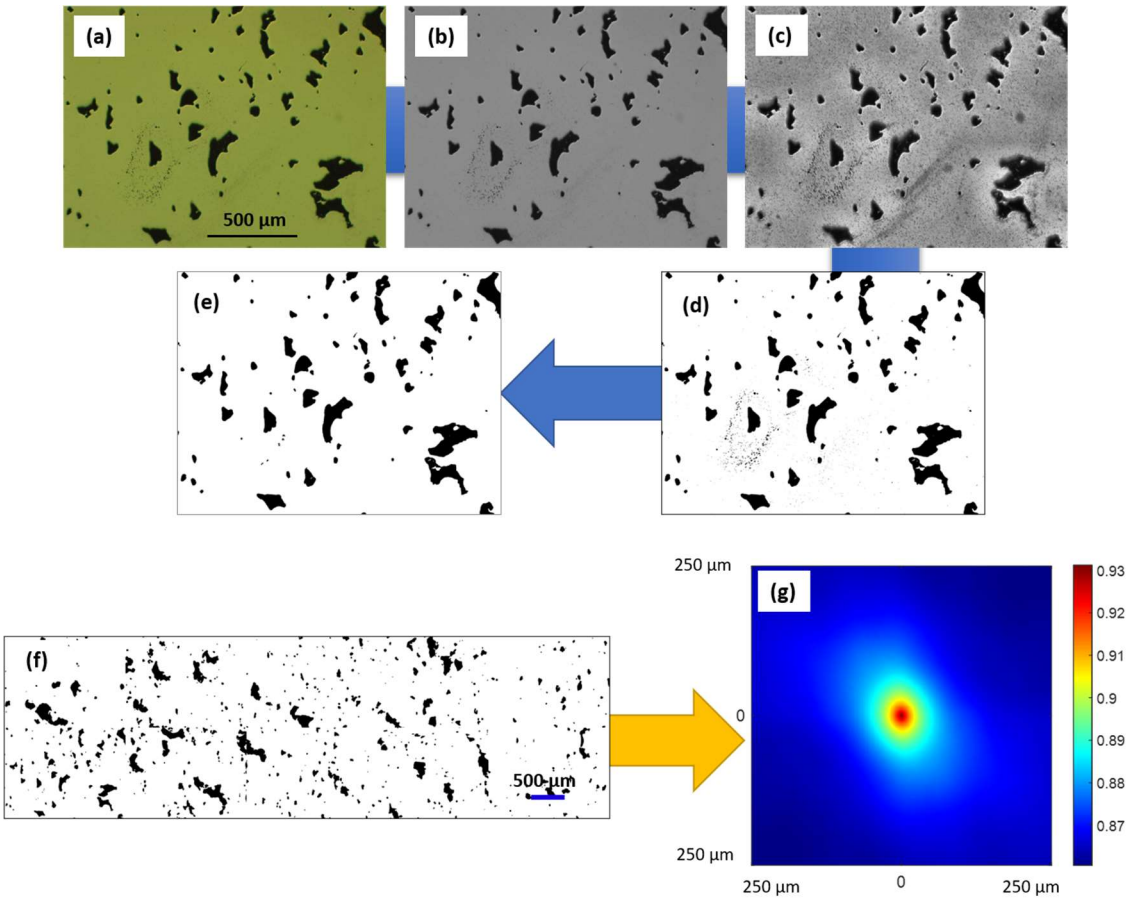

Figure 27. Image processing and quantification workflow of the optical porosity images illustrating the (a) raw image, (b) step 1, (c) step 2, (d) step 3, (e) step 4, (f) stitched image of the ten samples from one surface, and (g) 2-point correlation statistical representation.

Even though metallographic methods are a satisfactory approach for demonstrating the methodology, it should be recognized that they suffer from shortcomings. In general, no standard procedure exists for metallographic imaging of porosity that specifies the details such as a suitable choice of magnification, the total number of captured images, location, and focus adjustment. Moreover, it is a destructive approach and labor intensive at the sample preparation stage. In future application of the DTMM, this same general workflow can be applied from data acquired by X-ray CT (XCT), which is a commonly used non-destructive technology for inspection of the overall integrity of critical parts by detecting and revealing internal defects such as cracks, discontinuities, and porosities in three-dimensional (3D) space.

From the nine total microstructure samples manufactured under identical processing parameters with each build, an average of five underwent the metallographic procedure for porosity characterization (55 total over the 11 builds). The samples were selected from different locations on the build plate, shown in Figure 23, to detect any conceivable pattern that can be later attributed to the position of samples on the build plate. One of the microstructure specimens from each build was in pre-HIP'ed condition while the rest were subjected to the HIP process. The binarized 2D pore structure of the pre-HIP'ed samples manufactured by Concept M2 and Renishaw systems are shown in Figure 28 and Figure 29, respectively.

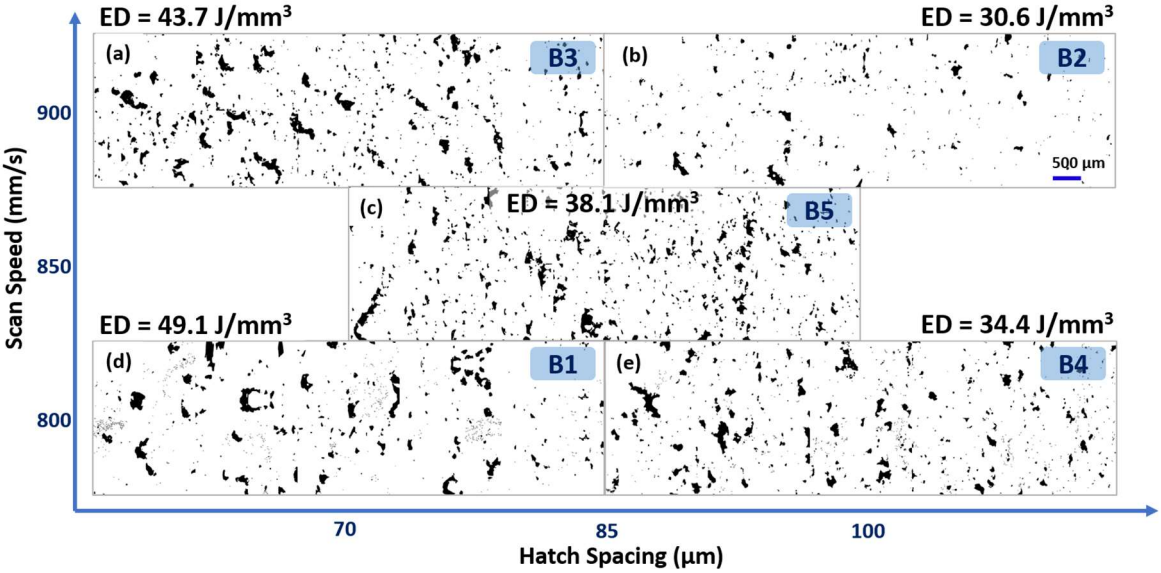

Figure 28. 2D porosity survey of microstructure samples from builds 1-5 (B1-B5) manufactured by Concept M2 system. The energy density (ED) is specified for each build.

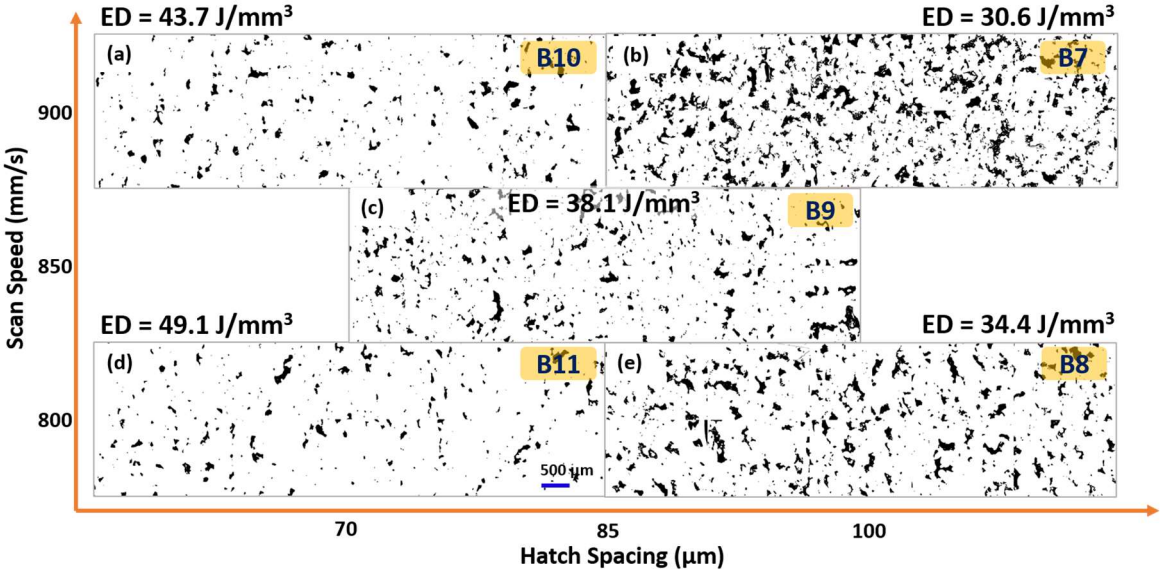

Figure 29. 2D porosity survey of microstructure samples from builds 7-11 (B7-B11) manufactured by Renishaw system. The energy density (ED) is specified for each build.

The as-built images from the Concept M2, Figure 28, do not reveal any discernible pattern of pore evolution with variation in scan speed and hatch spacing. However, it is readily recognized that the B2 specimen exhibits the highest density and the smallest pore sizes. The as-built images from the Renishaw, Figure 29,

show a more intuitive trend. Increasing both hatch spacing and scan speed resulted in a more pronounced porous structure in build 7 which is associated with the least energy density; on the other hand, the combination of process parameters for build 11 with the highest energy density level led to the best densification quality.

In order to justify the discrepancy observed between the porous structures of Figure 28 and Figure 29 with nominally identical processing parameters, the difference between the continuous and discrete laser modes of Concept M2 and Renishaw machines has to be investigated. In general, the porosity of the Concept M2 samples is considerably lower than the Renishaw system for this set of parameters. One admissible explanation is that despite the fact that point distance, exposure time, and move time variables in discrete laser mode have been adjusted to match the target scan speed to the ones in continuous mode, the obtained energy densities are not necessarily identical. In the Renishaw machine with discrete laser operation, the laser is switched off during the move time, which causes the actual energy density of the pulsed mode to be lower than the continuous mode with the same parameters. Therefore, the overall lower energy input to the powder bed gives rise to diminished densification of builds 7-11. Furthermore, the situation is exacerbated with the smaller laser spot size in the Renishaw system. The laser spot size affects the melt pool geometry. Even though high precision is achievable with smaller laser diameters, lack of fusion pores are created when hatch spacing is increasingly exacerbated by the smaller laser diameter.

A similar observation was made for the post-HIP'ed samples, where substantially higher porosity levels were observed for those manufactured by the Renishaw system (except for build 11). The porosity images of the samples built at the front and back of the build chamber are illustrated in Figure 30 for the Concept M2 and Figure 31 for the Renishaw. The structure of the Concept M2 specimens (Figure 30) located at the front of the build plate, marked by the black dot on the visible build plate edge, proves the effectiveness of the HIP process in eliminating the large irregular pores. At the same time, it is observed that the small gas entrapped spherical pores have remained intact. However, the structure of the specimens located at the back of the platform, in builds 4-6 with the lower energy density, stands out with considerably large pores. This situation is intensified for the Renishaw specimens (Figure 31) where the porosity state is comparable to the pre-HIP'ed ones, particularly in builds 7-9 associated with the low energy density levels. Such observations raise questions about the efficacy of the HIP process in the densification of the parts with an extremely high porosity fraction. It can be inferred that post-build procedures such as HIP can not necessarily mitigate the severe defects promoted as a result of an unsuitable combination of processing parameters.

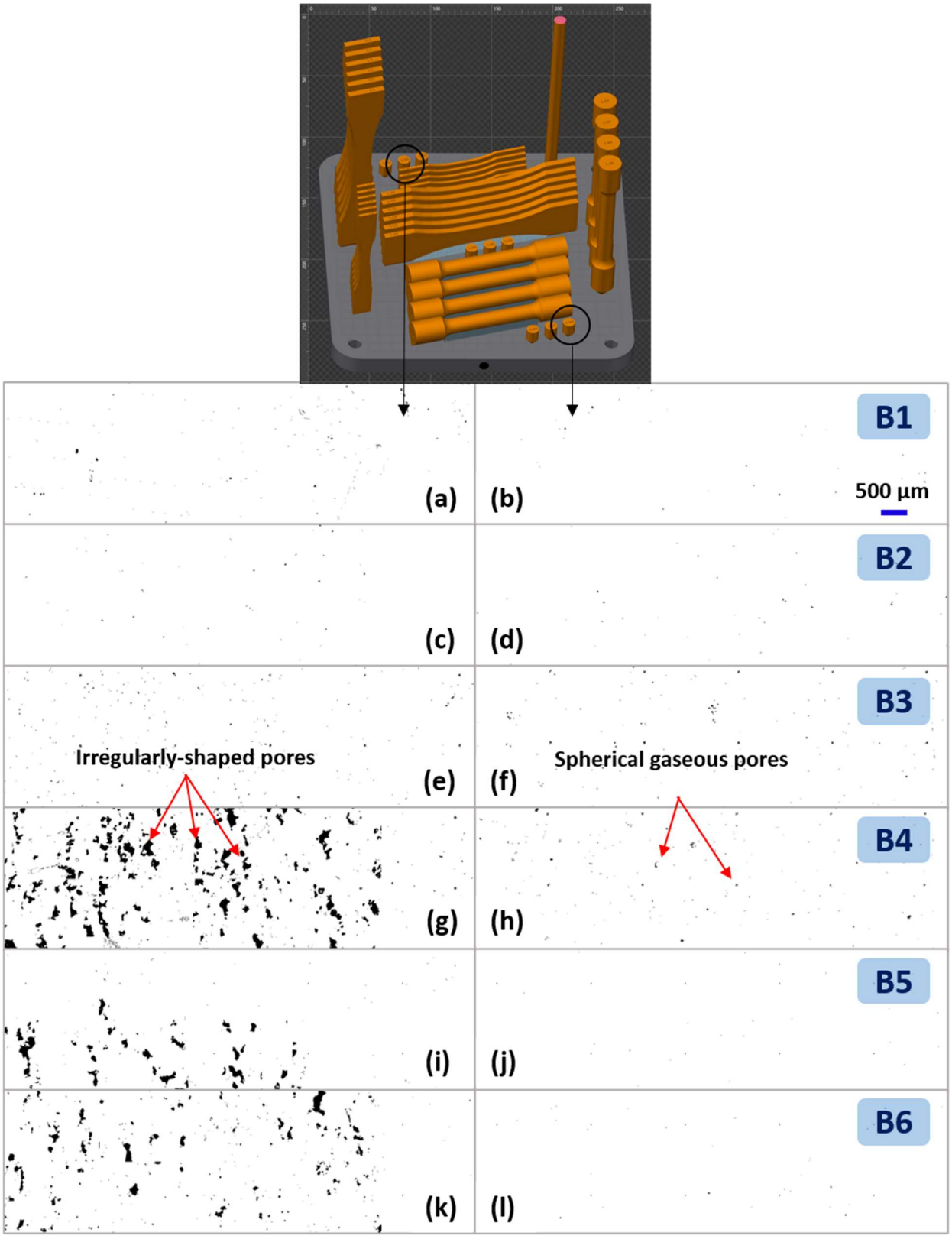

Figure 30. Post-HIP'ed structure of builds 1-6 manufactured by Concept M2 system obtained from microstructure samples located at the front and back of the build plate.

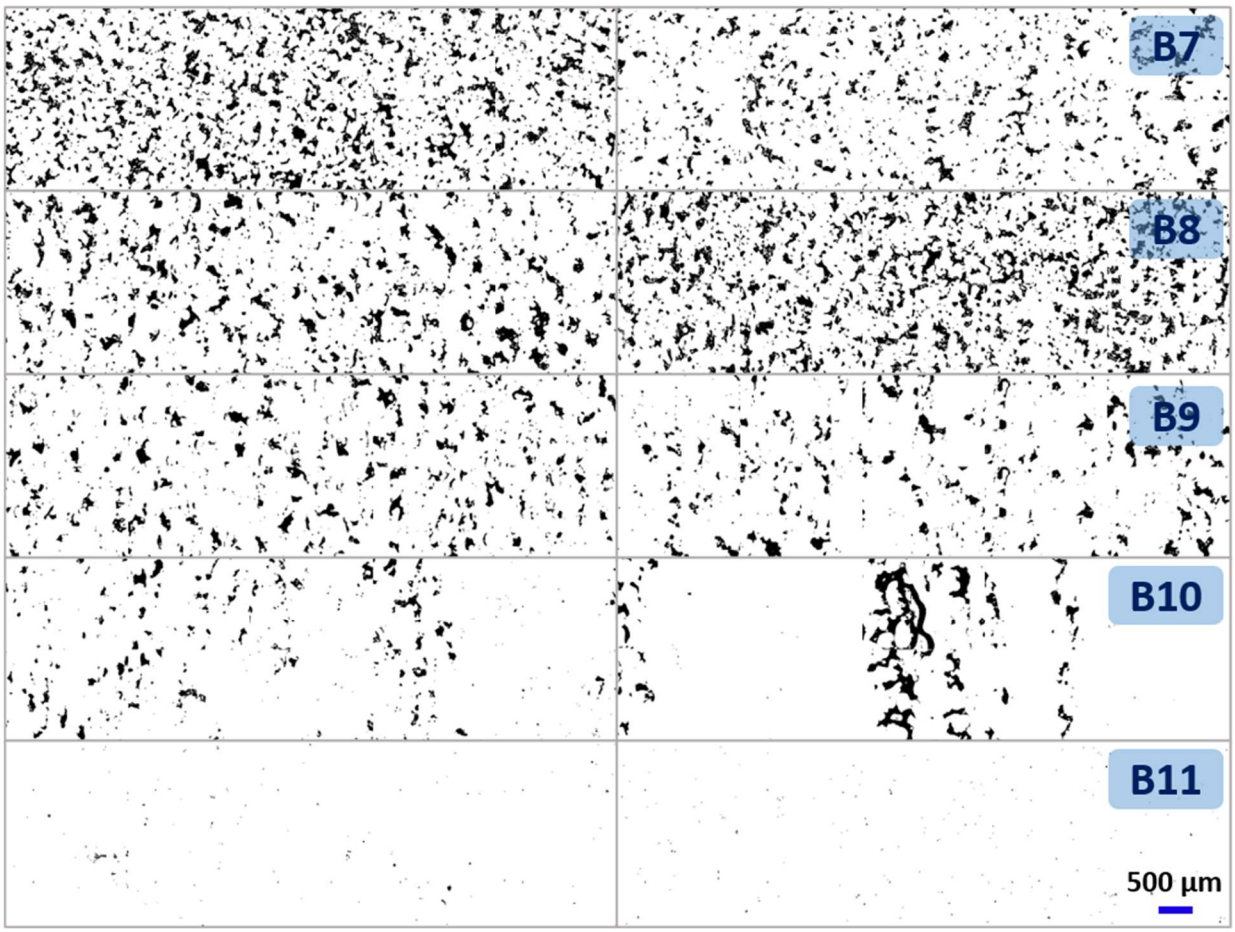

Figure 31. Post-HIP'ed structure of builds 7-11 manufactured by Renishaw system obtained from microstructure samples located at the front and back of the build plate.

The porosity volume fraction of the 50 microstructure samples from the 11 builds are summarized in the bar plot of Figure 32. The pre-HIP'ed samples (denoted BN-35) are signified by the black-bordered and glowing bars. The samples with the best structural integrity in pre- and post-HIP'ed conditions are from builds 1, 2, 3, and 11. Note that builds 2 and 6 were manufactured under the exact same parameters with the Concept M2 machine. Even though the pre-HIP'ed samples reveal similar results, the post-HIP'ed samples of build 6 exhibited high porosity volume fraction. This observation suggests that the discrepancy observed between the pore structure of builds 2 and 6 is an indication of the uncertainty of the currently uncontrolled parameters involved in the adopted manufacturing process.

Evidently, the porosity volume fraction alone is not adequate in characterizing the state of the porosities since it excludes critical information such as pore size, morphology, and distribution. Such information is fully entailed in the 2-point statistics maps. Figure 33 depicts the 2-point auto-correlation of the white-white phase of three different microstructure samples of build 5. The statistical representation has successfully differentiated between their distinct porous structure. The size and morphology of the pores are reflected through the central features in the maps.

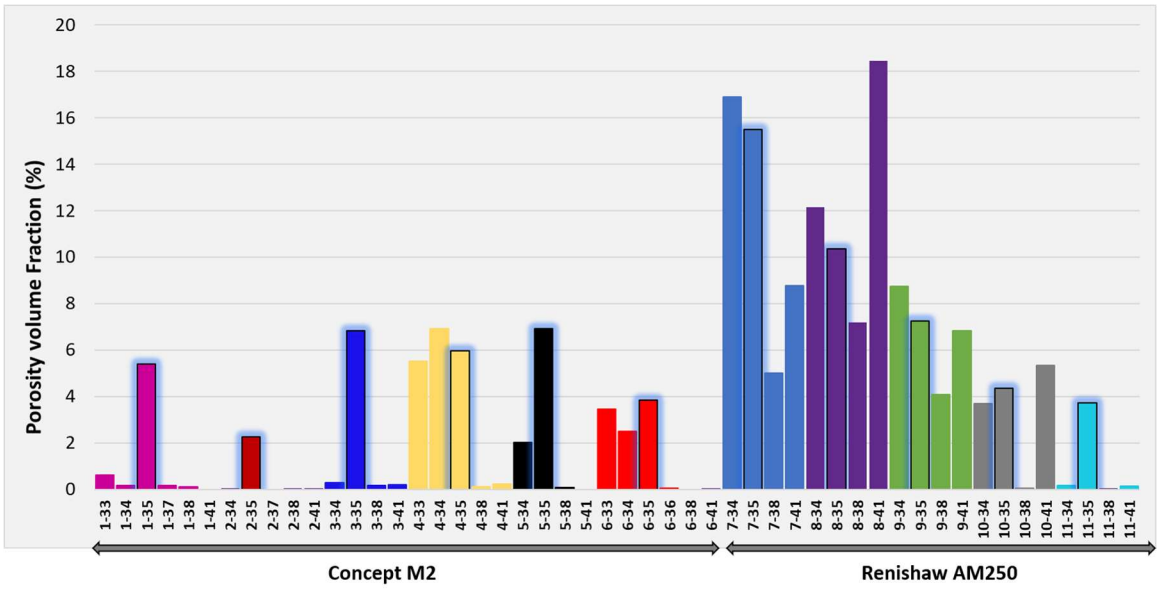

Figure 32. Porosity volume fraction of 50 microstructure samples in pre- and post-HIP'ed conditions from eleven manufactured builds.

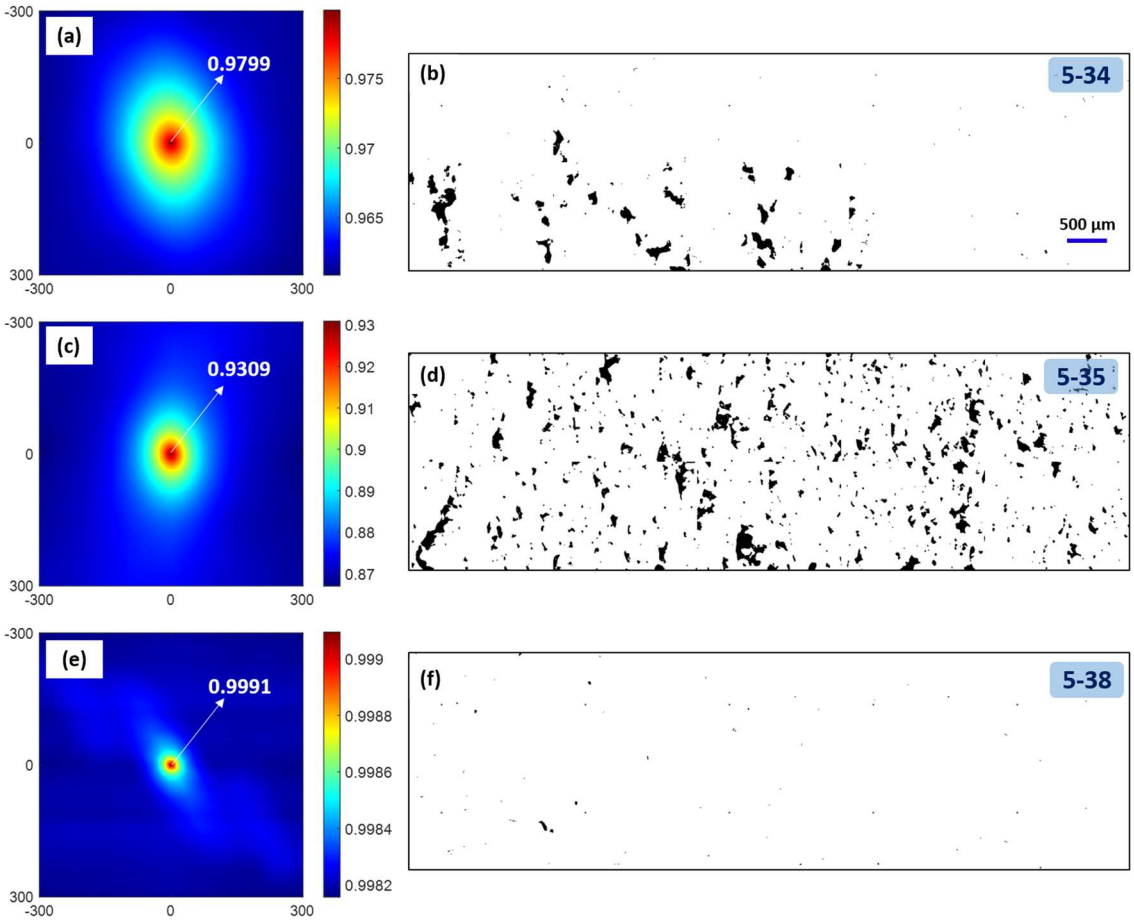

Figure 33. The binarized optical images and their statistical representation of three microstructure samples processed under the same manufacturing parameters in pre-HIP'ed (d) and post-HIP'ed (b and f) conditions.

Samples 5-34 and 5-38 shown in Figure 33 were both subjected to the HIP process. Although 5-38 was successfully densified, an uneven distribution of large pores is still present in the structure of 5-34. The differentiation is clearly reflected in the corresponding 2-point correlation maps. Compared to the pre-HIP'ed sample (5-35), the larger average pore size in sample 5-34 as well as its lower volume fraction is captured by the size of the central feature and the higher 2-point correlation value of the [0 0] index, respectively.

After implementing PCA on the 2-point correlation results of the microstructure samples, the first PC was found to capture 99.97 % of the total variance. Therefore, the data can be represented in a 1-dimensional PC space, as shown in Figure 34. The low-dimensional representation of the data in PC space clearly distinguishes the subtle variation in the pore structure of microstructure samples. The results strongly agree with the prior observations. Along the PC1 axis, the most positive coordinates correspond to the highly densified HIP'ed structures with the lowest porosity volume fraction. As the PC1 value reduces towards negative coordinates, the higher content of large pores becomes prevalent in such a way that the sample 8-41 with the highest porosity volume fraction of about 18%, is located at the extreme negative coordinate. It should be noted that the representation in Figure 28 also supports the observation that samples of builds 7, 8, and 9 have the greatest deviation from the ideal pore-free structure.

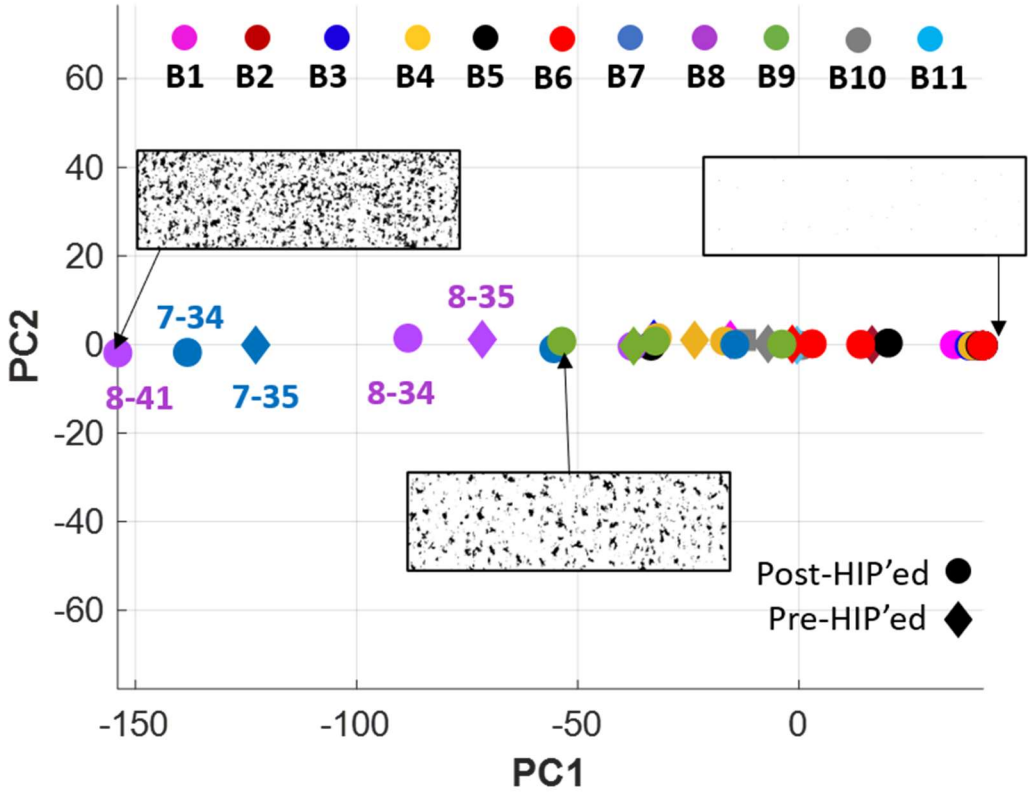

Figure 34. Low-dimensional representation of the porosity database in the PC space.

E. SURFACE ROUGHNESS – DATA ACQUISITION AND ANALYSIS

The data acquisition and quantification workflow for surface roughness of the fatigue specimens follows the steps shown in Figure 35. The surface roughness was acquired using the Zygo Zegage 3D optical profiler system. The Zygo 3D profiler setup and a sample 3D surface generated by the Mx data analysis software (version 7.5.0.1) are shown in Figure 36. The measurement scans were carried out on the gage section of the fatigue specimens prior to fatigue testing. Data were collected from two parallel wide and narrow sides,

constituting four scans for each specimen, illustrated in Figure 37. The details of the scan area orientation and location on both XY and Z fatigue specimens are provided in the schematic of Figure 38. The corresponding scan sizes on the wide and narrow sides are 4.2 × 2.3 mm and 3.9 × 2.3 mm, respectively. The scan area dimensions were selected as the minimum area that encompasses statistically similar surface features compared to the entire gage section for time-effective data acquisition. Once the raw height data were collected by the instrument, it underwent a series of post-processing by Zygo Mx software, including (i) surface form removal, to eliminate the influence of possible deviation of the surface form from a flat surface and (ii) data filling, to fill the voids or opening on the interior of the discrete regions. The final measurement data were exported in the format of a .xyz file for further analysis and characterization.

Figure 35. Schematic of the surface roughness characterization and quantification workflow in this study.

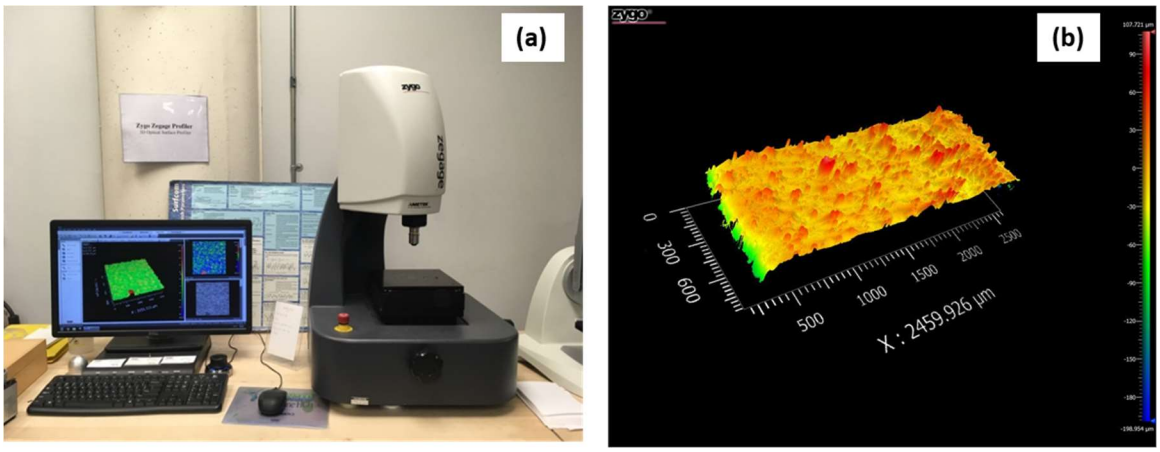

Figure 36. (a) Zygo 3D profiler measurement and analysis setup and (b) 3D surface reconstruction using Mx software.

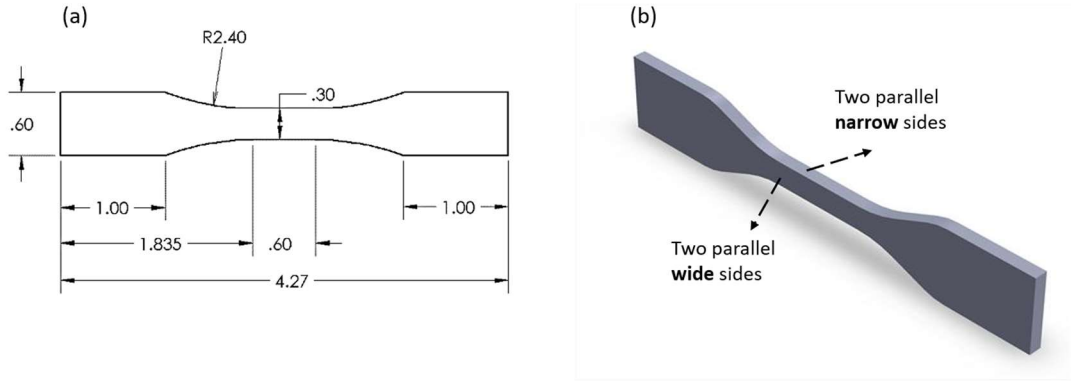

Figure 37. (a) Nominal dimensions of the small fatigue specimen and (b) position of the four roughness measurement scans in the gage section.

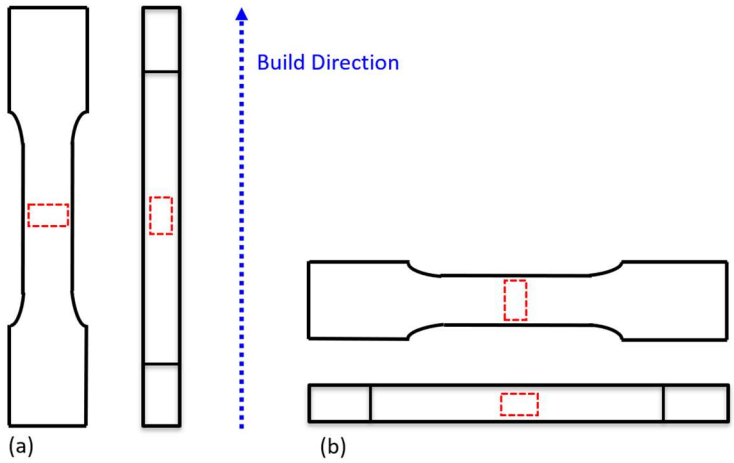

Figure 38. Illustration of the roughness scan area with respect to the build direction for (a) Z and (b) XY fatigue specimens.

After the roughness measurement dataset was created, data cleaning and trimming were applied to treat any missing values and to adjust the scan area sizes to ensure consistency in the dataset. Figure 39 provides examples of the scan area topography captured from a wide and a narrow side of a fatigue specimen.

During the image segmentation step, the height value at each pixel was binned to represent four local states, labelled S1 for a value closest to the deepest valley, and then in order of increasing heights, S2, S3, and S4 for a pixel value near a peak. The 2-point statistics framework is adopted to quantify the generated segmented surface roughness images. Noting that for a given image with n local states, $n-1$ independent correlation functions are needed to represent the structure statistically. Hence, in the example of Figure 39 with four local states, the black (S1), yellow (S3), and red (S4) auto-correlation functions provide the full statistical quantification of the segmented roughness images, as shown in Figure 40. Hence, the surface roughness component of the structure database is comprised of a collection of three 2-point correlation maps for each scan and a total of twelve maps for every specimen.

Examples of the 3D surface profiles of the wide surfaces of the Z and XY oriented specimens as a function of scan speed and hatch spacing are shown in Figure 41 through Figure 44. In addition, recognize that builds 2 and 6 were processed under identical processing parameters and are located at the same coordinate in Figure 36. In general, it can be inferred that the Renishaw system (builds 7-11) with the discrete laser approach and slightly smaller laser spot size has led to smoother surfaces compared to the Concept M2 system (builds 1-6). The superiority of the Renishaw surfaces is more notable for Z specimens with overall smoother surfaces than the XY specimens.

Similarly, Figure 45 through Figure 48 reveal that the narrow surfaces of the Z specimens exhibit lower surface roughness than XY-oriented specimens. The narrow side relative orientation with respect to the build direction shifts by 90° from a vertical to a horizontal-type of surface in the Z and XY specimens, respectively, suggesting that the layer-by-layer fusion of powders originates rougher surfaces on 0° (horizontal) sides than 90° (vertical) ones. Furthermore, builds 7 and 8 with the low energy density level manufactured with a discrete laser scan produced the lowest range of height variation and, consequently, the smoothest narrow surfaces in the Z direction.

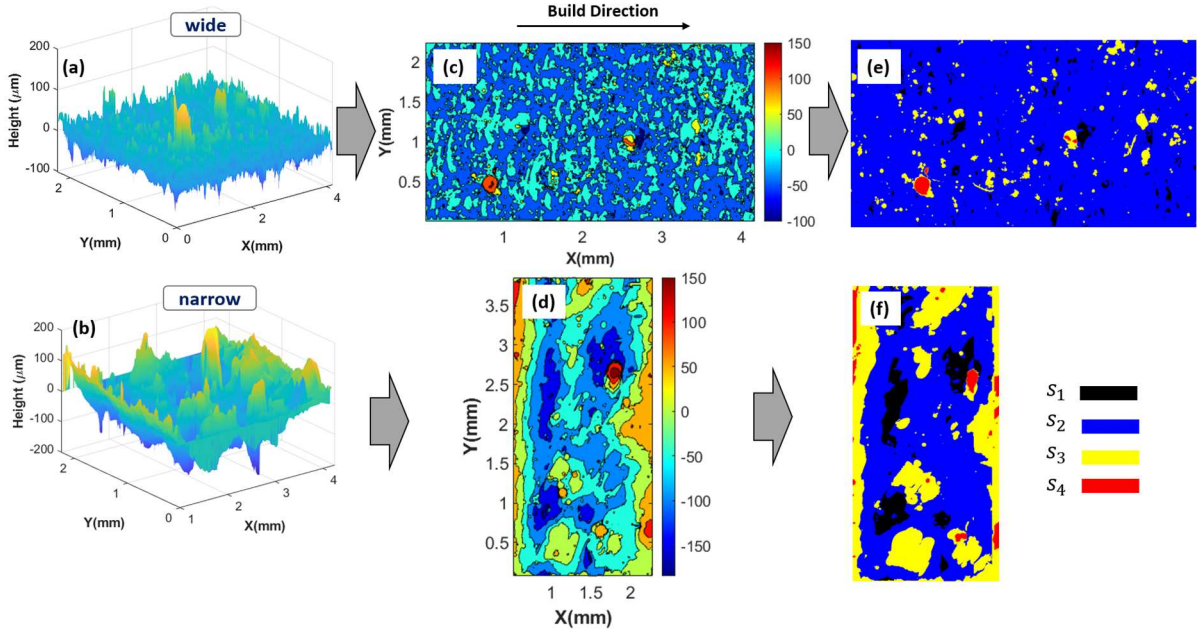

Figure 39. (a,b) 3D topography, (c,d) contour plots, and (e,f) segmented discretized representation of surface roughness.

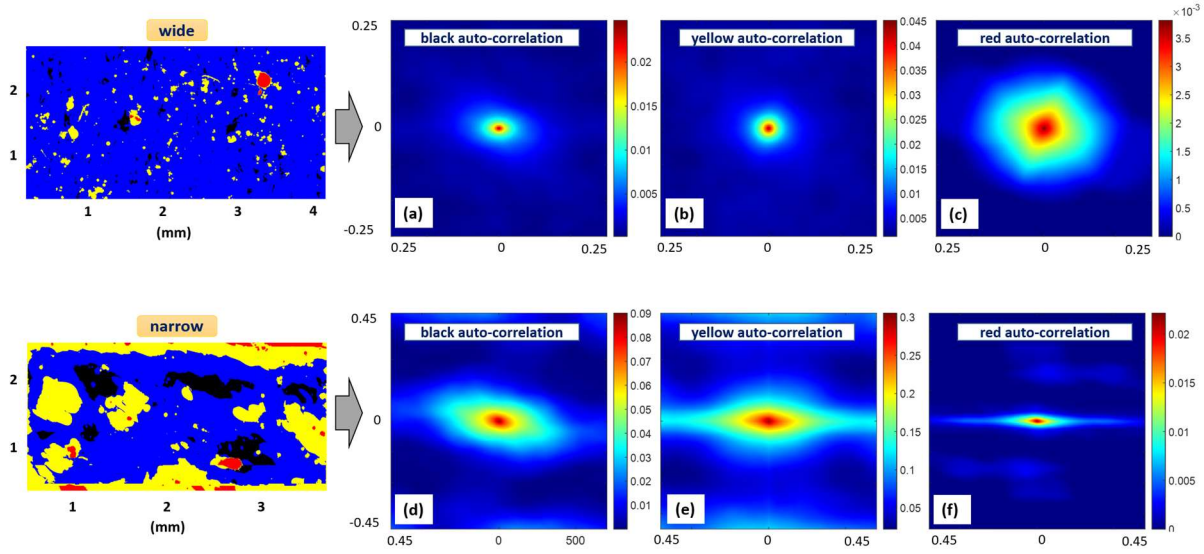

Figure 40. Statistical description of the segmented roughness maps with three local states by (a,d) black, (b,e) yellow, and (c,f) red auto-correlation functions.

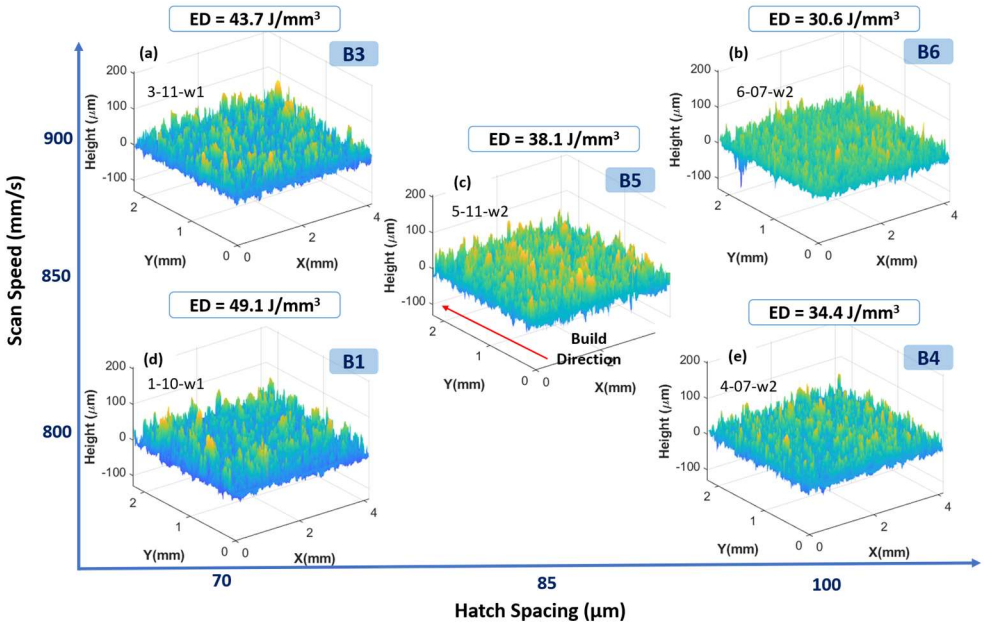

Figure 41. Examples of the areal wide surface profiles of Z specimens manufactured by Concept M2 system under variant scan speed and hatch spacing levels.

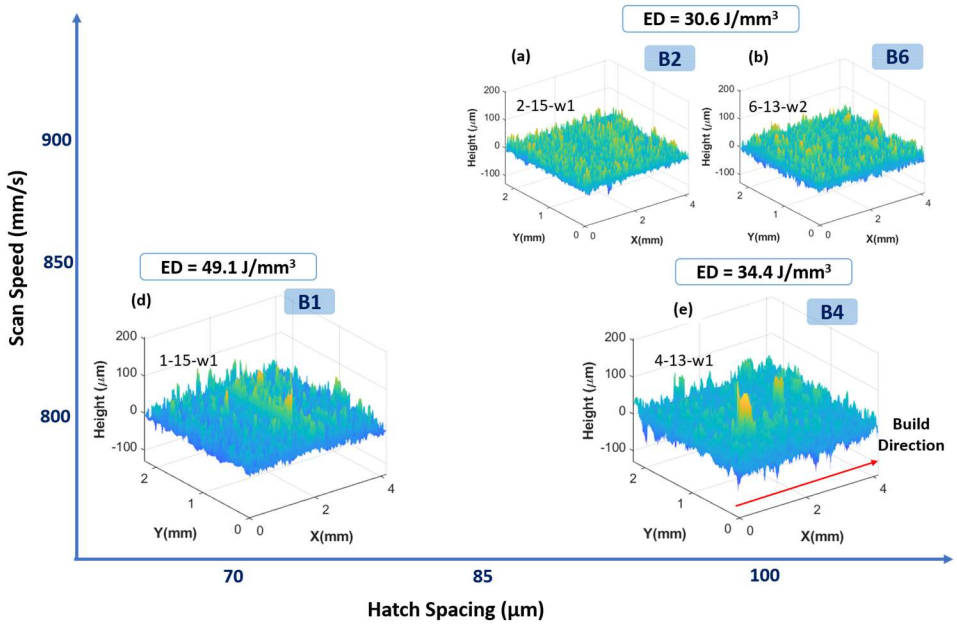

Figure 42. Examples of the areal wide surface profiles of XY specimens manufactured by Concept M2 system under variant scan speed and hatch spacing levels. B2 and B6 were both processed at 900 mm/s speed and 100 μm hatch spacing.

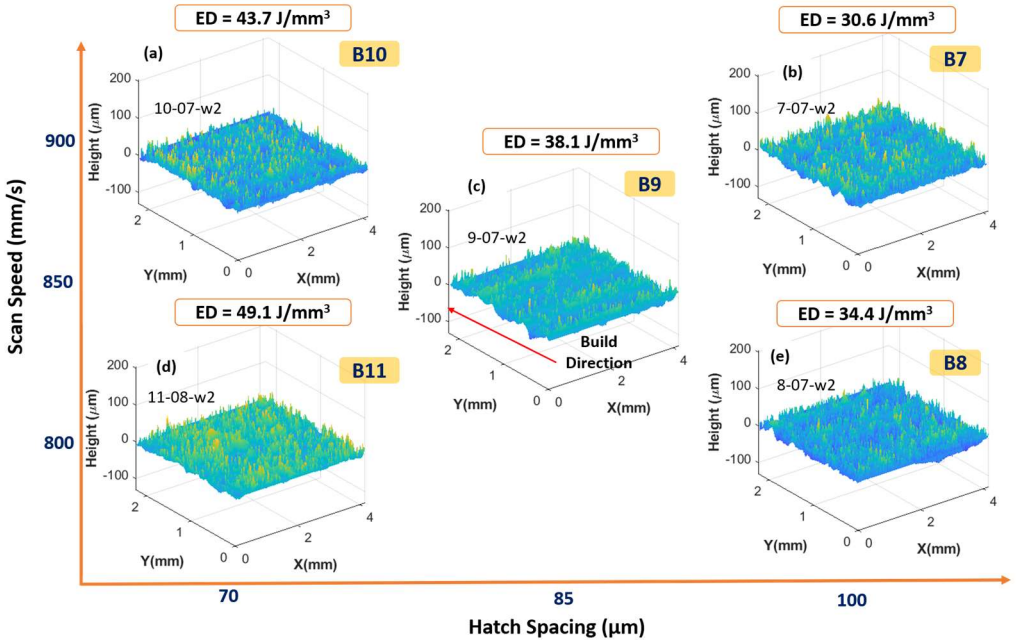

Figure 43. Examples of the areal wide surface profiles of Z specimens manufactured by Renishaw system under variant scan speed and hatch spacing levels.

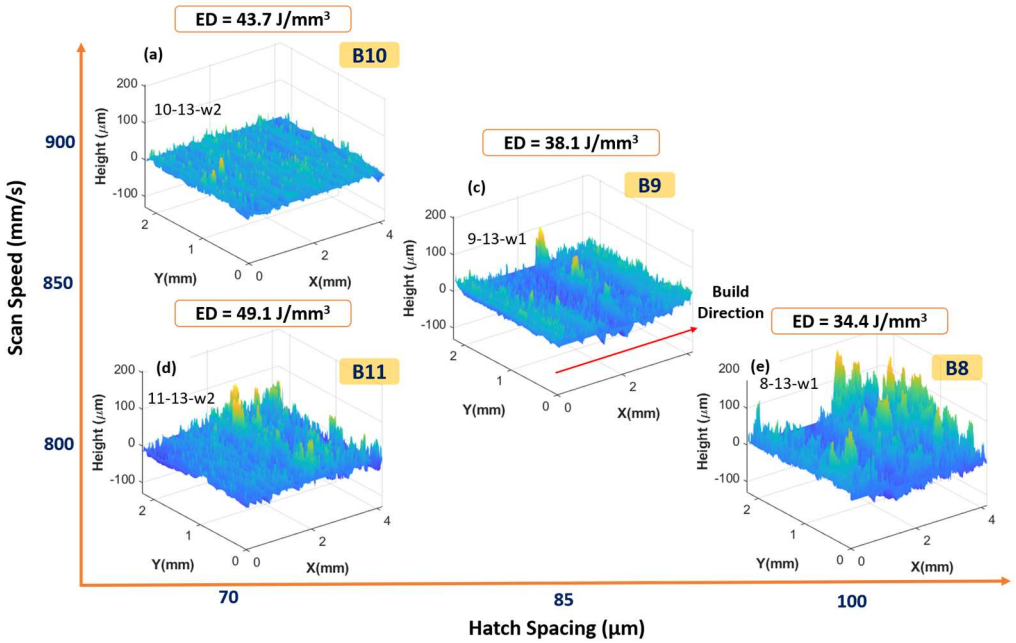

Figure 44. Examples of the areal wide surface profiles of XY specimens manufactured by Renishaw system under variant scan speed and hatch spacing levels.

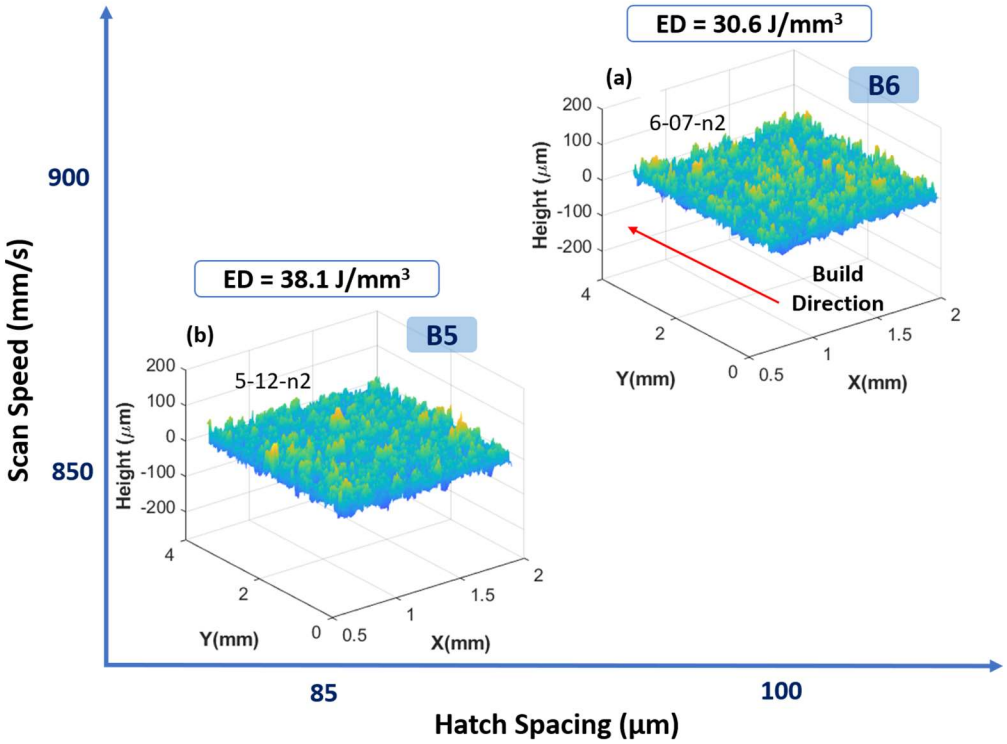

Figure 45. Examples of the areal narrow surface profiles of the Z specimens manufactured by Concept M2 system under variant scan speed and hatch spacing levels.

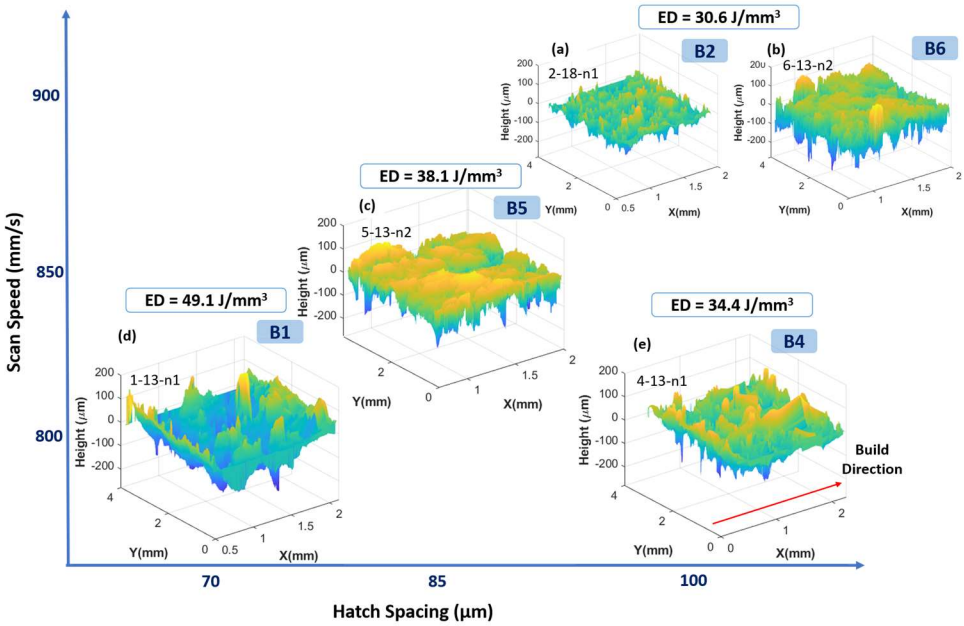

Figure 46. Examples of the areal narrow surface profiles of XY specimens manufactured by Concept M2 system under variant scan speed and hatch spacing levels. B2 and B6 were both processed at 900 mm/s speed and 100 μm hatch spacing.

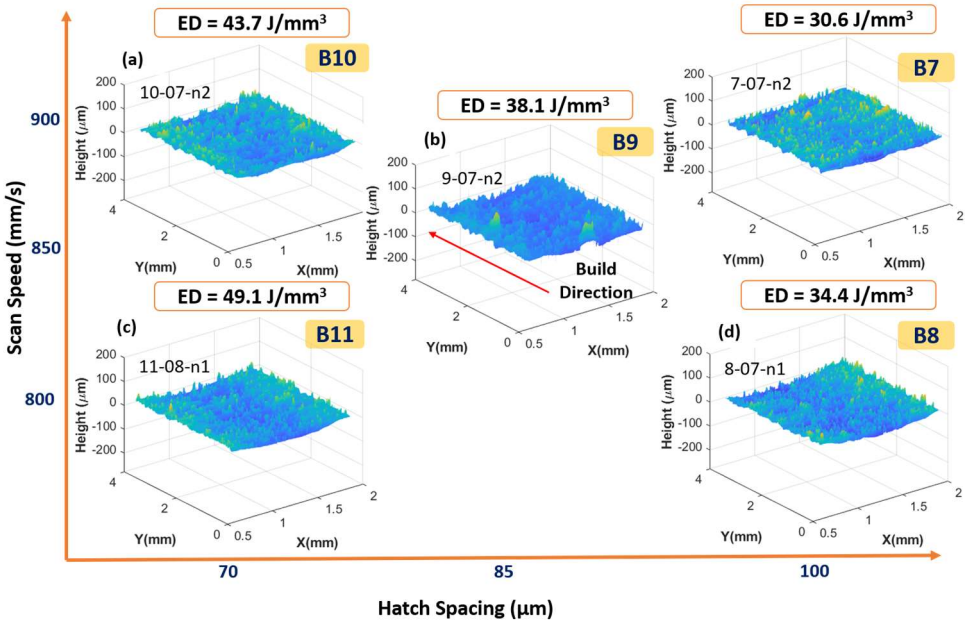

Figure 47. Examples of the areal narrow surface profiles of Z specimens manufactured by Renishaw system under variant scan speed and hatch spacing levels.

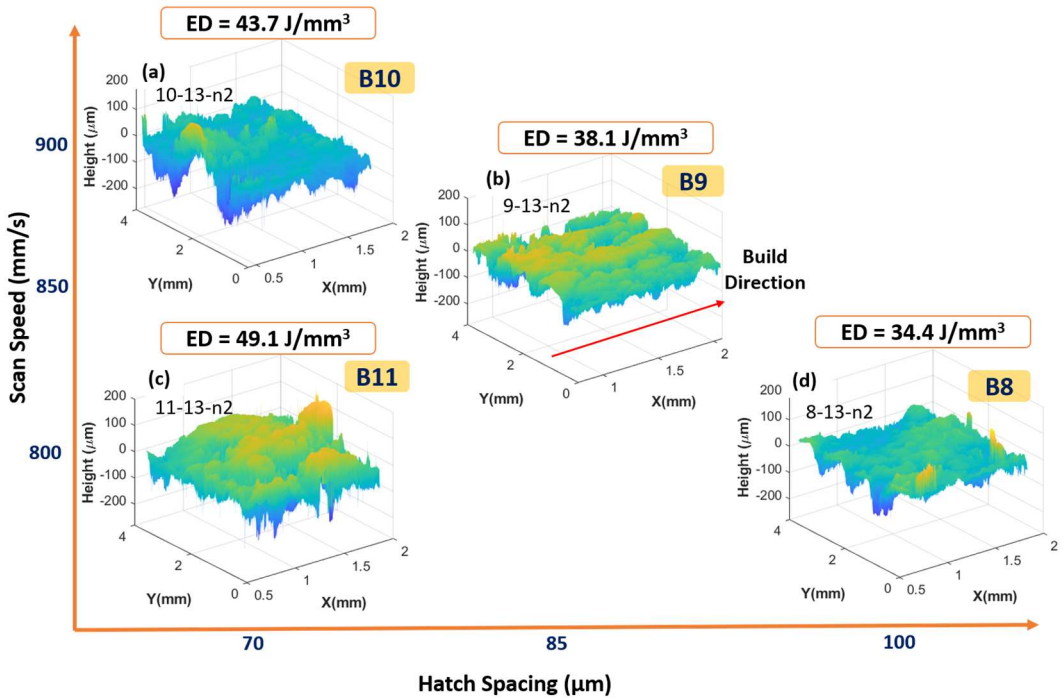

Figure 48. Examples of the areal narrow surface profiles of XY specimens manufactured by Renishaw system under variant scan speed and hatch spacing levels.

For quantitative analysis and comparison of the surface quality, the data processing, feature extraction, segmentation, and quantification is applied to the acquired surface roughness database. The transformation of the example roughness profiles shown in Figure 41 through Figure 48 to segmented images is presented

in Figure 49 through Figure 56. It is readily recognized that the surfaces are differentiated by the distribution, size, and morphology of the extracted features. For instance, all wide surfaces in Figure 49 have a quite uniform distribution of s_3 local state whereas by changing the laser mode to discrete in Figure 51, the development of smoother surfaces stands out. Furthermore, Figure 50 and Figure 52 show the increased surface roughness of the XY specimens. In particular, by increasing the hatch spacing to 100 µm at the lowest scan speed of 800 mm/s (build 8), surface quality has deteriorated under both Concept M2 and Renishaw systems.

In general, the narrow sides have developed surfaces with higher roughness. Fine surface features are produced on Z specimens of build 5 and build 6 (Figure 53), while the development of coarse features is evident in segmented images of Figure 54-Figure 56. From the illustrated segmented images, the significant role of areal characterization of surface roughness and adoption of a quantification method that can successfully differentiate between such various surface characteristics becomes clear. Before the implementation of the 2-point correlation for quantification of the surface roughness, the segmented images are converted to binarized images. Since four local states have been defined, three auto-correlation functions (e.g., black-black, yellow-yellow, and red-red) statistically represent each discretized roughness image.

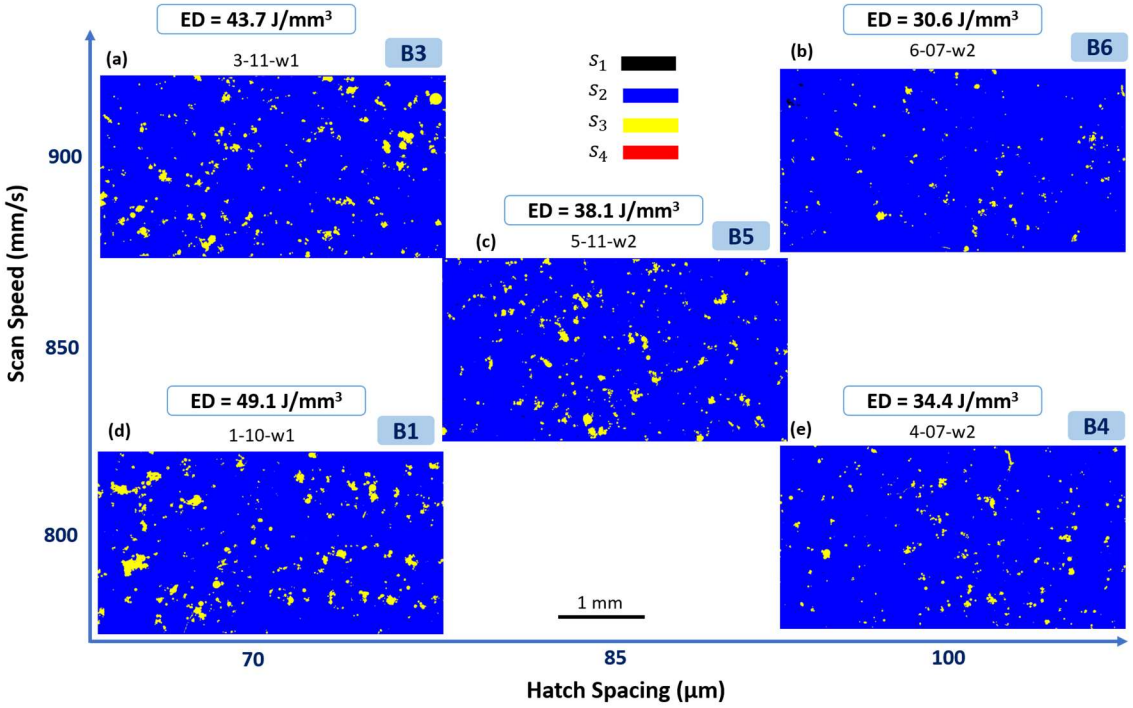

Figure 49. Examples of the roughness segmented images of the Z specimens wide surfaces manufactured by Concept M2 system under variant processing parameters.

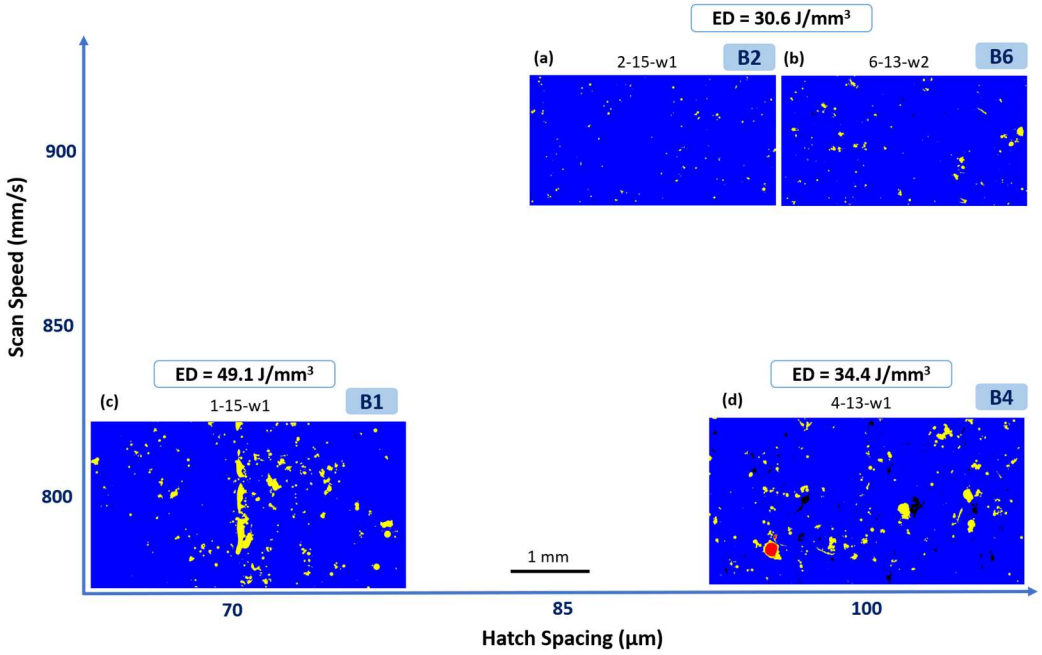

Figure 50. Examples of the roughness segmented images of the XY specimens' wide surfaces manufactured by Concept M2 system under variant processing parameters.

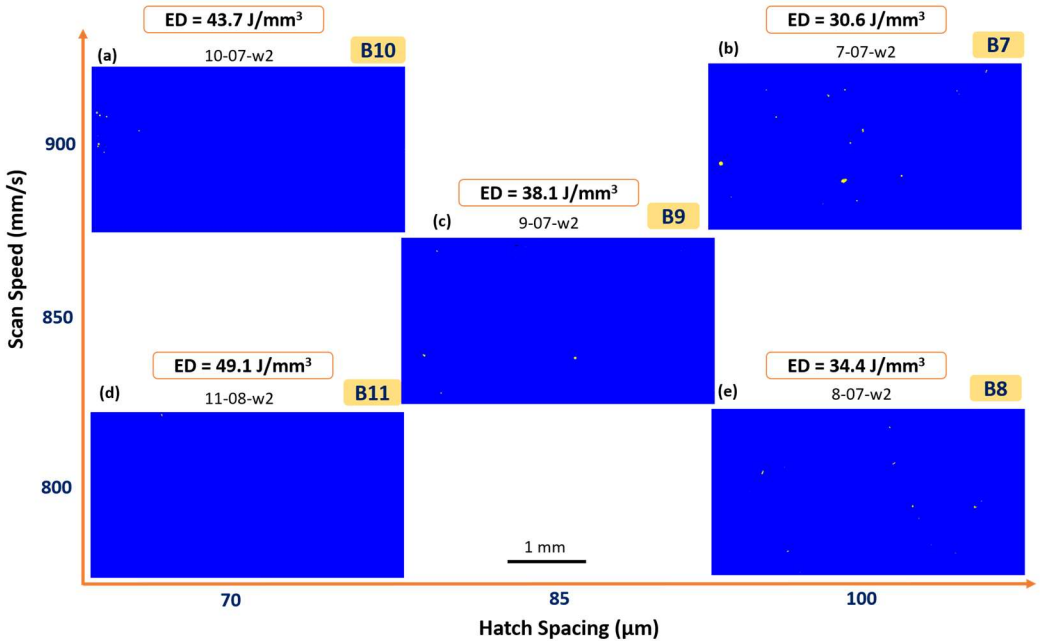

Figure 51. Examples of the roughness segmented images of the Z specimens wide surfaces manufactured by Renishaw system under variant processing parameters.

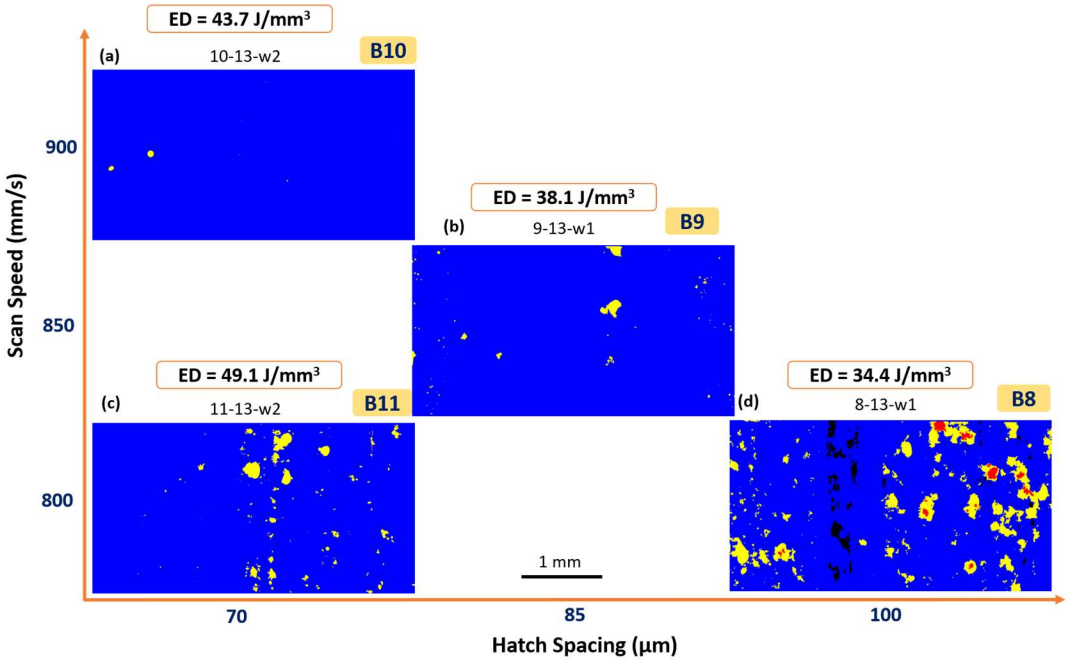

Figure 52. Examples of the roughness segmented images of the XY specimens' wide surfaces manufactured by Renishaw system under variant processing parameters.

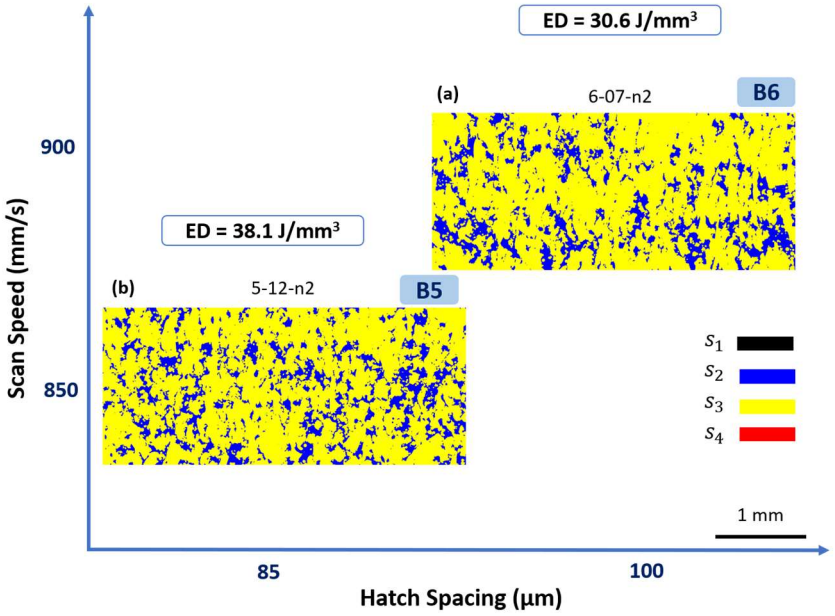

Figure 53. Examples of the roughness segmented images of the Z specimens narrow surfaces manufactured by Concept M2 system under variant processing parameters.

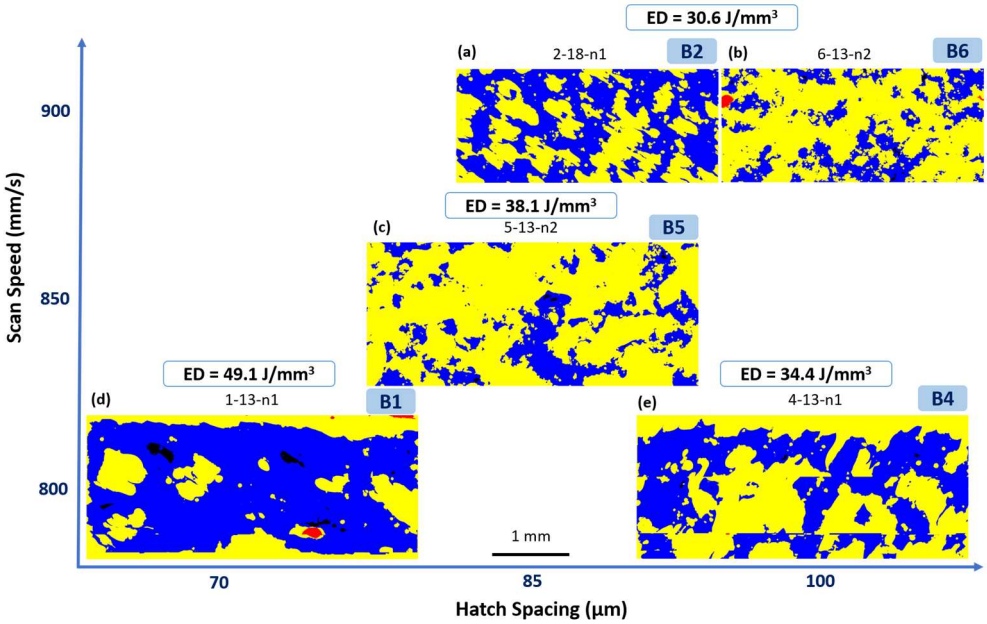

Figure 54. Examples of the roughness segmented images of the XY specimens' narrow surfaces manufactured by Concept M2 system under variant processing parameters.

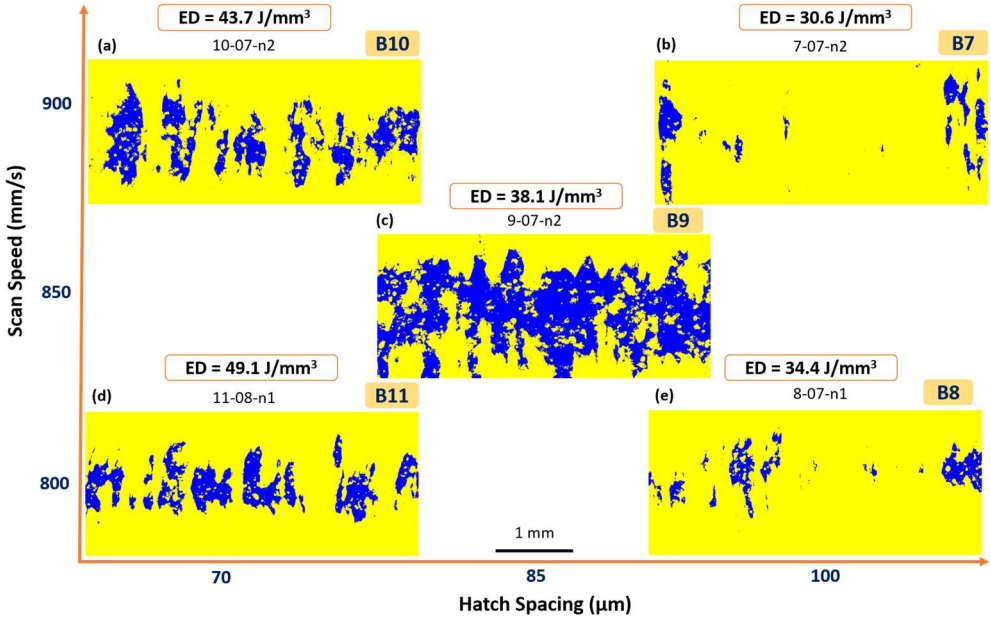

Figure 55. Examples of the roughness segmented images of the Z specimens narrow surfaces manufactured by Renishaw system under variant processing parameters.

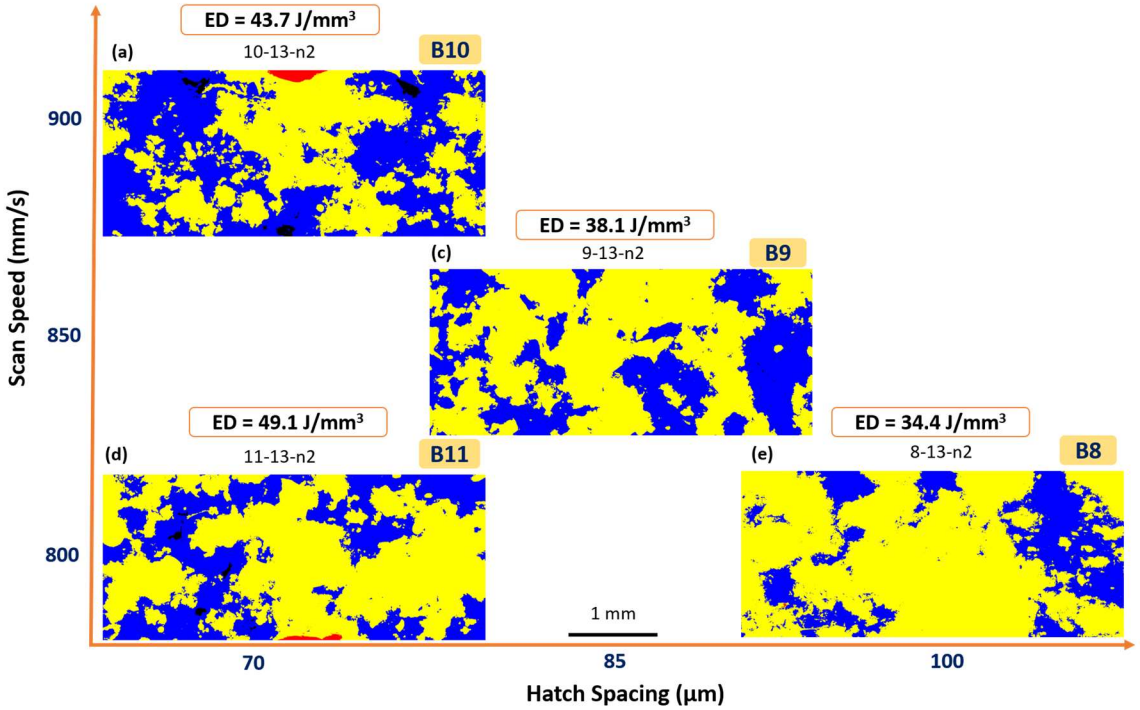

Figure 56. Examples of the roughness segmented images of the XY specimens' narrow surfaces manufactured by Renishaw system under variant processing parameters.

Three binarized images are produced for each of the surface roughness discretized images. For wide surfaces, the local state s_2 (blue) was deemed as the background and thus the binarized $s_1 - s_2$ (black-blue), $s_3 - s_2$ (yellow-blue), and $s_4 - s_2$ (red-blue) images were generated. Two examples of the segmented wide surfaces from build 8 (sample ID 8-13) and their binarized version associated with the implementation results of the 2-point correlation for each black and white image are presented in Figure 57. Note that all the computed 2-point statistics are auto-correlation of the white-white local state. The information that can be readily transferred from the 2-point correlation map is the size and morphology of the s_1, s_3, and s_4 local states from the central feature of the maps. The maximum value of the scale bars indicates the volume fraction of each extracted feature.

In the as-built condition, build 10 turned out to achieve the smoothest wide surface in both Z and XY direction. The Z specimens of builds 7, 8, and 11 also yield a narrow range of height variation while their corresponding XY specimens exhibit an increased level of roughness, particularly in build 8. Therefore, considering the combined densification and surface roughness characterization results, builds 10 and 11 processing parameters have led to the most satisfactory part quality. Considering that hatch spacing was set at its lowest level while scan speed varied from 800 mm/s to 900 mm/s, it can be inferred that within the selected range of scan speed and hatch spacing, the latter parameter is likely to exert a more pronounced influence on the structure of the additively manufactured Inconel 625.

The primary difference between the quantified porosity and roughness data is the number of derived 2-point correlation maps to represent each data point. This number was increased to three for roughness data. Given that the roughness data of two parallel wide and two parallel narrow surfaces were acquired for each specimen, a total of twelve (4×3) 2-point correlation maps represent the surface roughness condition of each fatigue specimen. In this section, the results of the wide and narrow sides are processed independently. The data merging steps for the six 2-point correlation maps of the wide side prior to the implementation of PCA is detailed in Figure 58. Similar steps were applied to merge the data from narrow surfaces. Eventually, an *n*-by-*m* matrix is obtained for each type of surface, where *n* is the total number of scanned samples, and *m* is the size of the vectorized 2-point correlation maps (6×601×601).

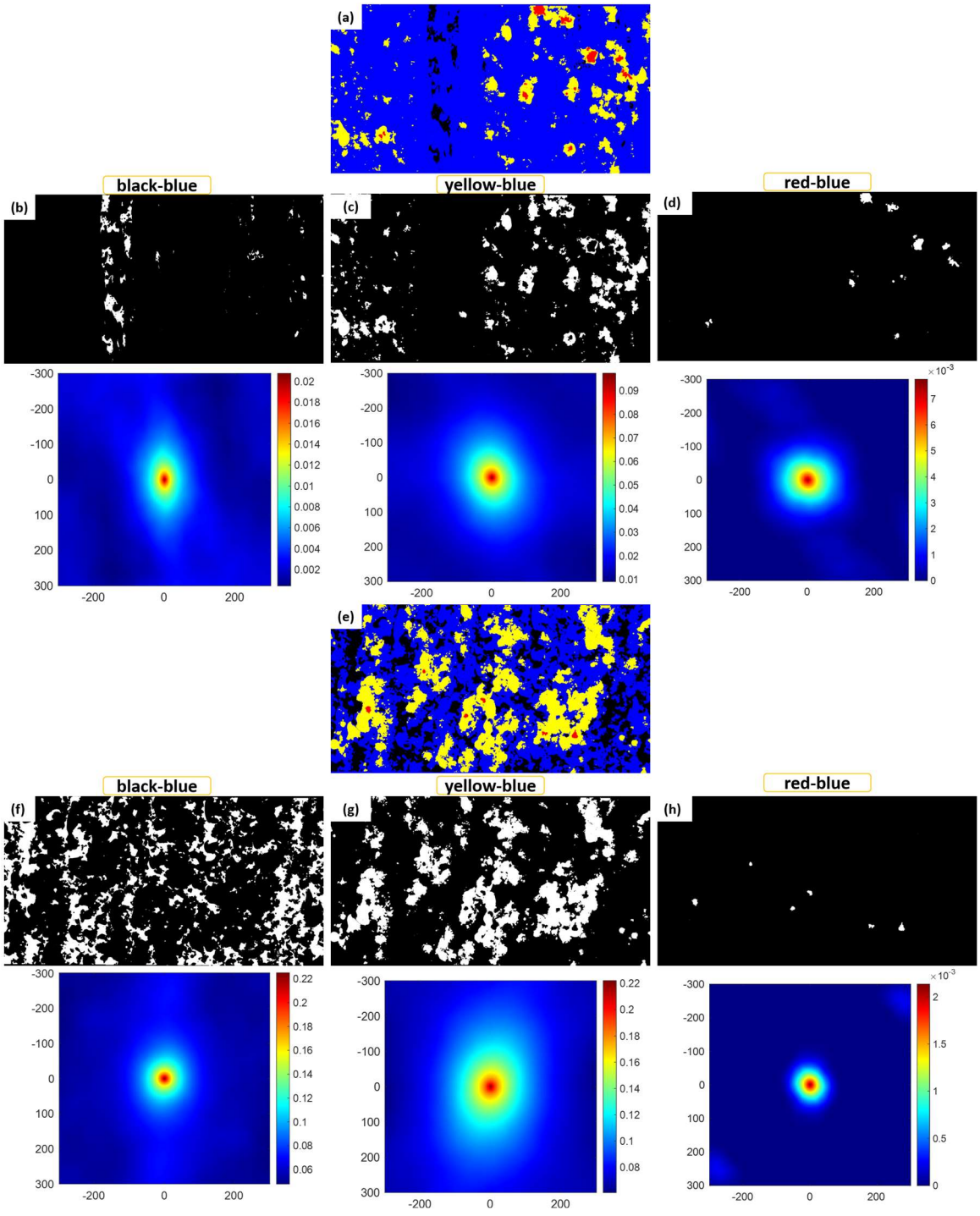

Figure 57. Binarized images and their corresponding 2-point correlation functions of the four-local state discretized surface roughness images of two parallel wide side of a fatigue specimen (sample ID 8-13).

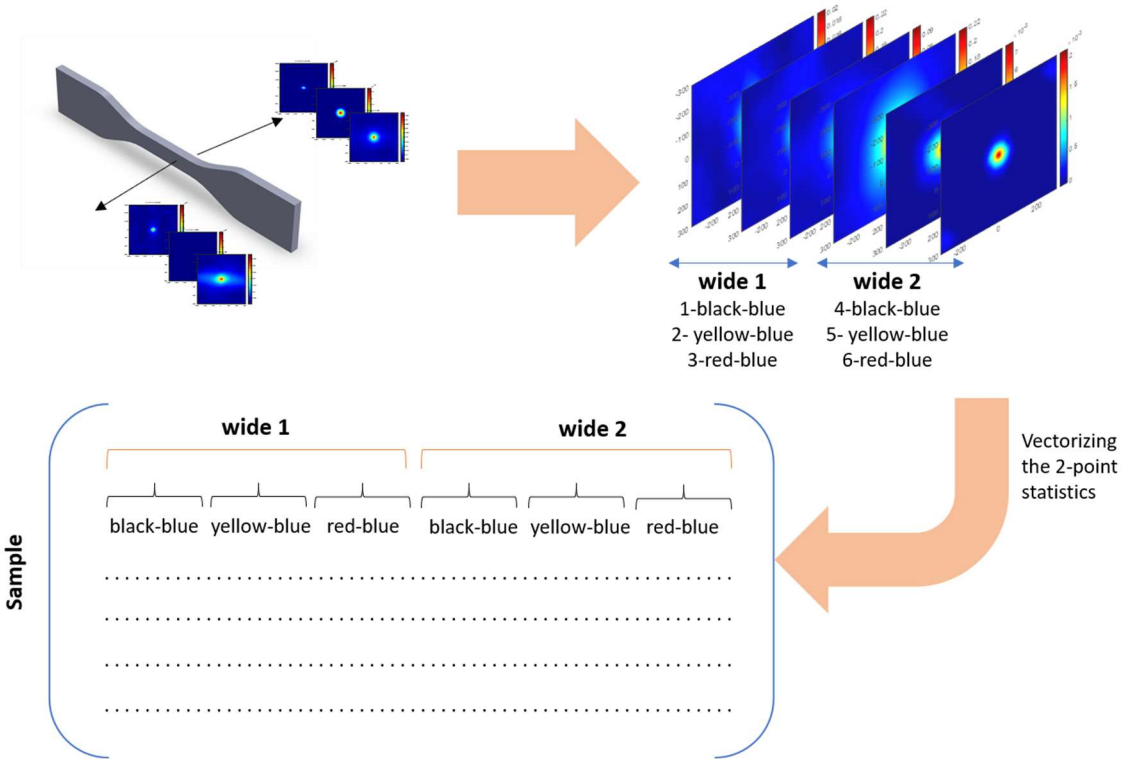

Figure 58. Schematic illustration of the rearrangement of the 2-point correlation data to generate a 2D matrix as an input for PCA.

The results of the transformation of the high-dimensional 2-point correlation data to the lower-dimensional PC-space are presented in Figure 59 and Figure 60. The orthogonal axes of the PC-space are ordered based on the extent of data variance each represents. For instance, the wide surface roughness data can be delineated by just the first PC score since it captures more than 98% of the total data variability (Figure 53(c)). The evolution of the surface features along the PC1 axis implies that as the PC1 coordinate of the sample departs from negative values, the surface roughness exhibits higher values. At the negative extreme of the PC1 axis, the data points represent the polished surfaces (the solid blue segmented images). The highest PC1 coordinate belongs to the sample from build 8 (8-13) with the coarsest surface features and a wide range of height variation. The pairs of discretized images correspond to the two parallel wide sides of the fatigue specimen.

The narrow surfaces, on the other hand, required the first two PC scores to acquire more than 98% of the data variability (Figure 54(b)). From negative PC1 to positive values, the surface quality deviates from the polished surface quality. The surfaces with PC1 close to zero have developed fine scattered surface features, and by further increase in PC1, the coarse localized features dominate the surface and s_1 and s_4 local states with the lowest and the highest valley and peaks become apparent.

This workflow demonstrates a novel approach for the characterization and quantification of the surface roughness database in a robust and systematic manner that is adaptable to ML algorithms. The resolution of the extracted features can be adjusted by the number of defined local states, and there exists the possibility to continuously add more data to the database and update the analysis. Addressing the areal features rather than profile linear features offers the unique capability to detect the minor differentiation between surfaces that can be later decisive in governing the properties sensitive to the surface features.

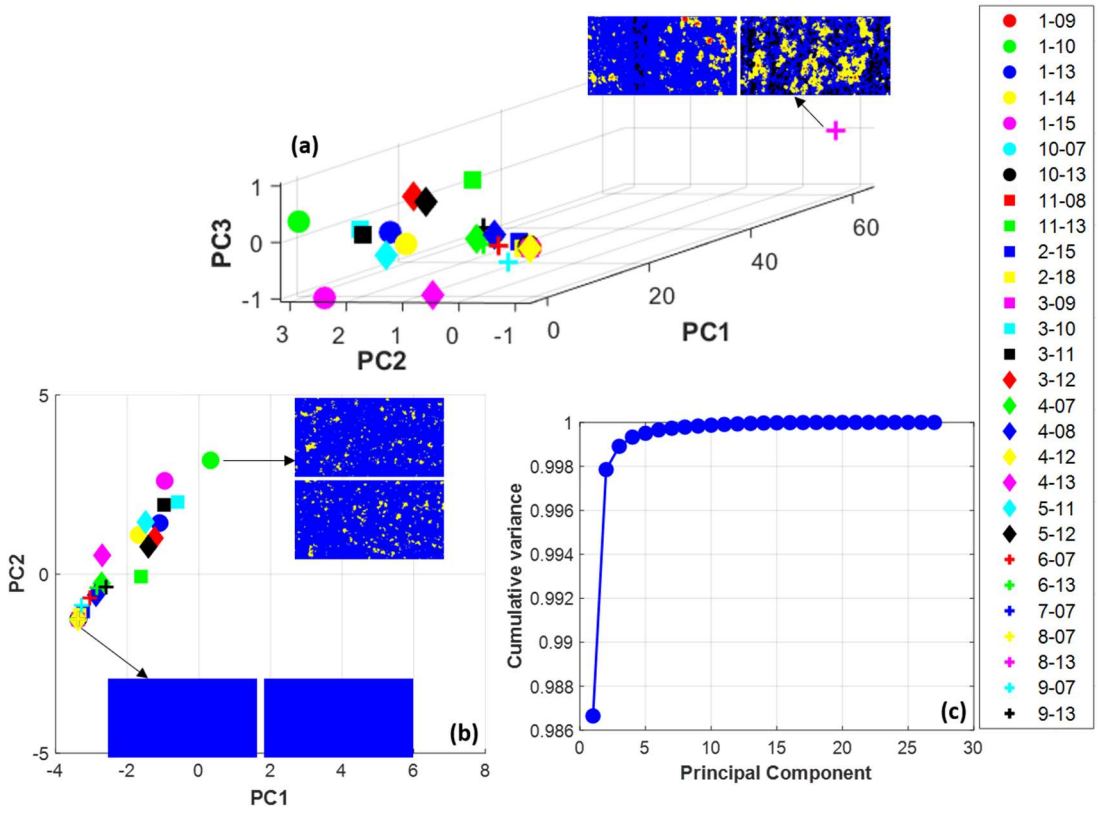

Figure 59. Low-dimensional representation of the wide surface roughness ensemble of the fatigue specimens at the (a) 3D and (b) 2D PC space. (c) Accumulative contribution of principal components to the total acquired variance.

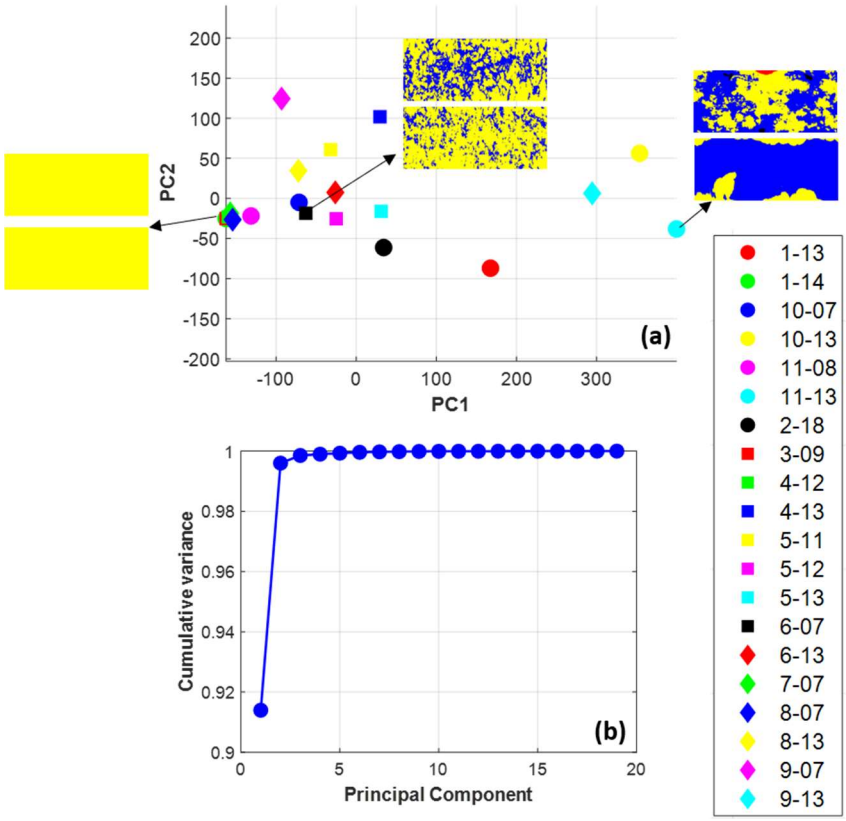

Figure 60. Low-dimensional representation of the narrow surface roughness ensemble of the fatigue specimens at the (a) 2D PC-space. (b) Accumulative contribution of principal components to the total acquired variance.

F. PROPERTY – HCF STRENGTH – DATA ACQUISITION AND ANALYSIS

The property of interest is high cycle fatigue (HCF) strength, which is generally more sensitive to the microstructure attributes than other mechanical properties such as elastic modulus, yield strength and tensile strength. Populating a stress-life (S-N) curve for assessment of the fatigue endurance limit is time-consuming and restricted by the number of specimens available to test. This limitation is addressed by adopting the step test approach [Bellows, 1999]. The fatigue strength is determined by applying a constant stress range and stress ratio, R, on a specimen for a predefined number of cycles. If failure does not occur, the applied stress range is increased (typically 5%) and cycling is continued. This process is continued until the specimen fractures. The HCF strength is computed by

$$\sigma_E = \sigma_{PS} + (\sigma_F - \sigma_{PS})\left(\frac{N_f}{N_r}\right) \tag{3}$$

where σ_E is the fatigue strength in terms of stress amplitude (one-half the stress range), σ_{PS} and σ_F denote the stress amplitude of the previous block and stress amplitude from the final block, respectively. N_f and N_r refer to the number of cycles to failure of the final step and run-out cycles, respectively. The number of run-out cycles is defined as 2×10^6 cycles in this program.

Prior to fatigue testing, HCF specimens of similar geometry were fabricated from a cold-rolled Inconel 625 sheet to generate an S-N curve to serve as a reference baseline and to verify that the step-test method provides suitable results when testing one-of-a-kind Inconel 625 specimens. This was important because several of the L-PBF specimens had unique defect features (or sometimes referred to as anomalies), and the step test enabled the relative fatigue strength to be determined for each defect feature, which was critical

for developing correlations between specific attributes of the structure and HCF strength. The fatigue tests were conducted at stress amplitudes within the range of 225 to 382.5 MPa with a fixed stress ratio of R = 0.1, and frequency of 20 Hz except for the 382.5 MPa and 337.5 MPa tests that were performed at frequencies of 10 Hz and 15 Hz, respectively. The test results were then fit to a double power-law equation:

$$\sigma_a = A\left(N_f\right)^a + B\left(N_f\right)^b \tag{4}$$

where σ_a and N_f denote stress amplitude and the number of cycles to failure, shown in Figure 61. The parameters determined by linear regression are A = 31,420 MPa/cycles, B = 217 MPa, a = -0.485, b = 0. Note that b was near zero in the regression analysis and therefore was set to zero. By doing this, B then represents the threshold stress amplitude, below which no failure is predicted.

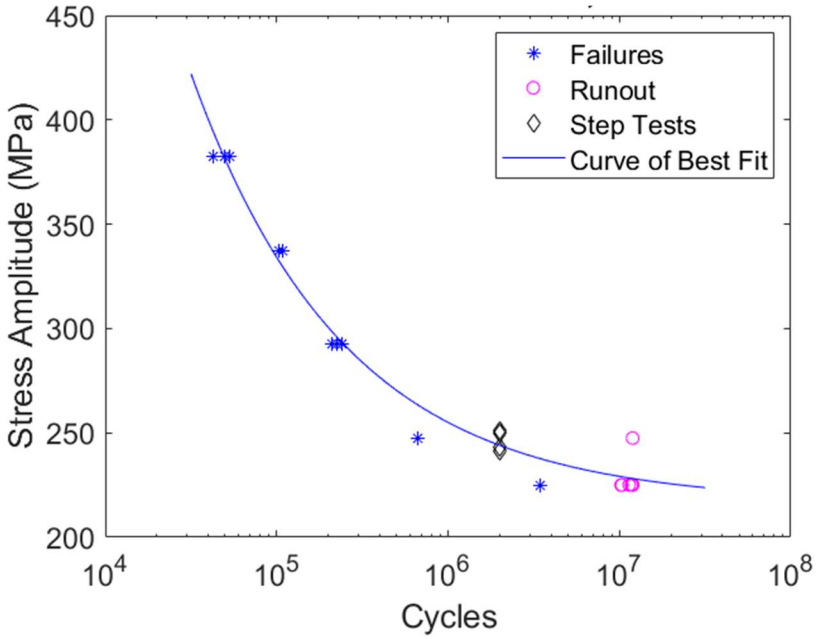

Figure 61. Double power law curve fit to SN data of Alloy 625 sheet tested at R = 0.1.

The HCF tests were designed such that both intrinsic fatigue response of the material as well as the effect of the surface roughness were explored. To this end, two specimens were tested with polished sides in the gage section to determine the intrinsic fatigue response, and the remaining specimens were tested in the as-built and post-processed condition which includes influence of the surface condition. Note that the support that was used on the bottom edge of the XY specimens introduced additional roughness to the surface. Therefore, the narrow side attached to the support of the XY specimen was polished for all samples since this would not be representative of a surface in a component at a location where HCF is a concern.

All fatigue experiments on the AM HCF specimens were carried out on uniaxial servohydraulic test systems with a sinusoidal force waveform and cyclic frequency of 20 Hz. The stress ratio (R) was fixed at 0.1. The test was terminated upon load drop below 100 N, which implies the failure (fracture) of the specimen. If no failure had occurred by 2×10^6 cycles for a step test segment or 10^7 cycles for the standard fatigue test, the test was stopped.

To set the initial stress amplitude for the first step of the first specimen of a build, it was assumed that the fatigue strength of the AM specimen and rolled sheet specimen possess a ratio similar to their corresponding hardness ratio. Thereafter, the testing was conducted at 80% of the average fatigue strength measured on other HCF specimens from the same build. The workflow of the adopted step test strategy is shown in Figure 62. If the failure occurs in the first step, it is assumed that the additively manufactured material follows the same S-N curve shape as that of the baseline rolled sheet (Figure 61). Therefore, the fatigue strength is determined using the double power-law expressed as

$$\sigma_E = \sigma_{FS} + A\left(N_r^a - N_f^a\right) + B\left(N_r^b - N_f^b\right) \quad (5)$$

where σ_{FS} is the stress amplitude applied in the first step, N_f is the number of cycles to failure in the first step, and N_r is the reference life which in this program is defined as $N_r = 2 \times 10^6$ cycles. The fatigue parameters are the same as the baseline rolled sheet, i.e., A = 31,420 MPa/cycles, B = 217 MPa, a = -0.485, b = 0.

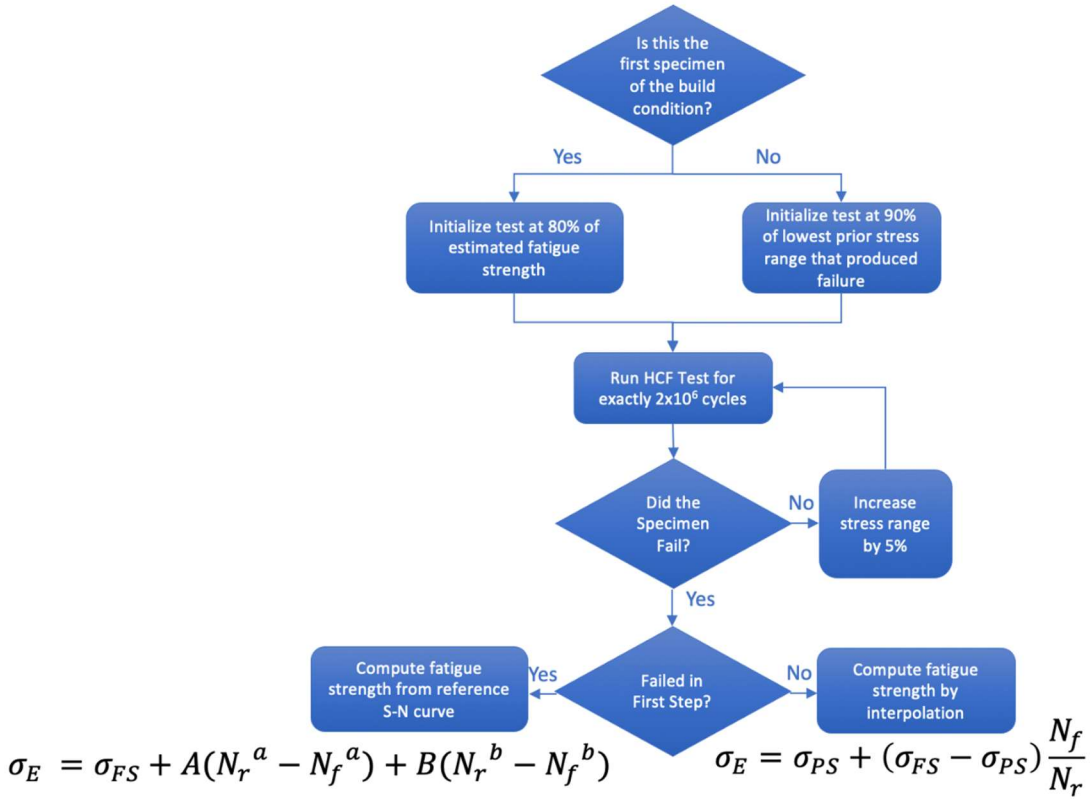

Figure 62. The step test workflow to determine the fatigue strength.

The fatigue strengths at 2×106 cycles for Z and XY specimens are summarized in Figure 63 and Figure 64 with specific values for each HCF test reported in Table 14. Figure 63 shows the results for the small Z specimens, comparing the fatigue strengths for the 11 builds tested in both as-is (as-built plus post process HIP) and polished conditions. The variation bars represent the range in fatigue strengths measured from multiple specimens. In nearly all builds, the polished specimens had higher fatigue strength, especially prevalent in the higher fatigue strength cases. There is a high variability in the strengths of the specimens across builds. It can be observed from the plots that builds 1-3 and 9-11 performed much better than the rest. In fact, builds 3 and 11 in the polished conditions had very similar fatigue strengths to the rolled IN625 sheet which is 244.6 MPa for R = 0.1. It is worth highlighting that the expected strength of the as-is small Z specimens for build 11 was higher than the obtained data. This is due to a large porosity defect found on the surface of one of the specimens. Therefore, the average strength is considerably penalized and increases the uncertainty of the builds from the Renishaw AM250. Overall, the step test method was successful at measuring fatigue lives, with the exception of specimens from build 7 which had very low performance due to extreme lack-of-fusion porosity.

Figure 64 compares the fatigue strengths of the small Z and XY specimens tested in the as-is condition. For the Concept M2 builds (1-6), a significant difference of fatigue strengths was found between the two orientations, especially for the cases with good fatigue strength properties in the Z-direction. This is consistent with the notion that cases where there is a larger amount of porosity, the difference becomes lower or almost negligible because the fatigue crack formation is completely governed by porosity defects

and not surface roughness features. An interesting insight from this plot is that there is a larger anisotropy in fatigue strengths between Z and XY specimens for the Renishaw AM250 than the Concept M2 machine, with the exception of build 11.

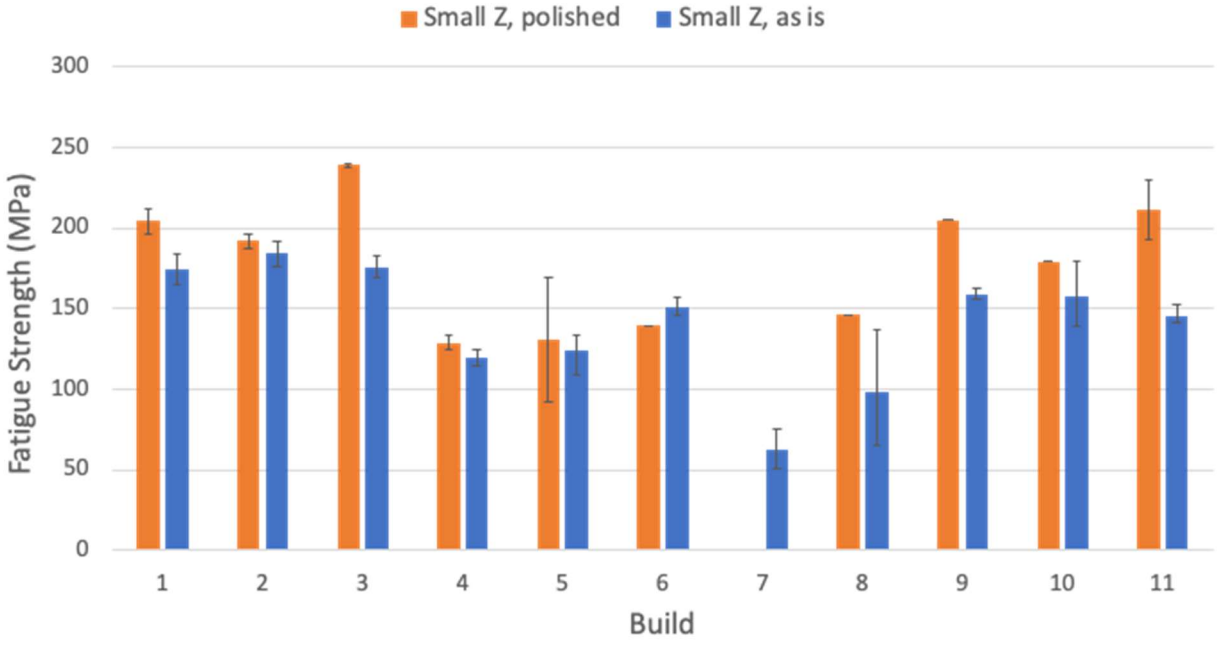

Figure 63. Fatigue strengths for 2 x 10^6 cycles measured on the small Z specimens in the as-is and polished condition (R=0.1).

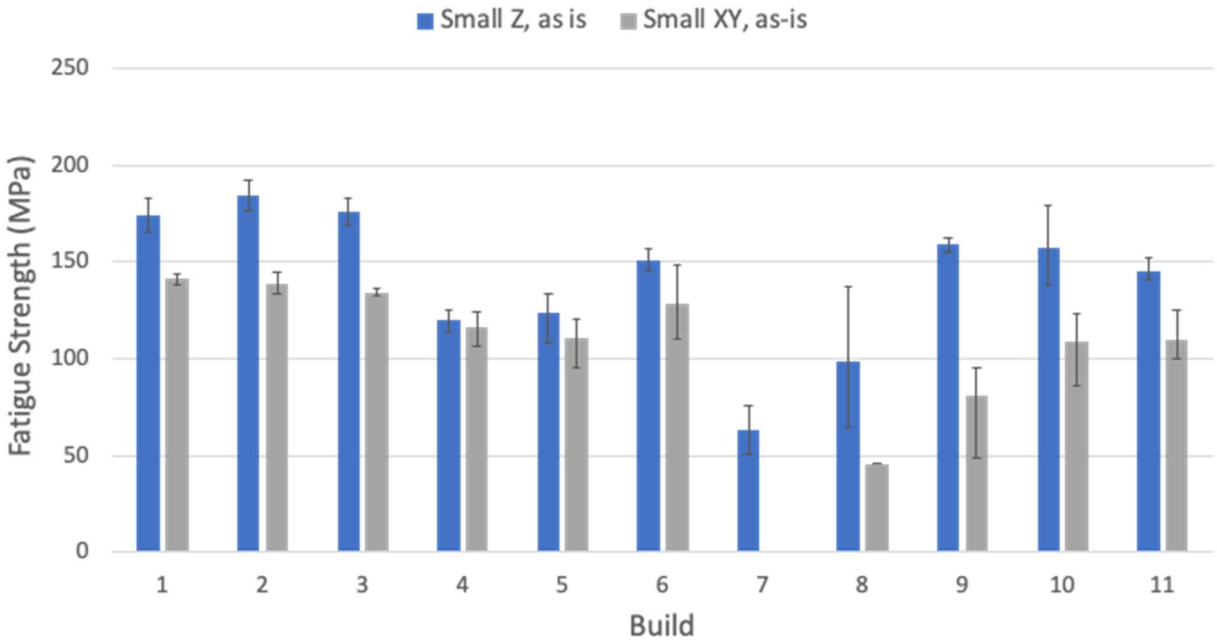

Figure 64. Fatigue strengths for 2 x 10^6 cycles measured on the small Z and XY specimens tested in the as-is condition (R=0.1).

Table 14. Fatigue strengths of each HCF specimen, reported as stress range in MPa

blank	as-processed
]	as-processed + polish filed edge
[]	as-processed + polish narrow edge
P	as-processed + polish all sides
FFS[1]	failed first step

Completed - good value
No action yet
Damaged/flawed specimen

Test conditions (unless otherwise
Frequency 20 Hz
R 0.1
Reported values are stress ranges w

	Spec ID	DOE Build 1		DOE Build 2		DOE Build 3		DOE Build 4		DOE Build 5		DOE Build 6	
Small Fatigue Z	7	367.0		392.3	P	338.2		228.7	FFS	217.0	FFS	278.5	P
	8	424.3	P	362.0		476.1	P	249.1		184.8	P FFS	301.4	
	9	392.8	P	378.9		479.1	P	231.5		337.6	P FFS	292.2	FFS
	10	330.7	FFS	384.4				249.7		246.7	FFS	300.3	
	11	350.8		375.1	P	350.1		249.1	P	266.7	FFS		
	12	347.7		352.5		365.8		265.9	P	262.2		314.0	
Small Fatigue X-Y	13	286.4	] FFS					233.2	]	241.7		221.3	FFS
	14	276.8	[]	263.4	P FFS			213.4	FFS	228.9		296.3	
	15							225.2	FFS			276.1	
	16	256.3	P FFS	274.5	FFS	266.1	FFS	248.0	FFS			257.8	FFS
	17	287.9	FFS	268.0	FFS			240.1	FFS	221.6	FFS	231.9	
	18	279.8	[]	289.7	]	272.1	] FFS			190.9	FFS	280.3	P
Large Fatigue Z	1	279.0	FFS			262.4	FFS						
	2							239.9	FFS				
	3					260.1	FFS	226.5	FFS				
	4							213.7	FFS				
	5							197.6	FFS				
	6					225.3	FFS	265.6		163.2	FFS		
Large Fatigue X-Y	19												
	20												
	21												
	22												
	23												
	24												

DOE Build 7		DOE Build 8		DOE Build 9		DOE Build 10		DOE Build 11	
Too Low*	FFS	292.2	P	325.5		359.3		458.4	P
Too Low*	P FFS	185.0	FFS			308.5		284.6	
		129.8	FFS			358.6	P	384.9	P
100.6				311.0		277.4	FFS	281.7	
151.0				409.2	P			304.7	
		274.7	FFS	Too Low*				327.8	
Too Low*	FFS	91.6	] FFS	187.2	FFS	172.9	FFS	210.5	FFS
				158.6	FFS	200.2	P FFS	250.2	FFS
				97.2	FFS				
						231.1	FFS	199.6	FFS
				191.7		222.4		219.7	FFS
				175.3	FFS	245.9	FFS	254.5	P
						174.8	FFS		
								255.6	FFS
						201.4	FFS		

G. ANALYSIS OF HCF DATA WITH A DAMAGE TOLERANT DESIGN POINT OF VIEW

Considering the level of porosity remaining in the HCF specimens even after HIP, a damage tolerant design point of view appears to be a sensible course of action to establish design allowables and a material model for each zone of the digital twin of the component. This was performed using NASGRO ver. 9.2. The material file available in NASGRO 9.2 for IN625 Sheet & Plate, room temperature, which had similar mechanical properties as our baseline IN625 sheet, was used in the analysis. The fatigue crack growth rate model selected was the NASGRO equation with default settings for the various options. The parameters of this material file are reported in Figure 65. Using these settings and material file, the ΔK_{th} was about 5.2 MPa $m^{1/2}$ for long cracks.

Stress-life curves were generated by repeatedly running NASGRO with different starting crack sizes, different starting crack locations, and stress amplitudes, shown in Figure 66. Three initial crack start locations were selected. These included two semi-circular edge cracks, one starting on the wide edge and one starting on the narrow edge, and a quarter-circular corner crack. On the wide edge, the SC30 geometry model was used in NASGRO, with the crack placed a quarter of the wide length from a narrow edge, illustrated in Figure 66. The flaw size was defined as the radius of the starting crack. Initial flaw sizes considered in the analyses ranged from 10 μm to 500 μm. Cracks were allowed to grow until either specimen fracture occurred due to the maximum stress intensity of the crack reaching the fracture toughness or net section yielding was reached in the remaining ligament. The fatigue limit was defined as the condition where the starting crack does not grow.

The predicted stress-life curves were similar for all three crack starting locations with the crack starting on the wide edge resulting in the lowest life. In the remaining figures, the stress-life curves with the crack starting from the wide side, being the most conservative, are compared to the life data obtained on the additive manufactured HCF specimens.

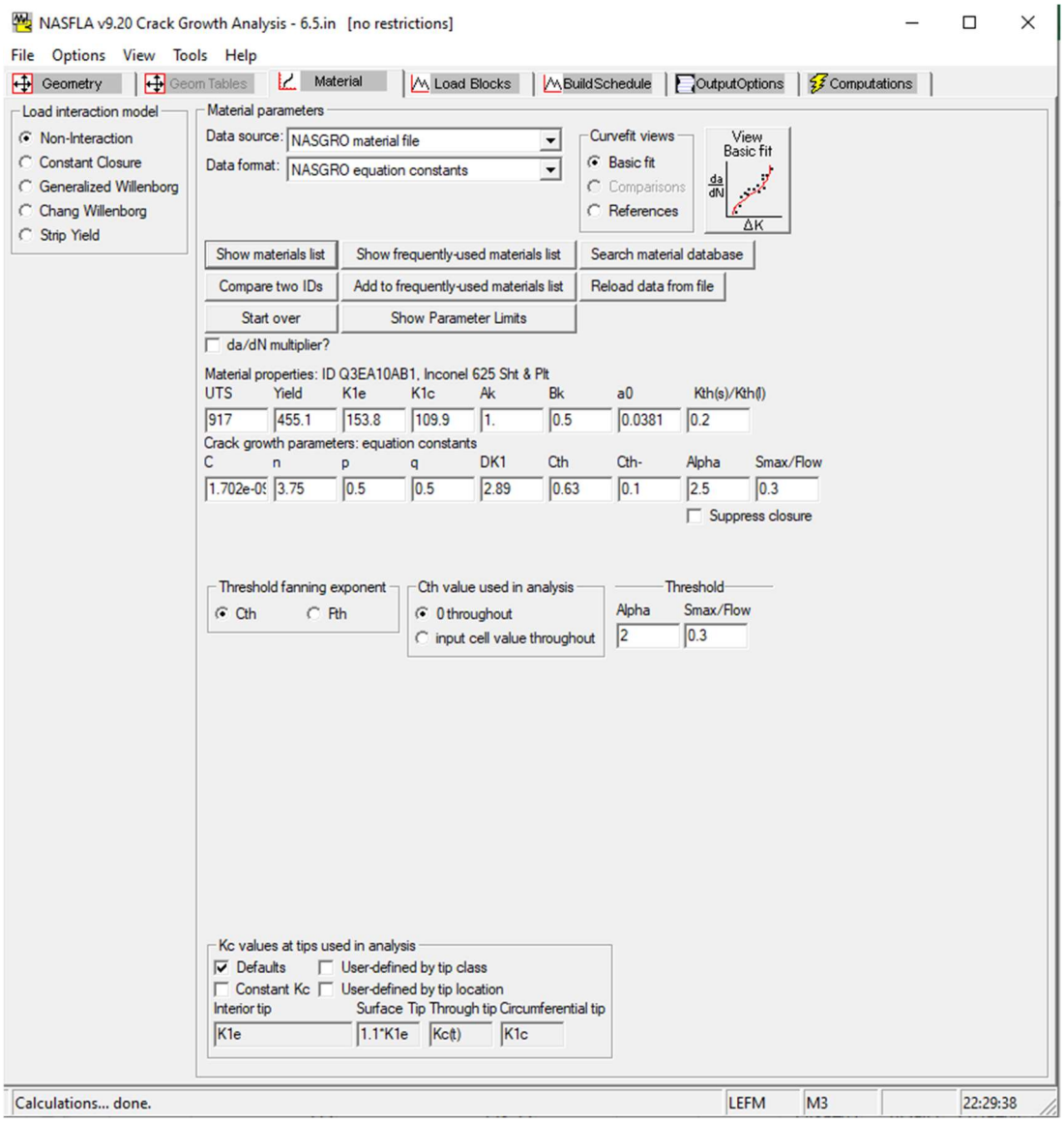

Figure 65. Material parameters used in the NASGRO fatigue crack growth rate equation representative of the rolled IN625 sheet.

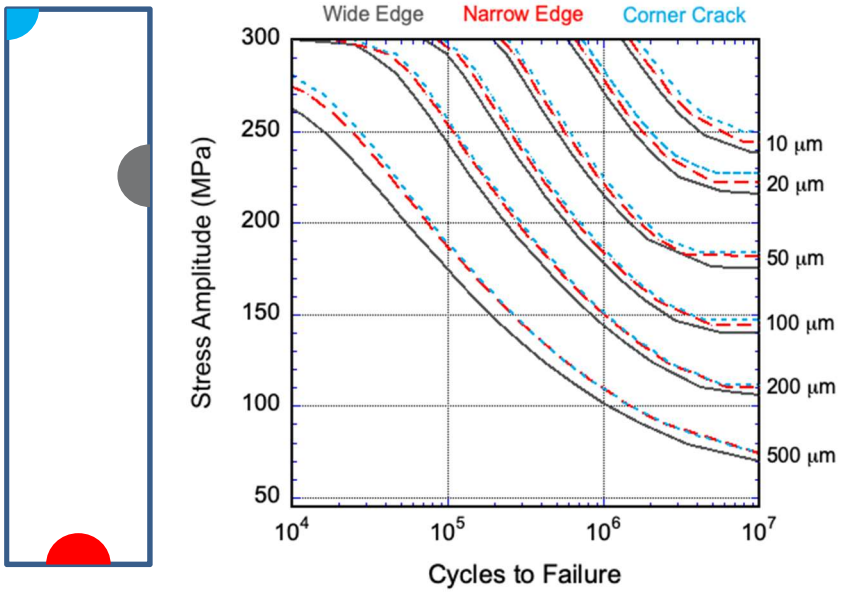

Figure 66. NASGRO predictions of S-N curves for three different initial flaw starting locations (R = 0.1).

The small specimen HCF lives for cycling in the Z direction are shown in Figure 67 and in the XY direction in Figure 68. Clearly, the lives of builds 7 and 8 are lower than the other builds, which can be directly attributed to the extreme porosity in those two builds even after HIP. Disregarding those two builds, the equivalent initial flaw size (EIFS) that captures the complete range of lives ranges from 50 to 500 μm. Polishing, or similarly machining, the surfaces of the Z direction specimens within the gage section indicates that the worse crack-like flaw is reduced, with the minimum EIFS being 20 μm for the best builds, indicating that surface roughness in the as-is condition has some influence on reducing the fatigue strength. One specimen from build 5 contained several lack of fusion type defects close to one another, shown in Figure 69, resulting in an EIFS close to 500 μm, consistent with the combined size of the lack-of-fusion defects observed.

In the XY orientation, the fatigue lives are lower than the Z orientation. In this condition, the EIFS is considerably larger ranging from about 120 μm to 500 μm, after removing the data of builds 7 and 8 which had extreme porosity. The majority of the fatigue cracks in the XY-oriented specimens formed on the narrow edge closest to the build plate. Even though the build supports on that edge were filed and polished, pockets along that edge were found to still contain lack of fusion type defects where the fatigue cracks formed (Figure 70). This appears to be the main reason why the XY-oriented specimens had lower average fatigue strength over all of the builds.

Since the porosity appears to be a primary source for fatigue crack formation, the fatigue lives were replotted on the NASGRO predictions with symbols indicating the average level of porosity observed in the microstructural samples for each build (see Figure 32 for reference). These are shown in Figure 71 using the mean porosity measured in the post-HIP microstructural samples. For good processing, the porosity is expected to be much less than 1%, which are represented by the black symbols on these plots. Clearly, the fatigue strengths are considerably higher for these builds with minimal porosity compared to the others. For the Z-oriented specimens in the polished condition, the EIFS is around 50 μm, which is comparable to the worse case porosity measured in the specimens. These plots also suggest that when the surface is left in the as-is condition (i.e., without any machining of the surfaces) and it is known that the surface is at a location where the cyclic stresses are high and cracks may form there, the EIFS needs to be set higher. The current data suggests setting the EIFS to 200 μm even when porosity is less than 1%. The EIFS for the XY-oriented specimens is higher, between 200 and 500 μm for the builds with porosity less than 1%. Most of these

cracks formed on the narrow edge closest to the build plate where lack of fusion defects of this general size were frequently observed (Figure 70).

Alternatively, and potentially having utility in the process qualification, these NASGRO predictions can be used along with witness specimens that are characterized immediately after the build is complete to verify that the build is good before performing the subsequent processing steps. This would help save the time and cost of processing parts that would be rejected later in the process. In each build, one of the microstructural samples was not further processed except for the stress relief which was performed before removing the samples from the build plate. These samples were labeled BN-35, where BN is the build number. The porosity in these non-HIP samples was higher and easily measurable by various standard methods (e.g, micro Xray CT, Archimedes' method for measuring density, optical microscopy of polished sections, etc.). Setting the threshold to 3% porosity, which is still somewhat high for as-built specimens using L-PBF process, but the best among the builds in this program, the fatigue strengths of all of the completely processed specimens (i.e., received HIP) in this grouping are near the higher end. It suggests from a damage tolerant point of view, that a witness specimen where just porosity is measured and found to be acceptable, here <3%, an EIFS of 50 μm for Z-oriented specimens in the HIP condition results in a stress-life curve that describes the mean stress-life curve. In the cases where the fatigue crack is expected to form at a build support location, the EIFS needs to be higher to capture the stress-life curve. In this study, an EIFS of 200 μm captures the mean stress-life behavior. Certainly, good build plate design needs to avoid locating build supports, or in general, the downward side of overhanging surfaces, in locations where the cyclic stresses are highest.

The Kitagawa-Takahashi (K-T) diagrams produced using the fatigue strengths at 1 x 10^7 cycles predicted by the NASGRO analyses are shown Figure 73. The K-T diagram is plotted in two ways, one using the EIFS defined by the radius of the flaw using the geometries shown in the schematic of Figure 66 and the other using the Murakami sqrt(area) parameter where the area is either the effective area of the largest defect or the area encompassing several defects close together. The fatigue limit obtained from the IN625 sheet, which is also consistent with the fatigue limit reported for IN625, R = 0.1, sheet and plate, in MMPDS-15 (Metallic Materials Properties Development and Standardization handbook), is used on these K-T diagrams. Based on these K-T diagrams, the critical flaw size, above which fatigue strength is reduced, is about 20 μm. This value is consistent with the EIFS for the polished Z specimens that exhibited the highest fatigue strength (Figure 67).

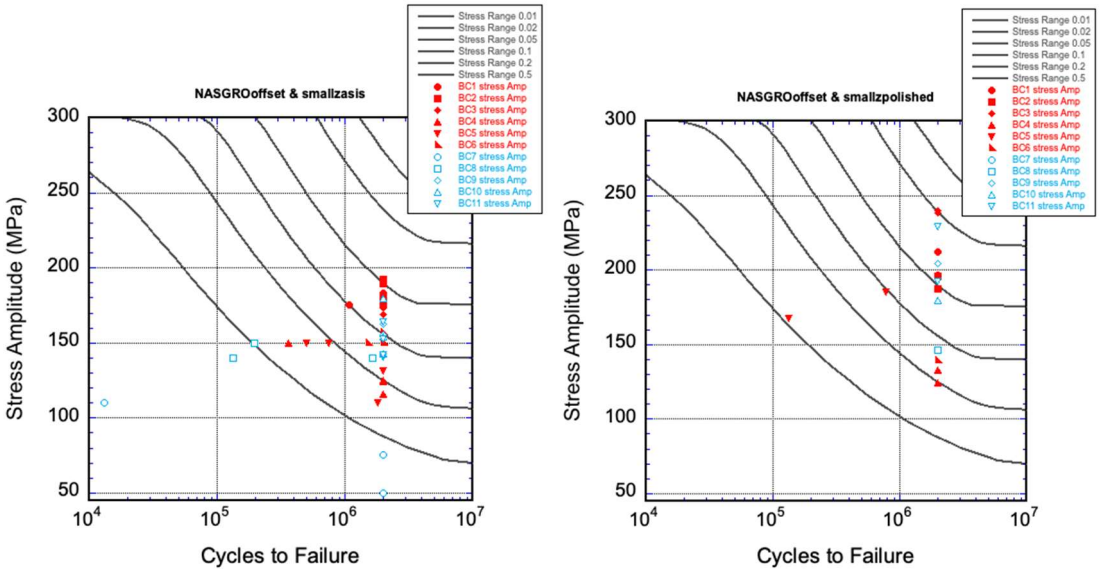

Figure 67. NASGRO predictions of S-N curves for different initial flaw sizes for small Z specimens tested in the as-is (left) and polished (right) conditions (R = 0.1).

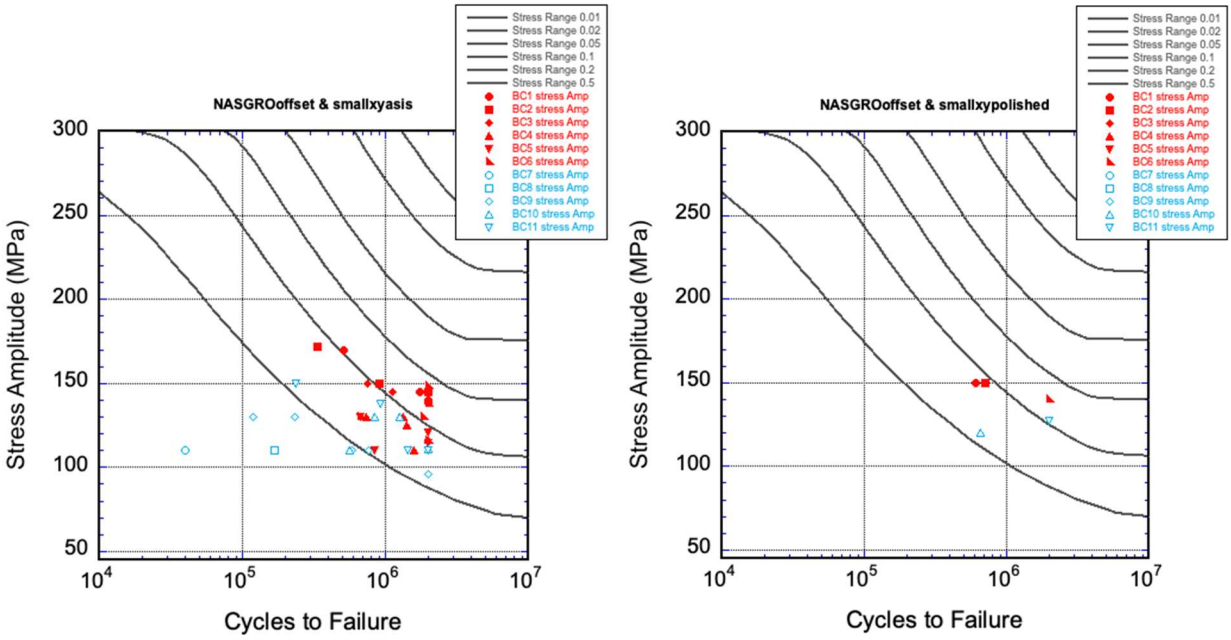

Figure 68. NASGRO predictions of S-N curves for different initial flaw sizes for small XY specimens tested in the as-is (left) and polished (right) conditions (R = 0.1).

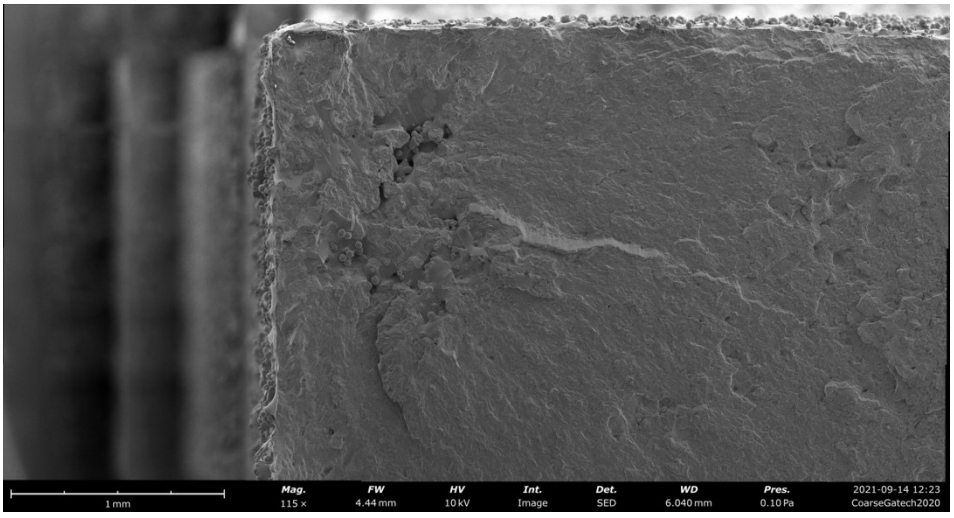

Figure 69. SEM image of HCF Z-oriented specimen from Build 5, Specimen 8, showing region where fatigue crack formed.

Figure 70. SEM image of HCF XY-oriented specimen (Build 1, Spec 18) showing typical defect observed on the narrow edge closest to the build plate.

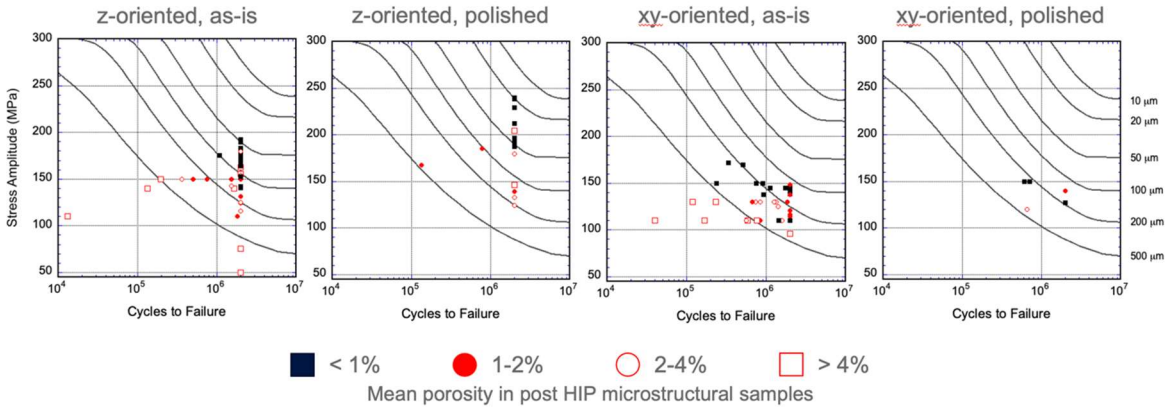

Figure 71. NASGRO predictions of S-N curves for different initial flaw sizes compared to HCF data comparing the influence of mean porosity of the HIP'ed microstructural samples (R = 0.1).

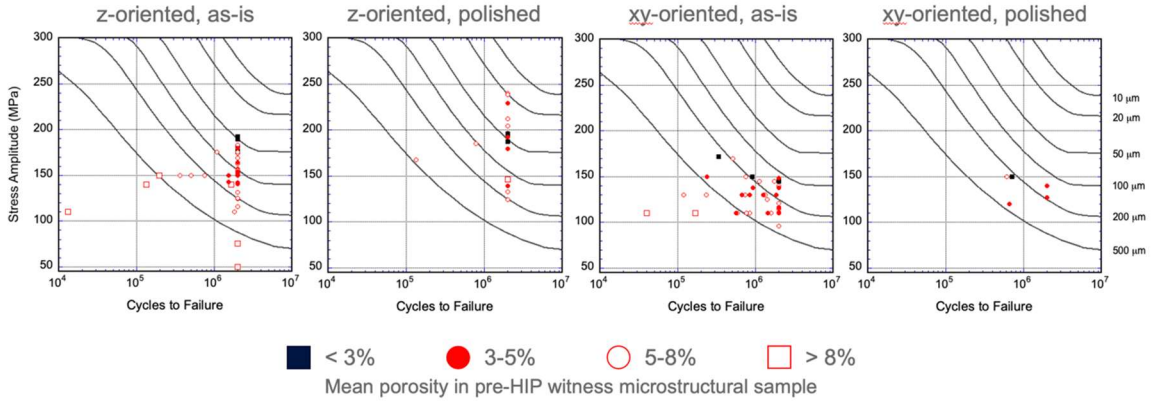

Figure 72. NASGRO predictions of S-N curves for different initial flaw sizes compared to HCF data comparing the influence of mean porosity of the witness microstructural sample (R = 0.1).

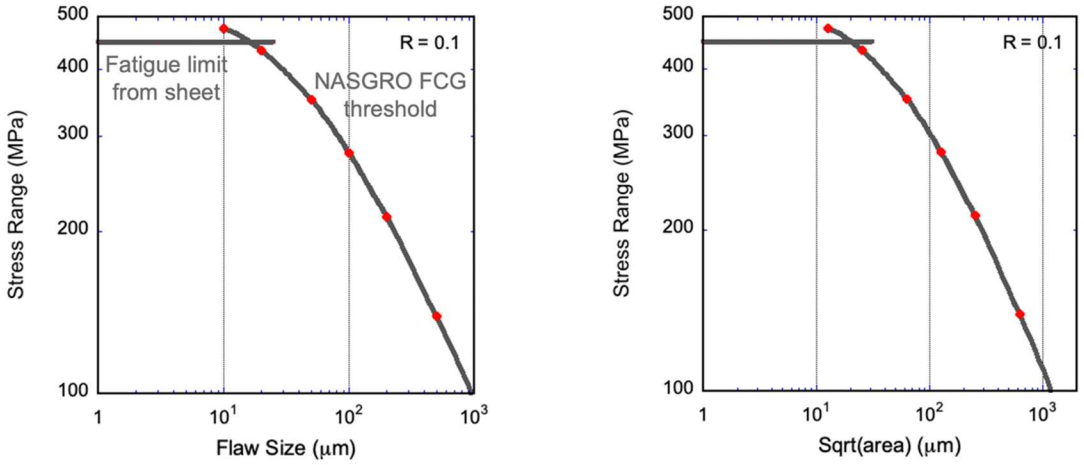

Figure 73. Kitagawa-Takahashi diagrams for fatigue strengths at 1 x 10^7 cycles determined by NASGRO analysis and fatigue limit of rolled sheet (R = 0.1).

H. ML MODEL DEVELOPMENT TECHNIQUES

In general, the end goal is to form a function through a learning process by an ML algorithm that maps outputs to the inputs. These regression methodologies used in ML determine and characterize the cause-and-effect relationships between several dependent (target) and independent (predictor) variables. Once such a relationship is estimated, it becomes a key tool in efforts aimed at predictive modeling, significance and impact analysis, and design.

The regression algorithms can be broadly categorized into two classes: (i) parametric and (ii) nonparametric regression techniques. Examples of parametric regression models are linear, nonlinear, and generalized linear models. The primary characteristic that these parametric regression models have in common is that the form of the function that describes the relationship between independent and dependent variables is predefined, and the model parameters are determined through the learning process of the algorithm.

Contrary to the parametric models, in nonparametric techniques, no assumption is made on the functional form of the relationship, and it does not require prior knowledge of the trend of the data. The function is data-dependent, and it allows information to be passed from the data set while establishing the form of a functional model. Data smoothing techniques, kernel-based models (e.g., support vector machines and Gaussian processes), k-nearest neighbor, and regression trees are examples of nonparametric algorithms. Given the definitions for each approach, it is readily perceived that parametric methods are associated with restrictions due to the prescribed form that is imposed prior to the learning process. In contrast, the flexibility that accompanies nonparametric techniques enables them to adjust the learning function to bring about superior precision. Nonparametric methods are best suited if the empirical relationship is nonlinear and unknown, but they require a larger sample size to derive the model structure compared to the parametric techniques.

Both parametric and non-parametric regression techniques were used to construct DTMMs to illustrate the suitability of the different ML methods using the same database. The methods exercised in developing the DTMM included

- Parametric Linear Multiple Regression (MR)
- Support Vector Regression (SVR)
- Gaussian Process Regression (GPR)
- Multiple Tensor-on-Tensor Regression (MTOTR)

Parametric Linear Multiple Regression (MR) models are the most widely used and accepted parametric techniques owing to their simplicity of implementation and interpretation. A linear equation is fitted to a pattern of data, and for *n* number of variables and *p* number of observations.

Support Vector Regression (SVR) is a nonparametric ML approach that is an extension of support vector machines (SVM) to the regression problems where the model returns a continuous output as opposed to a discrete set-in classification cases. The hyperplane that separates the distinct classes in SVM becomes the function to approximate the dependent variable in SVR. In other words, SVR, analogous to all other regression problems, attempts to find the best function that maps data from input to output domain. It entails solving a convex optimization problem to determine a hyperplane accompanied by an ε-insensitive region, called ε-tube that estimated the output data. Essentially, the ε-tube designates a tolerance zone (i.e., acceptable error) and the best hyperplane is the one that encompasses the largest number of support vectors (the data points closest to the hyperplane) inside its corresponding tube. The support vector (SV) framework has shown popularity in additive manufacturing applications for both classification and regression models to provide design decision support, AM process and performance optimization, in-situ process monitoring and control, and post-process inspection and validation. In some applications, SV-based regression techniques are promising alternatives to artificial neural networks.

Gaussian Process Regression (GPR) is a flexible, nonparametric, and probabilistic ML approach relying on the Bayesian inference framework. It is associated with attractive characteristics that has turned it into a prevalent surrogate modeling technique. In recent scientific efforts, researchers have devoted their attention to utilizing GPR for the development of the regression PSP models. It circumvents the need for large size database and offers the capability for quantifying the uncertainties associated with the predictions. The broad definition for the uncertainty quantification (UQ) is the science of diagnosis, characterizing, quantifying, and controlling uncertainties that are inevitably introduced in stochastic physical systems and models. It has received considerable attention for modeling of complex systems in critical applications. Before delving into the details of GPR, the Bayesian approach is introduced briefly, which is a counterpart to the traditional frequentist philosophy. In the traditional statistical viewpoint, the estimates of the unknown variables are considered as deterministic quantities, while the Bayesian scheme is based on probability, and all variables are random that follow a joint probability distribution with confidence intervals that reflect the high probability density regions. The other significant distinction is that Bayesian approach enables the inclusion of prior domain knowledge in the available observation which is an imperative capability in engineering settings. Therefore, Bayesian inference entails estimating the posterior distribution by combining the prior distribution and the observations based on the Bayes' theorem.

Multiple Tensor-on-Tensor Regression (MTOTR) is the most novel technique investigated. This is the first time that it has been used to learn AM data. It features consolidation of the independent dimensionality reduction and modeling task of the other methods into one single step. This distinct advantage potentially mitigates the loss of information encountered in the conventional PCA-regression approach.

The details including equations and references for these ML methods are documented in the PhD Dissertation of Sanam Gorgannejad [Gorgannejad, 2020].

I. INITIAL PROCESS-STRUCTURE MODEL

The primary objective of the process-structure (PS) model is to predict the resultant porosity and surface roughness from the AM processing variables. The data presented in Table 15 have been used as an input to build the PS model. The model input include two continuous variables, scan speed and hatch spacing, and two categorical variables, AM system and the direction of the printed specimens. Since the "SR" and "NSR" post-processing heat-treatments do not influence the structural attributes under study (porosity and surface roughness), they are not used as the model input variables. The output data is comprised of the PC scores characterizing the combined state of the surface roughness and the porosity of the built state.

Table 15. The input data for the construction of the process-structure model. The 0 and 1 values for direction and machine variables denote XY and Z, respectively, and Concept M2 and Renishaw AM250 systems, respectively.

Obs	Sample ID	Obs ID	Scan Speed (mm/s)	Hatch Spacing (μm)	Direction	Machine
1	1-13,14	b1dxy	800	70	0	0
2	10-7	b10dz	900	70	1	1
3	10-13,16,18	b10dxy	900	70	0	1
4	11-8,10,12	b11dz	800	70	1	1
5	11-13,14,16	b11dxy	800	70	0	1
6	2-16,17,18	b2dxy	900	100	0	0
7	3-16	b3dxy	900	70	0	0
8	4-13,15,16	b4dxy	800	100	0	0
9	5-10,11,12	b5dz	850	85	1	0
10	5-17	b5dxy	850	85	0	0
11	6-8,9	b6dz	900	100	1	0
12	6-13,15,16	b6dxy	900	100	0	0
13	7-7	b7dz	900	100	1	1
14	8-8	b8dz	800	100	1	1
15	8-13	b8dxy	800	100	0	1
16	9-7,10	b9dz	850	85	1	1
17	9-13,14,15	b9dxy	850	85	0	1

Various machine learning approaches were implemented and their power in learning from small datasets was evaluated. Two general approaches were adopted for the development of the PS model: (1) PCA-regression and (2) MTOTR.

For the first approach, two regression algorithms were implemented, MR and SVR, to investigate whether the flexibility offered by not imposing a predetermined form of the equation to the data would enhance model performance. However, the cross-validation results reflecting the generalization power of the models were comparable. Indeed, the ease of implementation that does not involve form and term selection is a benefit of SVR that should not be neglected.

In the second approach, the novel MTOTR method combines the dimension reduction and regression in a single algorithm. Therefore, the 4^{th}-order tensor built from the stack of the 2-point spatial correlation images was used to train the model instead of the reduced structure representation by PC scores. The MTOTR algorithm learns basis vectors of the output images such that they hold high correlation with a response while in the PCA-regression approach, performing the dimensionality reduction and regression in sequence suggests that no correlation is necessarily guaranteed between the first few determined PC scores and the processing parameters. As a consequence, the outperformance of the MTOTR method was evident by the cross-validation process as shown in Figure 74. The reconstructed images from PCA-regression prediction of PC scores and the predicted images from the MTOTR model were compared to validate the results as shown in Figure 75. Therefore, the MTOTR model established a tool for direct prediction of the quantified 2-point correlation images with high accuracy, the capability that is often offered by deep learning methods such as convolutional neural network models which have the disadvantage of demanding extremely large datasets for training, and hence not feasible to use for the dataset in this work. Obviously, the hurdle of generating such a large amount of experimental data is the major impediment in developing models for

fatigue and hence we are limited to ML techniques that have success when data is sparse. It is noteworthy to point out that in addition to the outlined benefits of providing improved predictions, MTOTR is a computationally more expensive method than the first two techniques.

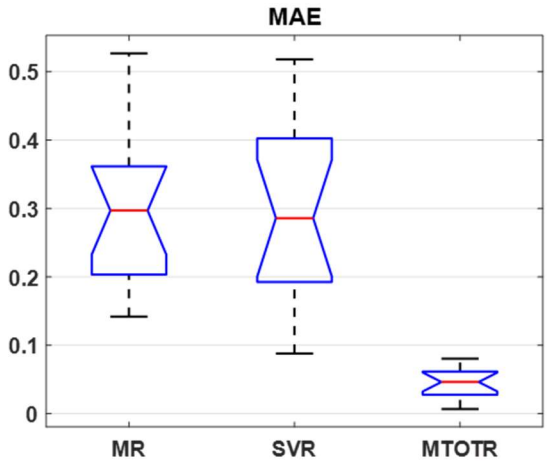

Figure 74. Mean absolute error boxplot of the fifteen leave-one-out predictions made by the MR, SVR, and MTOTR models.

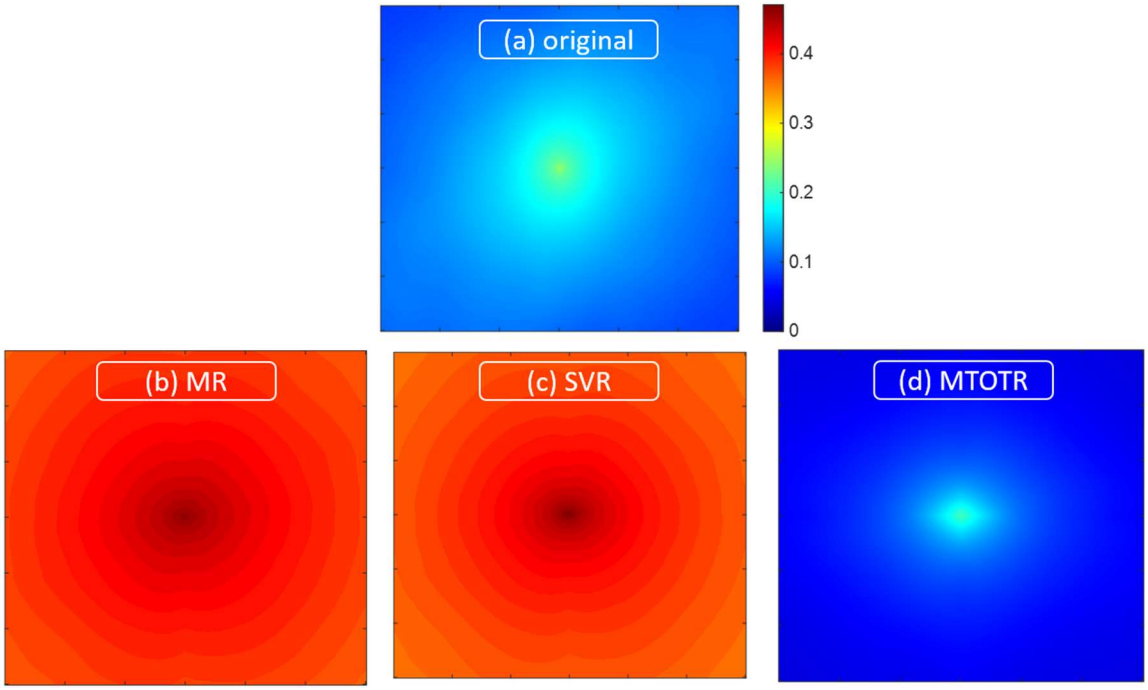

Figure 75. Illustration of an (a) original 2-point correlation representation of a sample surface roughness and the estimation of the same image using the models developed by the (b) MR, (c) SVR, and (d) MTOTR algorithms. Color scale bar is the same for all images.

J. INITIAL STRUCTURE-PROPERTY MODEL

To establish the structure-property (SP) model, the surface roughness and porosity were identified as the potent drivers that govern the HCF strength. The structure was characterized by the first three PC scores which were used as the input of the model and output is the scalar value of HCF strength. The data from Z

and XY specimens were combined together with the assumption that the existence of any structural direction-dependency that is critical to the property is captured through structure attributes.

Only PCA-regression methods were investigated since the output is a single scalar quantify (i.e., HCF strength). Note that the MTOTR algorithm was not used since it is more useful when the model's output is high-dimensional such as in the form of an image or video. In the property database, a few specimens exhibited considerably low strength which was attributed to the exceedingly rough surface or large lack-of-fusion pores. The MR model failed to make a good prediction of these points. Regularizing the regression model using ridge regression formulation was found to make significant improvements in these prediction errors. In addition to exercising SVR, GPR was adopted due to its unique capability to provide prediction uncertainty, which is crucial in predicting properties.

A comparison between the performance and generalization capability of the four data-driven structure-property models are summarized in Figure 76. The predictions of the SVR and GPR models were comparable and showed that they successfully captured the nonlinearities in the relations between structure and HCF strength. From the MR to regularized MR, SVR, and GPR, the model accuracy increased, and the nonparametric SVR and GPR models considerably outperformed the other two. The evident outperformance of the nonparametric kernel-based algorithms (i.e., SVR and GPR) demonstrates their power in learning the relationship between the potent structural attributes (surface roughness and porosity) of the additively manufactured Inconel 625 and the desired mechanical property (HCF strength). The key merit of SVR and GPR models is that they do not bound the data to a predetermined form of the equation, therefore unlike parametric regression method, there is no need to determine the best form prior to model training. Offering such advantage is particularly beneficial under the circumstance that the model requires regular re-training with collection of new data. It is concluded that various ML techniques possess unique benefits and drawbacks, and often, there is a trade-off between efficiency and accuracy.

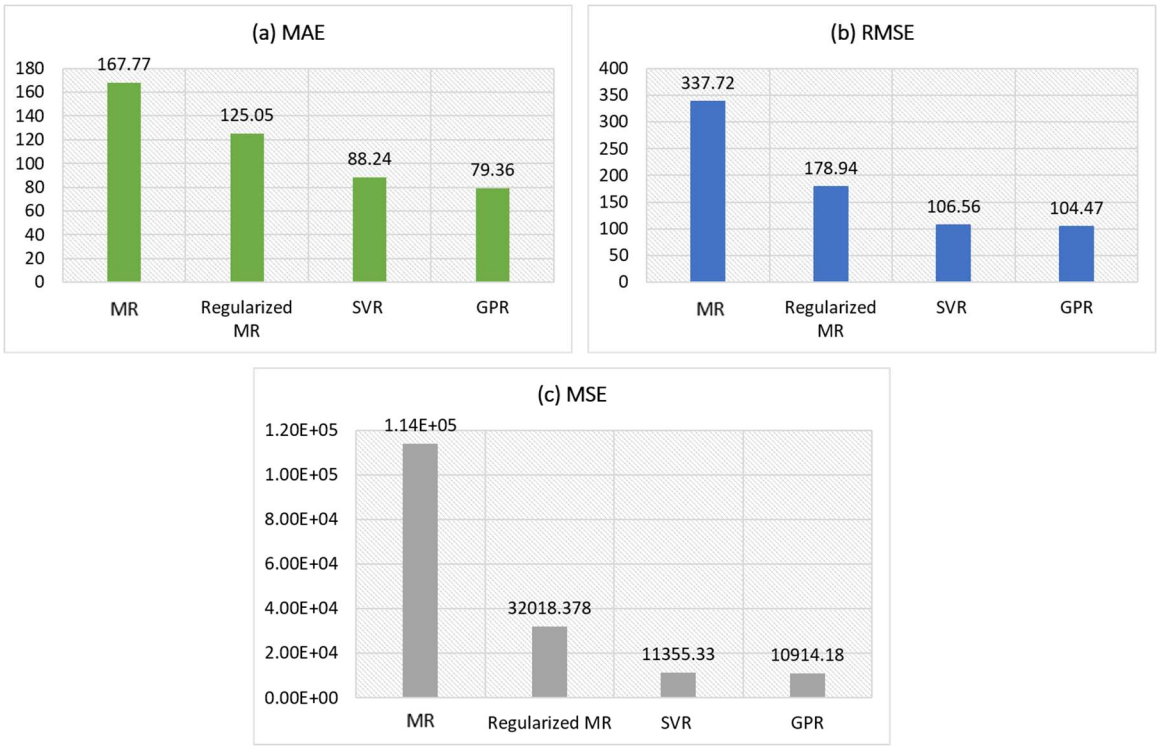

Figure 76. Cross-validation prediction errors of the structure-property models developed by four different machine learning algorithms: (a) Mean absolute error (MAE), (b) root mean squared error (RMSE), and (c) mean squared error (MSE).

K. IMPLEMENTATION IN CODE

Various research codes have been used to implement these different ML models. The more advanced models (SVR, GPR, MTOTR) require a combination of Matlab and Python scripts to run. Python is the preferred tool in the ML industry and all the ML codes except the MR are in Python. Matlab was used for image processing due to its ease of use and availability when the model was being developed. The 2-point spatial correlation is currently an open-source code only available in Matlab. Ultimately, these can be combined in a single code in future developments. These are discussed in detail in the PhD Dissertation of Sanam Gorgannejad [Gorgannejad, 2020].

The predictions using the different ML models tended to give similar trends. Since the Parametric MR model runs on a Matlab based code without the need for Python, it is provided as the DTMM since it could easily be run by any user at this time. It contains a Process-Structure model (PS.m) and a Structure-Property model (SP.m). The full PSP model with prediction of life (PSP_Nf.m) uses these two models to link the process parameters to HCF strength. If the loading parameters are also input, the number of cycles to failure is output. The output of the code is

1. Fatigue strength (in terms of stress amplitude) at 2×10^6 cycles for R = 0.1 for the process parameters that are input.
2. The cycles to failure (i.e., crack of an engineering size has initiated) if the stress amplitude and stress ratio are input. The Walker equation with $\gamma = 0.42$, taken from MMPDS-14 for Inconel 625, is used to account for the mean stress difference between the acquired HCF strength data and the loading on the component in each zone.

A screenshot of the Matlab code is shown in Figure 77. It highlights what the user inputs in the Editor window and the corresponding output in the Command Window. The two outputs are shown: High Cycle Fatigue Strength (HCFS) for 2 x 10^6 cycles in terms of stress amplitude and units MPa, and the number of cycles to failure (Nf) for the loading input.

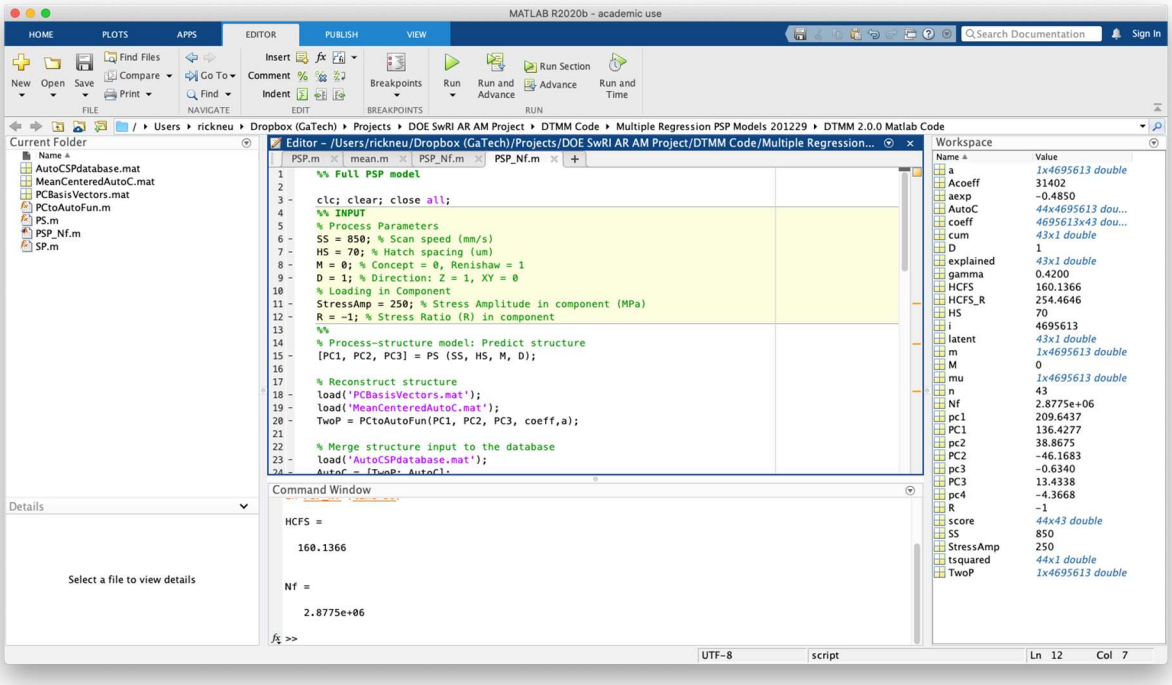

Figure 77. Screenshot of the Matlab code for running the Parametric Multiple Regression (MR) DTMM showing an example of the user input and resulting output.

Some examples of the SN curves generated from the output of the code are shown in Figure 78-Figure 80. The effect of hatch spacing on the cycles to failure is shown in Figure 78. Smaller hatch spacing results in better fatigue strengths and the Concept M2 had greater fatigue strengths than the Renishaw by 30 to 40 MPa in terms of greater stress amplitude. This is consistent with the observation that the majority of fatigue cracks formed at lack-of-fusion defects, which are generally more frequent as the hatch spacing is increased when that is the dominant defect type. The effect of scan speed is shown in Figure 79. Generally, the influence of the scan speed over the rather narrow range of scan speeds considered (800 mm/s to 900 mm/s) did not have as significant effect as the hatch spacing. The higher scan speed within this range is associated with higher fatigue strength.

The predicted stress-life curves for the specific process conditions of the 11 builds is shown in Figure 74. The model predicts that build 3 parameters (Concept M2, hatch spacing of 70 µm, scan speed of 900 mm/s) should result in the best fatigue strength. This figure also shows that the fatigue strengths of the Renishaw manufactured specimens are generally lower than the Concept M2 for the range of process parameters investigated. A contour plot comparing the influence of hatch spacing and scan speed is shown in Figure 81. The build 3 parameters (lower hatch spacing and higher scan speed) are highlighted as the optimum based on the data generated. The model predicts a primary dependence on hatch spacing and a secondary dependence on scanning speed. The model predicts no dependence on post-build annealing. The universally applied HIP wipes out any differences from the annealing step.

In a commercial implementation of this research code, it is envisioned that the algorithm demonstrated in this code could be implemented within each zone of a component to assess the current damage state from the process and loading pedigrees. It is primarily targeting the assessment of crack formation and its early crack growth in the presence of structure heterogeneity. It targets crack initiation to a sufficient engineering crack size after which damage tolerance approaches can then be applied to account for the subsequent fatigue crack growth to assess the full life of a component.

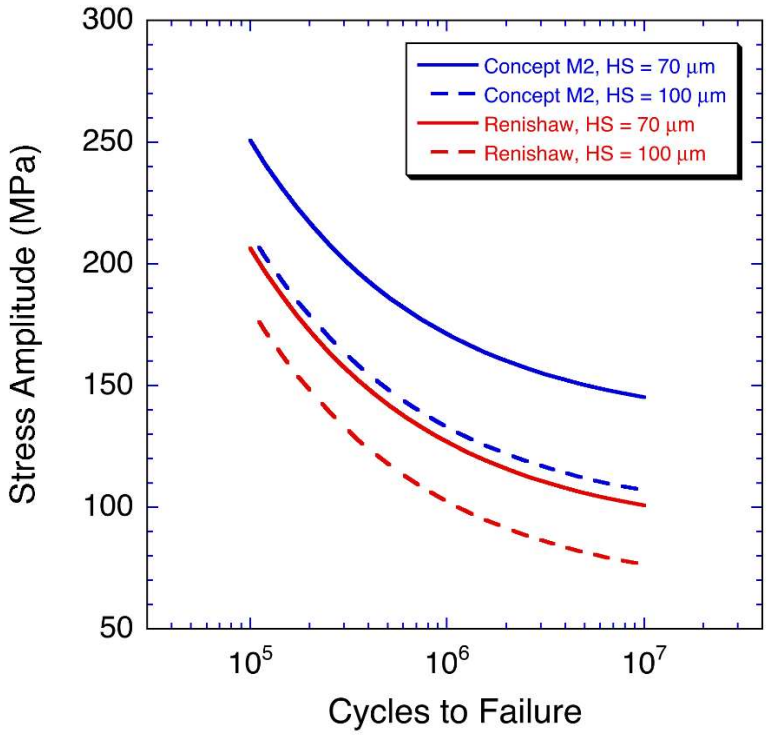

Figure 78. Stress-life plot for R = 0.1 showing the effect of hatch spacing with fixed scan speed of 850 mm/s generated from the Parametric Multiple Regression (MR) model, Z specimens in as-is condition (DTMM ver. 2.0.0).

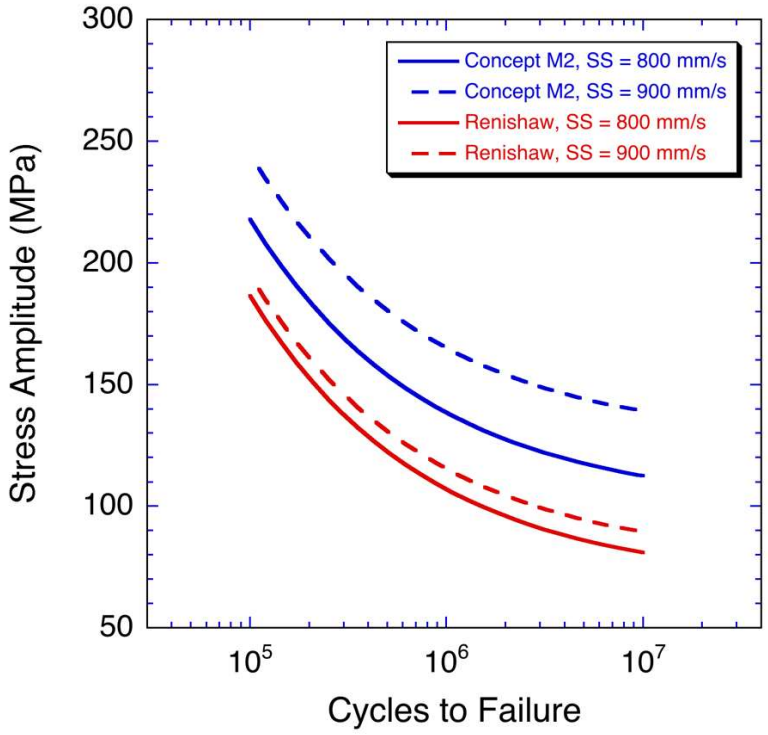

Figure 79. Stress-life plot for R = 0.1 showing the effect of scan speed with fixed hatch spacing of 85 µm generated from the Parametric Multiple Regression (MR) model, Z specimens in as-is condition (DTMM ver. 2.0.0).

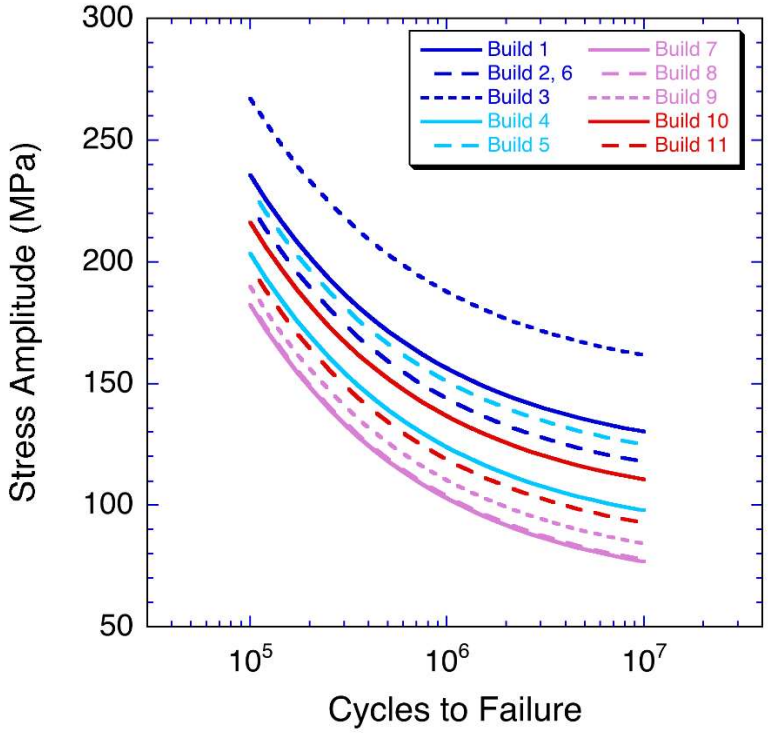

Figure 80. Stress-life plot for R = 0.1 comparing all build conditions generated from the Parametric Multiple Regression (MR) model, Z specimens in as-is condition (DTMM ver. 2.0.0).

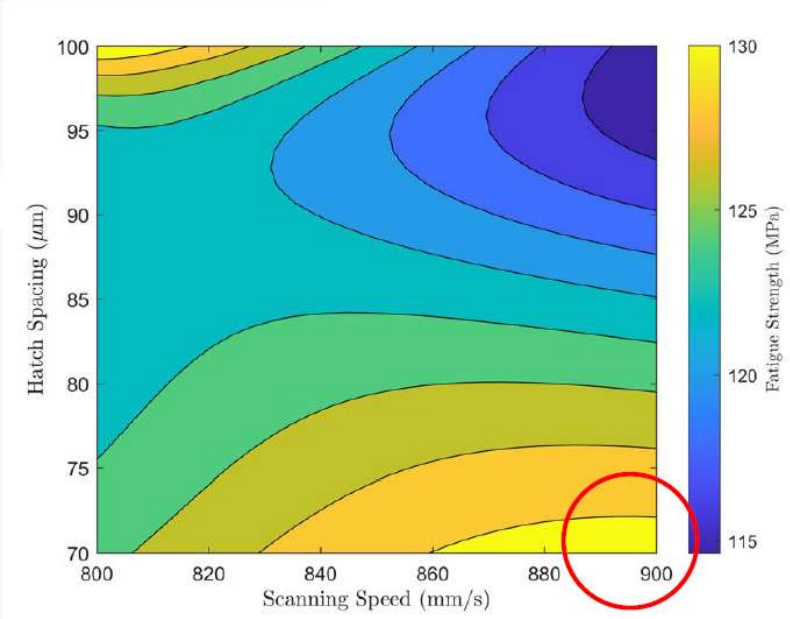

Figure 81. Contour Map Showing How Two Processing Parameters, Hatch Spacing and Scanning Speed, Influence Fatigue Strength in the XY Orientation (in Terms of Stress Amplitude for R = 0.1 Loading).

L. UPDATE OF THE DTMM WITH ADDITIONAL HCF DATA

The accuracy of data-driven models based on ML algorithms improves with additional data. This concept was explored by recalibrating the DTMM with additional data generated in the last year of the project (the original DTMM shown in the previous section was calibrated at the end of calendar year 2020 on a smaller dataset). At the time of the final training of the DTMM, the training data contained 58 surface roughness specimens, each with scans of the two wide surfaces, and HCF data from 95 completed tests. In this round, the narrow edge surface scans were left out from the training data to increase the computational efficiency.

The final training of the DTMM followed the same procedure as described above. All surface scan data, this time only including the two wide sides from each sample, were trimmed, segmented, and binarized into the black-blue (valleys), yellow-blue (median), and red-blue (peaks). The binarized images were then fed into the 2-point correlation algorithm to create correlation maps for each specimen. The data generated from the 2-point correlation maps of the surface roughness were merged with the maps created from porosity data. The multiple 2-point correlational maps of porosity for each build were averaged, excluding non-HIP samples. These build average values were concatenated to each of the 58 samples with roughness data. The combined roughness-porosity data was used as the input for PCA to reduce the dimensionality of the data and prepare it for model training. The PCA space plots and associated cumulative variance plot are shown in Figure 82. By using three principal components (PC's) it is possible to capture more than 99.9% of the variance of the input data.

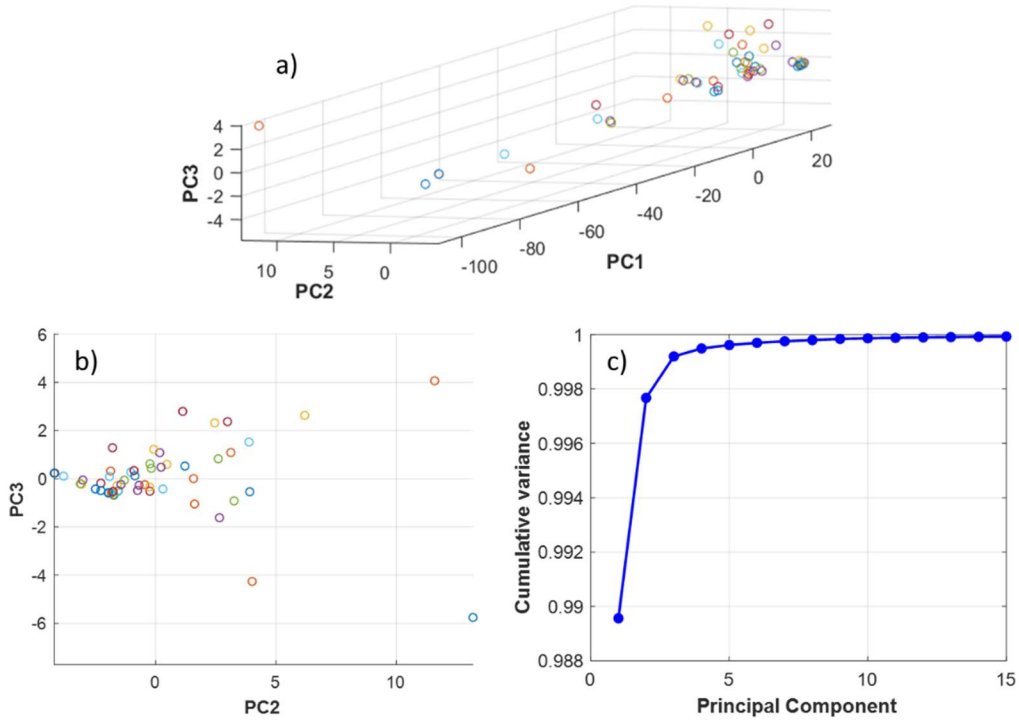

Figure 82. Low-Dimensional Representation of the Roughness-Porosity Data in (a) 3D and (b) 2D PC Space. (c) Plot Showing how Principal Components Cumulatively Contribute to Representing the Variance of the Original Data Set

The PC scores obtained from the PCA were used in the training data for the process-structure (PS) model and the structure-property (SP) model. In the updated DTMM, the training data has 58 samples, a few from each of the 11 builds. Each sample has associated surface roughness scan data and build-average porosity data which was transformed into PC scores. Each sample had three associated PC scores because, as the cumulative variance plot displays, three PC's are sufficient to capture most of the variance. By capturing most of the variance of the original data set, the PC scores accurately describe the surface condition and porosity state of each sample in low-dimensional terminology. The PC scores for each sample are associated with two continuous variables: hatch spacing (HS) and scanning speed (SS), and three categorical variables: machine (Concept M2 vs. Renishaw), build orientation (Z vs XY), and polish (as-built vs. polished). The PS training data was used in three of the regression methods previously described: parametric linear multiple regression (MR), support vector regression (SVR), and gaussian process regression (GPR). Using the training data, each method was capable of interpolating the PC scores for any combination of input variables. For example, given the input: hatch spacing = 70 micron, scanning speed = 800 mm/s, machine = Concept M2, build orientation = Z, surface condition = as-built, the outputs would be PC1, PC2, and PC3. These outputs are then used as the input to the SP model.

The SP model used training data from the same PC space as the PS data. This is an advancement compared to the previous version of the DTMM where the PS and SP PC scores were the result of independent analyses. In this round, the PC scores generated by the PS method were used as the scores for the SP training data. There were 95 samples with HCF testing data, but only 58 samples with surface roughness scan data. Because of this, the PC scores for some samples were repeatedly used for all SP specimens that shared a similar condition. For example, an unpolished Z specimen from build 1 without any surface scan data used the PC scores from a different unpolished build 1 Z specimen. This method worked well for all but a few specimens. A few "imaginary" specimens were included in the PS PCA in order to get PC scores for polished specimens from builds 2, 5, 9, 10, and 11 because there was no surface roughness scanning data for polished specimens from those builds. Since most polished specimens had a similar and much lower

surface roughness, these "imaginary" specimens were associated with the flat surface roughness data from a polished specimen from build 1 data and the corresponding porosity data for their respective builds. In the end, complete PC scores were obtained for each of the 95 tested HCF specimens.

In tandem, the PS and SP training data sets can be employed with the three described regression techniques to create full process-structure-property (PSP) models. These models can take any combination of input variables and provide the expected HCF strength for that parameter set. Comparing the MR, SVR, and GPR, there is observable difference in the accuracy of the SP model. As shown in Figure 83, the error is highest in the MR model and lowest in the GPR model. This matches the trends observed in previous DTMM versions. In the cross-validation plots, there is a soft limit observed for the predicted values of max HCF stress range around 350 MPa. This limit is not well understood and may be due to the nature of regression techniques to be swayed toward the average of large sets of data and away from any outliers. This results in conservative strength predictions for the PSP models.

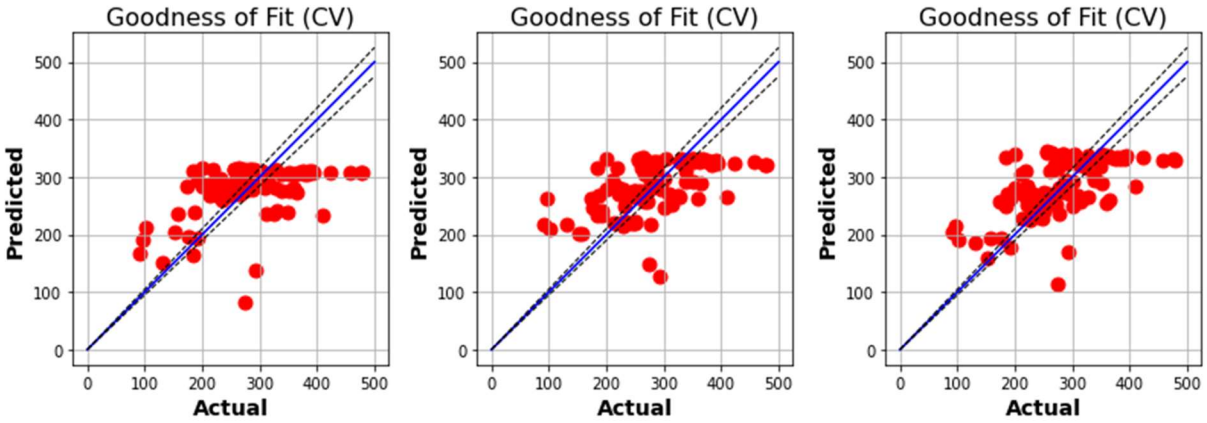

Error	MR	SVR	GPR
MAE	55.96	52.62	47.53
MSE	4975.70	4398.58	3924.74
RMSE	70.54	66.32	62.65
MAPE	23.75	22.62	19.92

Figure 83. Leave-One-Out Cross-Validation Results (Units are Stress Range in MPa) for MR (Left), SVR (Middle), GPR (Right) with Table Detailing the Errors of these SP Regression Models (MAE = Mean Absolute Error, MSE = Mean Squared Error, RMSE = Root Mean Squared Error, and MAPE = Mean Absolute Percentage Error)

Using the models to create prediction maps for the hatch spacing vs. scanning speed space visualizes the effect of the input parameters on the strength of the resultant additively manufactured component. Shown in Figure 84, the process map for the Concept M2 Z specimens differs slightly from the one for XY specimens, but they both show a similar trend with highest strength predicted in the region with the highest energy density (here, smaller hatch spacing and lower scanning speed). Similar peaks are observed in the process maps for both the Concept and Renishaw machines for Z specimens in the as-is condition. Even though the two plots are based on entirely different subsets of the training data set, they show a similar trend that matches that observed in testing. This shows that these ML techniques, namely the SVR used to generate these plots, are quite robust in their ability to interpolate relationships between a diverse set of training data points.

These updated predictions deviate from what was predicted with the initial DTMM that was trained on a smaller data set (shown in Figure 81). While the new predictions still indicate that the lower hatch spacing is desirable, the conclusion regarding scanning speed is opposite of what was predicted with less data. With the additional data used in training, the model now has more confidence that the smaller hatch spacing and

lower scan speed, of the conditions considered in the coupon testing, will most likely generate a more fatigue resistant microstructure.

This updated prediction turns out to be consistent with selecting the process parameters having the highest volumetric energy density. Considering most defects were the lack-of-fusion type, this means volumetric energy density was too low in most, if not all, of the builds in the coupon testing program. It is worth noting that all builds were originally centered on a higher energy density. The builds were adjusted to a lower energy density after Aerojet Rocketdyne reported that the higher energy process settings were unworkable on their Concept M2 machine. The model also suggests that smaller hatch spacing is more significant than lower scanning speed, which explains why the model with less data also predicted that smaller hatch spacing should be better but struggled to hone in on the optimum scanning speed in the initial DTMM.

It should also be noted that microstructural specimens were used to determine the characteristic porosity of each build. By doing this, it is assumed that the porosity measured in the microstructural specimens is statistically similar to that in the gauge section of the HCF specimens. However, this project showed that there were considerable differences in the porosity, in terms of volume fraction, sizes, and distribution, among the microstructural specimens and likely among the fatigue and tensile specimens. This is thought to be the primary cause of the model's accuracy limitations that were shown in Figure 83. A better correlation would be obtained by measuring the porosity in the gauge section of the HCF specimens themselves instead of using the microstructural specimens as a surrogate. However, this requires a non-destructive method such as high-resolution micro X-ray computed tomography, which was outside the scope of the original work statement.

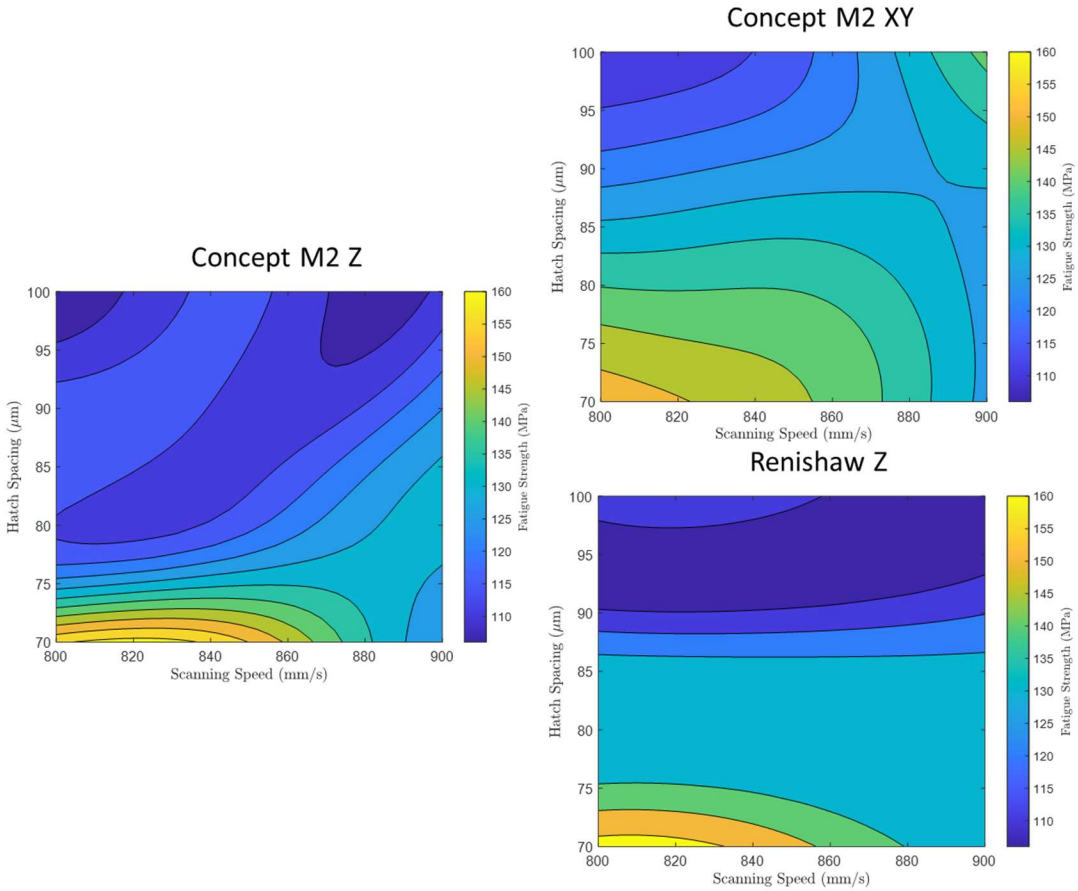

Figure 84. Process Parameter Contour Maps Generated by the Final DTMM with the SVR Method Showing the Prediction Surfaces for Concept M2 Z vs. XY as well as Concept M2 Z vs Renishaw Z. All Plots are for the As-Is Condition and Fatigue Strength is Given in Terms of Stress Amplitude for R = 0.1 Loading.

M. FATIGUE TEST OF THE SECOND INJECTOR

As discussed in section 2.C.2, the hot-fire testing of the second injector did not generate the stress necessary for fatigue damage. Therefore, the second injector was fatigued in a uniaxial servo-hydraulic test system to simulate the HCF loading that the injector would experience in an RDE with greater vibration. The second RDE injector was built using the build 3 parameters that were found to be optimum based on the DTMM version at the time the second injector was built. As a reminder, the build 3 parameters are a scanning speed of 900 mm/s, a hatch spacing of 70 microns, and the alternative stress relief and annealing cycle with HIP'ing.

The HCF test was conducted on the injector after it had been evaluated in hot-fire tests. The HCF test consisted of placing the RDE injector on a support apparatus that transferred force through the injector vanes and subjecting it to compression-compression cycling at a cyclic frequency of 10 Hz. This resulted in a cyclic bending stress in the vanes between the fuel nozzle and outer cylinder of the RDE injector. This is the same location where HCF cracks are expected to form in an operating RDE injector due to the cyclic wobbling of the centerbody. The orientation of the maximum principal cyclic stress along the surface of the vane at the expected fatigue crack location corresponds to an XY-oriented specimen (the stress plane is parallel to the build direction). Note that while a compression test apparatus was used, the maximum principal stress in the resulting bending of the vane was a tensile stress. It should also be noted that the stress concentration location in the RDE injector was not on an edge having a build support, which was found in the coupon testing to greatly influence the XY-oriented specimen HCF strengths.

The fatigue step test method that was used for the coupon HCF specimens was also used for the HCF test of the RDE injector. A constant amplitude sine wave was applied, cycling between a minimum compressive pre-load and maximum compression. The displacement evolution was monitored to determine if and when fatigue cracks formed in the vanes. The test was conducted at room temperature in lab air.

The initially applied cyclic loading was selected to generate a theoretical cyclic stress at the fatigue limit based on coupon data for build 3 parameters in the XY orientation. This conservative initial step did not make any considerations for notch sensitivity, which will be discussed shortly. The theoretical stress at the critical location in the vane as a function of the compressive force applied was determined by finite element analysis and is shown in Figure 85 as the blue line (each loading step is annotated in the figure). Since the fatigue strength for build 3 in the XY-orientation is 269.1 MPa stress range based on an average of the results from two HCF tests on build 3 in the XY direction, the stress range for the first step of the HCF test program was set to this value. To achieve this stress range at the hot spot location with a minimum to maximum stress ratio of 0.1 as was used in the coupon tests, the maximum compression force was set to 2742 lbs., and the minimum compressive force was 274 lbs. The mean force was 1508 lbs. The RDE injector was loaded to the mean force and then cycled between the maximum and minimum force limits.

The RDE injector survived the first step ending at 2×10^6 cycles. While some reduction in compliance was observed in the first step, which may indicate some fatigue damage, the force-displacement response stabilized during the step. Subsequent steps conducted are summarized in Table 16. The load was increased in step 2 by 8%, in step 3 by 12%, in steps 4-7 by 15% and in step 8 by 20%.

Table 16. Incremental 2 x 10^6 Cycle Steps for Fatigue of the RDE Injector

Step	Max Force (lbs.)	Min Force (lbs.)	Force Range (lbs.)	Theoretical Stress Range (MPa)	Theoretical Stress Amp. (MPa)
1	2742	274	2468	269.1	134.6
2	2961	296	2665	290.6	145.3
3	3316	332	2984	325.3	162.7
4	3821	382	3439	375.0	187.5
5	4394	439	3955	431.2	215.6
6	5053	505	4548	495.9	248.0
7	5801	580	5221	569.2	284.6
8	6961	696	6265	683.1	341.5

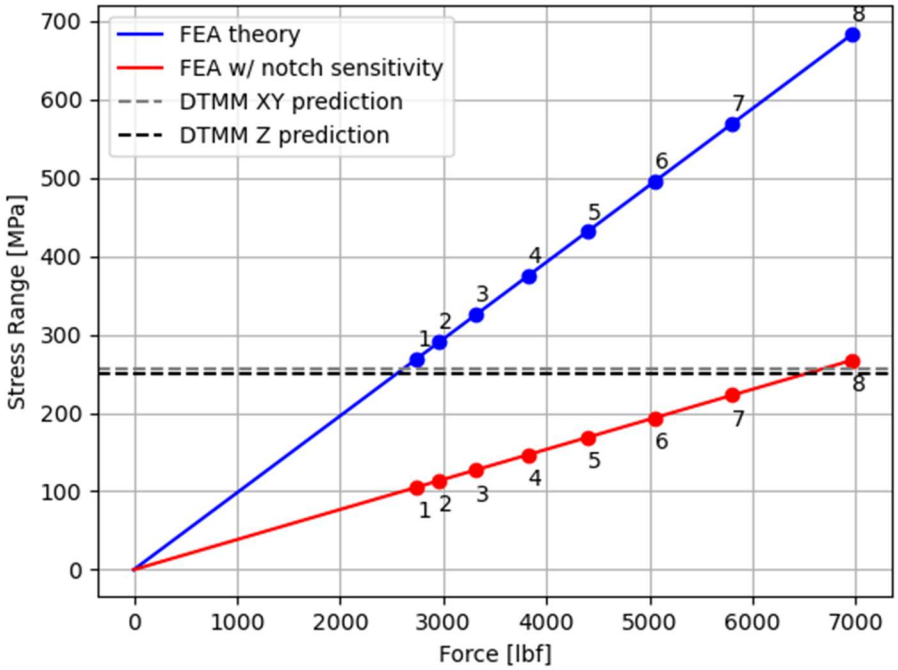

Figure 85. Relationship Between Applied Compressive Force and Stress at the Critical Location in the Vane where the Fatigue Crack is Expected to Form (Numbers Indicate the Loading Step)

Setting the Step 1 parameters to the fatigue limit of Build 3 in XY orientation was expected to be conservative for a few reasons. As noted in the coupon test data discussed in previous quarterly reports, larger lack-of-fusion defects that remained even after filing and polishing were observed near edges with build supports, resulting in reduced fatigue strength. The site of maximum stress in the ligament in the injector is on the top side of the build and hence the injector will likely have a fatigue strength closer to a condition without these larger lack-of-fusion defects associated with build supports. In addition, since the vane is experiencing a bending stress, the amplitude of the stress reduces with depth into the vane, unlike the HCF specimens that experienced uniform cyclic stress across the gauge section. The volume of material experiencing the maximum cyclic stress is also smaller in the RDE injector than in the coupon specimens. In the coupon specimens, it is statistically more likely that a larger flaw will be present somewhere in the highly stressed volume. The gradient in stress and volume effects were not considered to further maintain some conservatism in the initial load level selected.

These effects are addressed to some degree by considering the notch sensitivity of the material. Materials subjected to fatigue conditions are not always fully susceptible to stress concentrations. This is particularly important in this application because the peak stress is only generated by a stress concentration in a sharp fillet; the baseline stress field is benign. A material with low notch sensitivity would actually experience an effective cyclic stress that is much less than the theoretical prediction, and fatigue should occur at a higher load than expected. True knowledge of the notch sensitivity in this application would require the inclusion of notched coupon geometries in the design of experiment that was used to train the DTMM. This was not possible within the scope of this project. However, we can obtain an approximate estimate by consulting handbook data for conventional Inconel 625 that has similar tensile properties to the additive material created in this project.

Notch sensitivity q is defined based on the actual stress concentration factor in fatigue, K_f, and the theoretical stress concentration factor, K_t:

$$q = \frac{K_f - 1}{K_t - 1} \tag{6}$$

We see that q ranges between 0, meaning the material ignores the stress concentration, to 1, where the full theoretical stress concentration is obtained. The notch sensitivity for a feature of length scale r can be estimated from the Neuber equation, where a has the same units as r and is a material constant:

$$q = \frac{1}{1 + \sqrt{\frac{a}{r}}} \tag{7}$$

The fatigue data for notched and unnotched annealed Inconel 625 from MIL-HDBK-5J were compared to estimate a value for a for Inconel 625: 0.085 inches. The theoretical prediction for maximum principal stress in the injector was studied parametrically as a function of fillet radius. A power law fit was constructed to extrapolate to the asymptotic stress value in the absence of a stress concentration. The notch sensitivity was then evaluated from equation 7 and used to find the actual stress concentration factor in fatigue, K_f. The asymptotic stress value was multiplied by the fatigue stress concentration factor to give the actual maximum principal stress for the purpose of evaluating fatigue strength. This adjusted curve is compared to the theoretical FEA prediction in Figure 86. Injector #2 has a 0.02-inch radius fillet, where it can be seen that the relatively low notch sensitivity of the material significantly reduces the fatigue load compared to the raw FEA prediction.

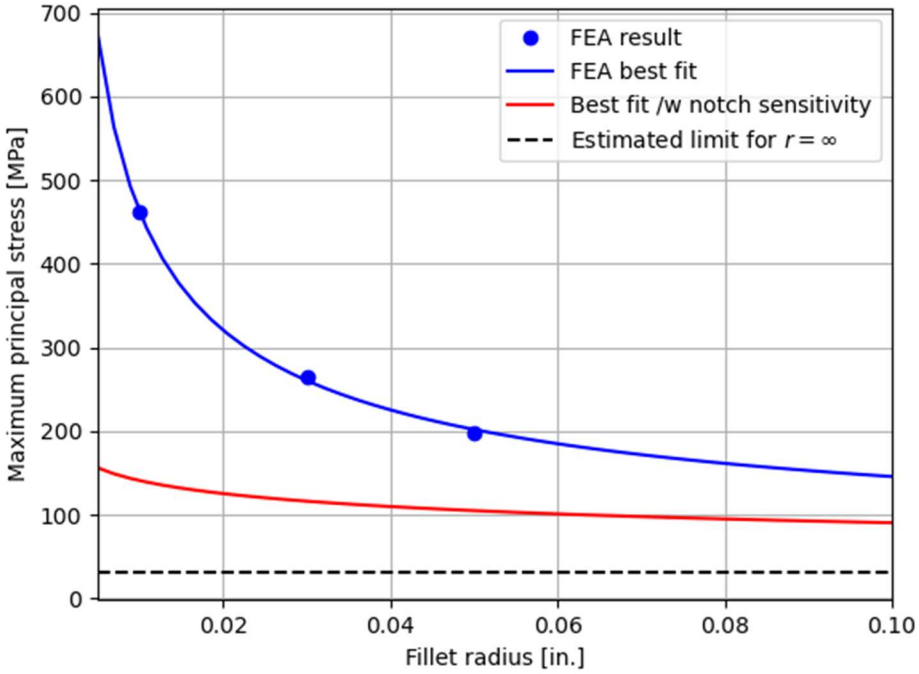

Figure 86. Maximum Principal Stress in the Injector as a Function of Vane Fillet Radius, FEA Theoretical Result Compared to the Result Adjusted for Notch Sensitivity

A total of eight steps of 2 x 10^6 cycles each were applied with the last step having a theoretical stress range of 683 MPa at the critical point in the injector. An adjusted maximum principal stress vs. load relationship is also included in Figure 85, which shows that the actual stress range relevant to fatigue was more likely 267 MPa. This is slightly above the final DTMM model predictions for the part's fatigue strength. Testing concluded after step 8 due to the project reaching the end of the period of performance. No failure occurred, demonstrating that the parameters recommended by the DTMM resulted in a part with adequate fatigue strength. The DTMM made a conservative prediction, which is a consequence of accuracy issues that were discussed in the previous section.

N. TENSILE TEST RESULTS

Recall that each sample build plate included round tensile specimens in addition to the HCF and microstructure specimens. Each of these specimens was tested to determine the variation of elastic modulus, yield strength, and ultimate strength with the process parameters. While this information was not incorporated into the DTMM that focused on fatigue strength predictions, it is provided as an addendum that provides another view of the relative quality and uncertainty of each build.

The vertical specimens from builds 1-6 and build 9 were tested in the as-is condition (aside from machining to thread the grips and a machining pass to improve surface finish). The other specimens could not be tested directly because of macroscopic flaws such as visible cracks and warping. All specimens from builds 7 and 8 as well as all horizontal specimens from builds 6 and 9 were unusable because of the widespread nature of these defects. However, other specimens, namely some of the horizontal specimens from builds 1-5 and some of the vertical and horizontal specimens from builds 10 and 11, had sufficient material intact to salvage a tensile specimen of smaller dimensions. The number of specimens that could be salvaged varied from build to build, and in no cases were all four specimens of a given type reclaimed. The outcome of each build is documented in Table 17. Therefore, less data is available for the horizontal orientation than the vertical.

Table 17. Tensile Specimen Outcomes

Build	Vertical	Horizontal
1	AS-BUILT 4/4	SALVAGED 1/4
2	AS-BUILT 4/4	SALVAGED 2/4
3	AS-BUILT 4/4	SALVAGED 2/4
4	AS-BUILT 4/4	SALVAGED 1/4
5	AS-BUILT 4/4	SALVAGED 2/4
6	AS-BUILT 4/4	UNUSABLE
7	UNUSABLE	UNUSABLE
8	UNUSABLE	UNUSABLE
9	AS-BUILT 4/4	UNUSABLE
10	SALVAGED 3/4	SALVAGED 1/4
11	SALVAGED 3/4	SALVAGED 2/4

All tensile test data are summarized in the following figures. Results from builds 2 and 6 are grouped together in the data because of their identical build parameters. They are equally probable outcomes of applying those build settings, similar to the specimen-to-specimen variation within a single build. Figure 87 and Figure 88 document the elastic properties of each build with yield strength and elastic modulus, respectively. Yield strengths are consistent across the Aerojet Rocketdyne (AR) builds with only minimal variation. Yield behavior is mildly anisotropic, with the vertical specimens achieving a slightly higher yield strength. The SwRI builds resulted in lower yield strengths than the AR builds, further demonstrating the influence of SLM machine type on material properties.

Significant variation in elastic modulus is apparent across the builds. Results are centered on the handbook value for wrought material with scatter both above and below this value. A precision uncertainty was estimated by repeating the modulus test on the same sample ten times including the complete removal and reapplication of grips and extensometers. The maximum and minimum values measured in the repeatability experiment were used to construct a relative precision uncertainty which is displayed about the handbook value in the figure. These lines bracket the magnitude of variation that is plausibly explained as experimental error. Notably, several builds exhibit variation outside of this range, and there are true physical differences between the specimens. Builds 2 and 6 stand out as having superior elastic properties. Their results are in line with expected values and show the smallest variation. The material also appears isotropic within the uncertainty of the experiment, which validates the assumptions used in the mechanical analysis of the injector.

Figure 89 shows the ultimate tensile strength and Figure 90 gives the elongation to failure. Together, these figures describe how the builds differ in the plastic regime. Builds 2 and 6 once again take the lead in ultimate tensile strength with values that are higher and more consistent than the other builds. In contrast, build 5 is clearly deficient with strengths that are lower and more variable than all the others. SwRI specimens generally have lower ultimate strength than the AR specimens, as was observed with yield

strength. There is no clear winner in the elongation to failure – there is extensive variation across the board. However, builds 2 and 6, 9, 10, and 11 have the highest minimum elongation.

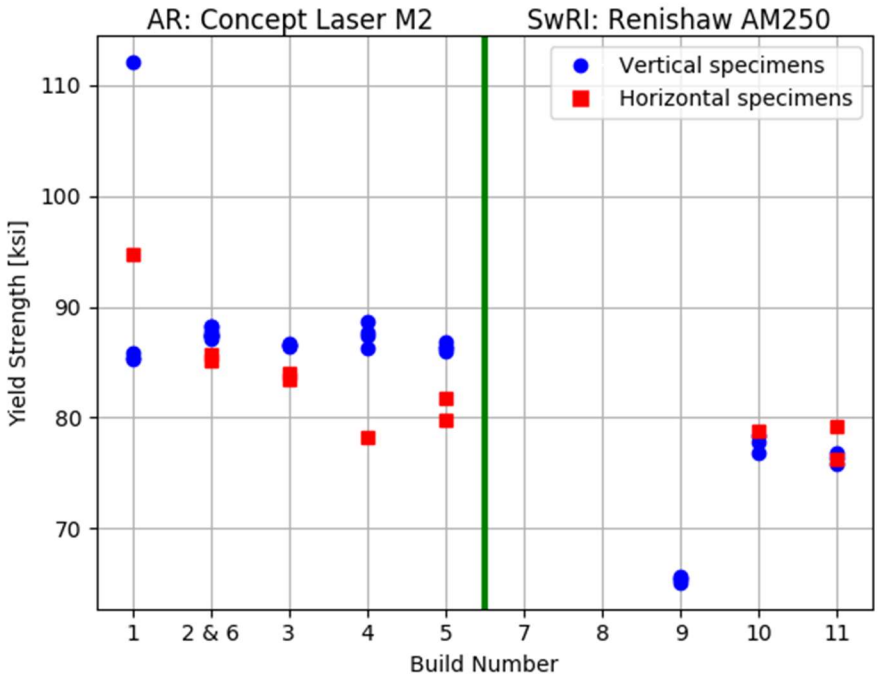

Figure 87. Yield Strength of all Viable Tensile Specimens, Builds 2 and 6 Grouped Together (Builds 7 and 8 Were Not Viable)

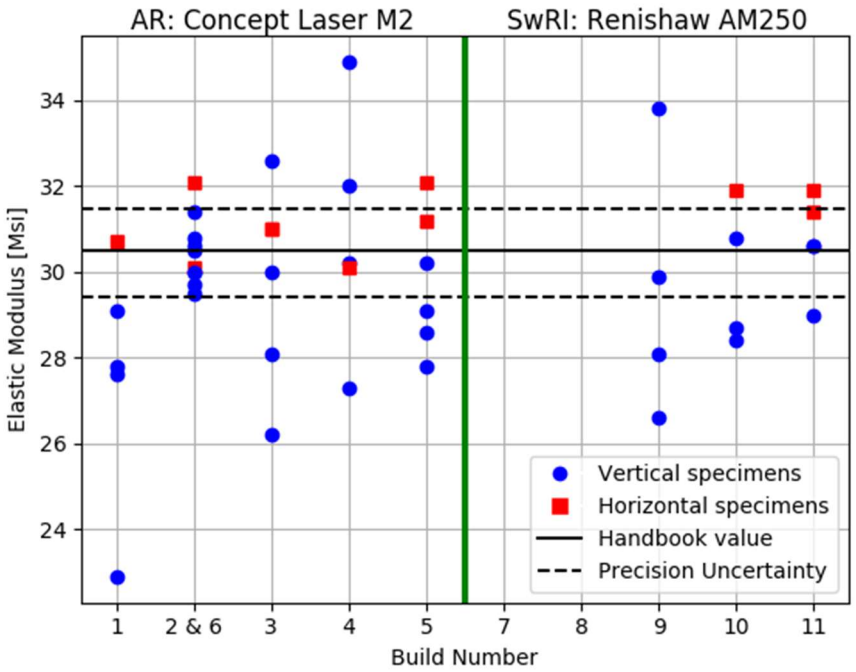

Figure 88. Elastic Modulus of All Viable Tensile Specimens, Builds 2 and 6 Grouped Together (Builds 7 and 8 were Not Viable)

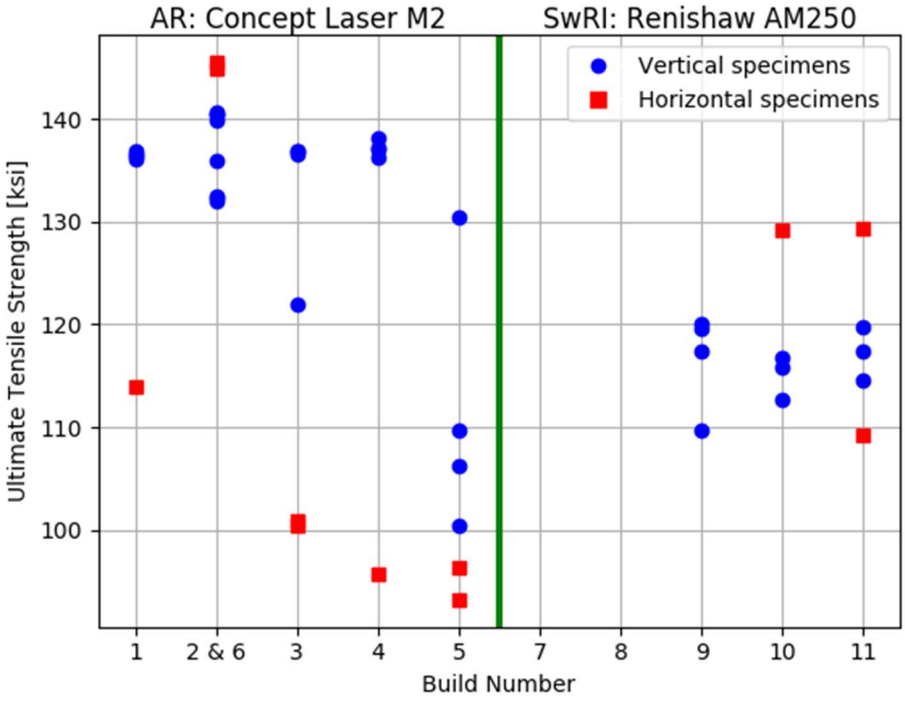

Figure 89. Ultimate Tensile Strength of All Viable Tensile Specimens, Builds 2 and 6 Grouped Together (Builds 7 and 8 were Not Viable)

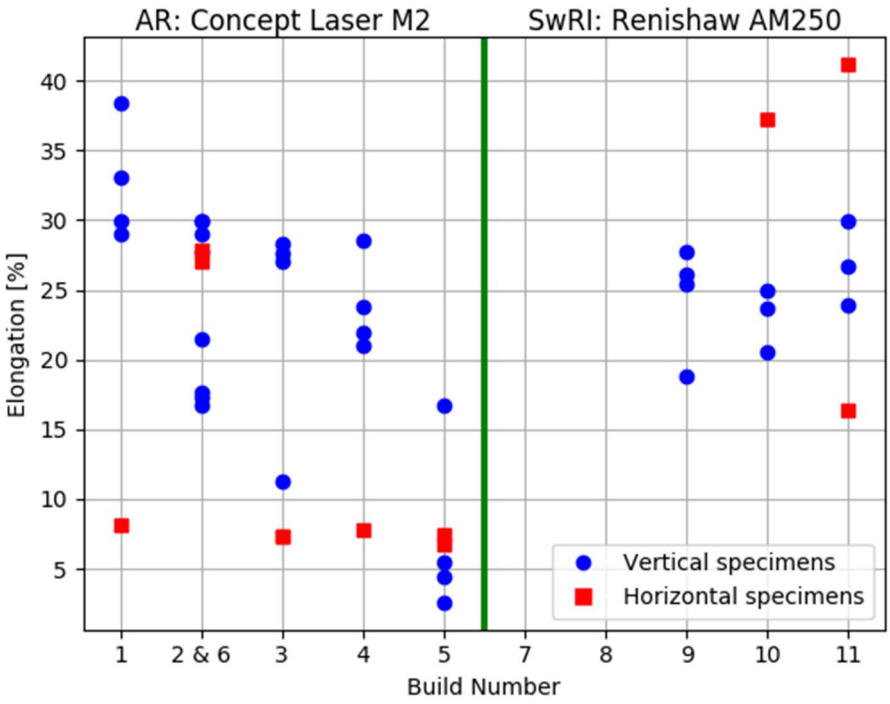

Figure 90. Elongation at Failure for All Viable Tensile Specimens, Builds 2 and 6 Grouped Together (Builds 7 and 8 were Not Viable)

O. INVESTIGATION OF TENSILE TEST DISCREPANCIES BETWEEN REPEATED BUILDS

The material specimen design of experiment included two pairs of repeat builds. The first pair, consisting of builds 2 and 6, were built with the same settings on the exact same machine at AR. The builds were separated in time by several months. The second pair, consisting of builds 5 and 9, were built with the same settings but on different machines. Build 5 was performed at AR on a Concept M2 machine, while build 9 was performed at SwRI on a Renishaw 250. However, the tensile test performance was not consistent within these seemingly identical builds.

Figure 91 shows that build 6 specimens have less ultimate strength and ductility than those from build 2, and Figure 92 shows that builds 5 and 9 follow entirely different stress-strain curves. While some disparity is expected for builds 5 and 9 considering the machines have contrasting laser architectures (continuous vs. pulsed) and AR used a proprietary powder chemistry, the differences are nonetheless striking. The discrepancy between builds 2 and 6 is more troubling, considering these were built on the same exact machine at AR according to identical specifications. These disconnects challenged the concept of the DTMM, which is prefaced on a consistent linkage between process parameters and material properties.

Table 18. Material Sample Build Matrix (Builds Highlighted in Orange Used the Same Settings on the Exact Same Machine; Builds Highlighted in Blue used the Same Settings on Machines from Different Manufacturers)

#	Pattern	Velocity (mm/s)	Hatch Spacing (microns)	Heat Treat Cycle	Machine	Energy Density (J/mm^3)
1	---	800	70	SR+HIP	AR	49.1
2	++-	900	100	SR+HIP	AR	30.6
3	+-+	900	70	NSR+HIP	AR	43.7
4	-++	800	100	NSR+HIP	AR	34.4
5	Center Point	850	85	SR+HIP	AR	38.1
6	++-	900	100	SR+HIP	AR	30.6
7	+++	900	100	NSR+HIP	SwRI	30.6
8	-+-	800	100	SR+HIP	SwRI	34.4
9	Center Point	850	85	SR+HIP	SwRI	38.1
10	+--	900	70	SR+HIP	SwRI	43.7
11	--+	800	70	NSR+HIP	SwRI	49.1

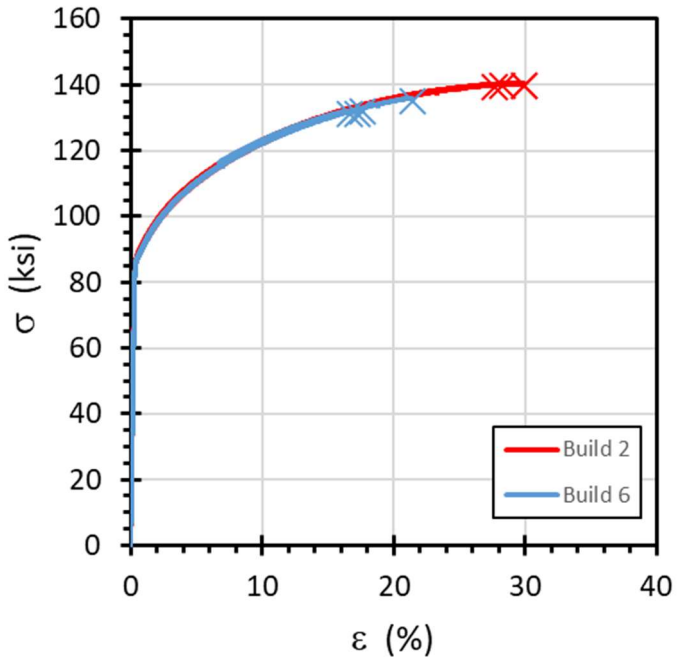

Figure 91. Tensile Test Results for Build 6 Compared to Build 2

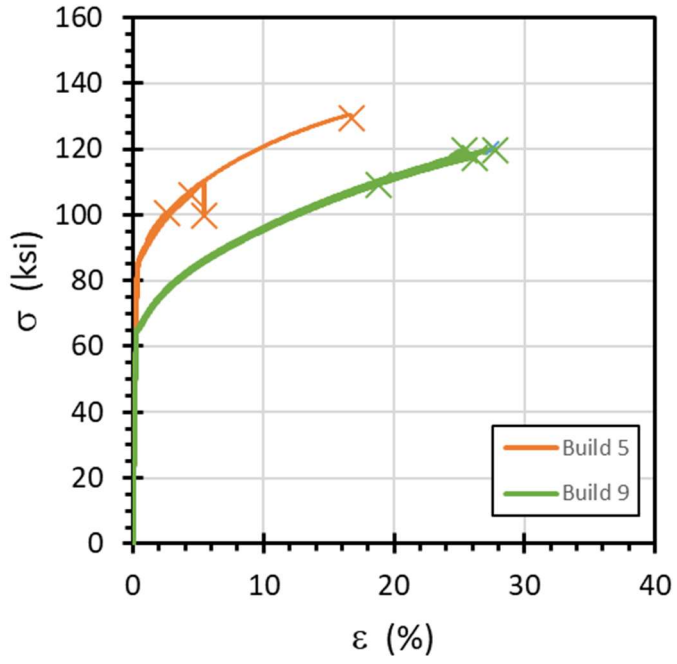

Figure 92. Tensile Test Results for Build 5 Compared to Build 9

The manufacturing logs were reviewed to determine if builds 2 and 6 were processed with the same materials, settings, and procedures. Build logs consist of operator notes as well as history files stored in the Concept M2 machine itself. These logs all indicate that builds 2 and 6 were built with the same powder composition and process settings. The recorded heat treatment data show that each build experienced the same stress relief and hot isostatic pressing cycles, as shown in Figure 93 through Figure 96. Vacuum

conditions were maintained throughout the stress relief cycle for both builds. A side observation is that the stress relief treatment extended beyond the specification of 60 +15 / -0 minutes, introducing a possible disconnect between the SwRI and AR stress relief treatments. The team reviewed this departure and determined that the unequal durations would only result in few, if any, differences in the macroscopic warping of SwRI vs. AR specimens. There should be no impact on microstructure.

The stress relief cycle was performed with all specimens still attached to the build plate, therefore it was impossible to accidentally omit specimens from the treatment. This error was a possibility for the HIP cycle, because parts were separated in order to fit inside the oven envelope. However, pictures captured during the manufacturing process confirm that all material specimens were placed in the HIP oven, as shown in Figure 97. In conclusion, builds 2 and 6 were in fact built according to the exact same process, and any variability in outcomes is due to uncontrollable factors inherent to the selective laser melting process.

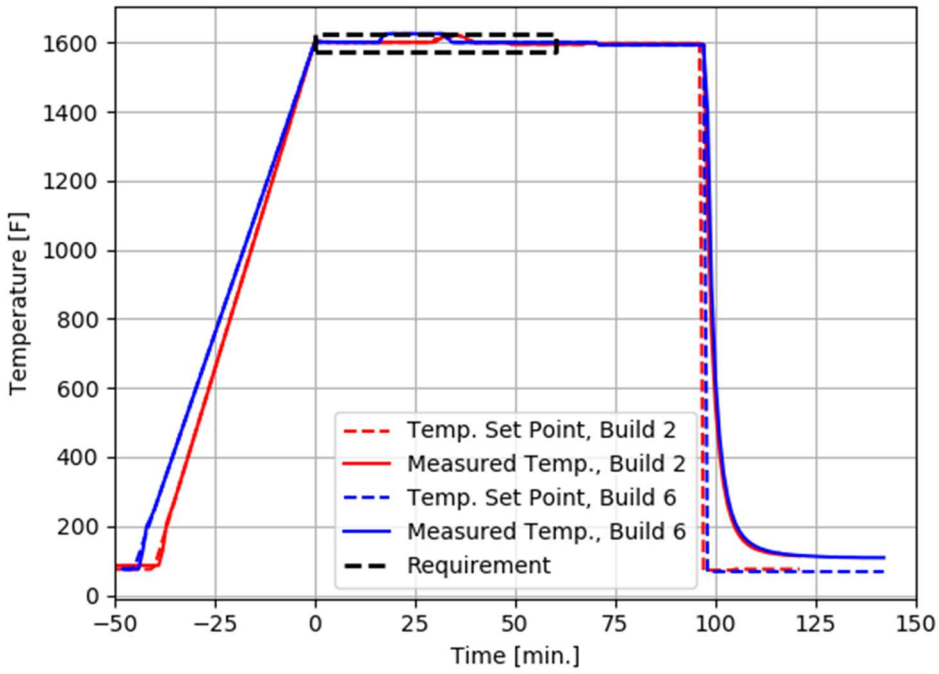

Figure 93. Stress Relief Temperature Profiles for Builds 2 and 6

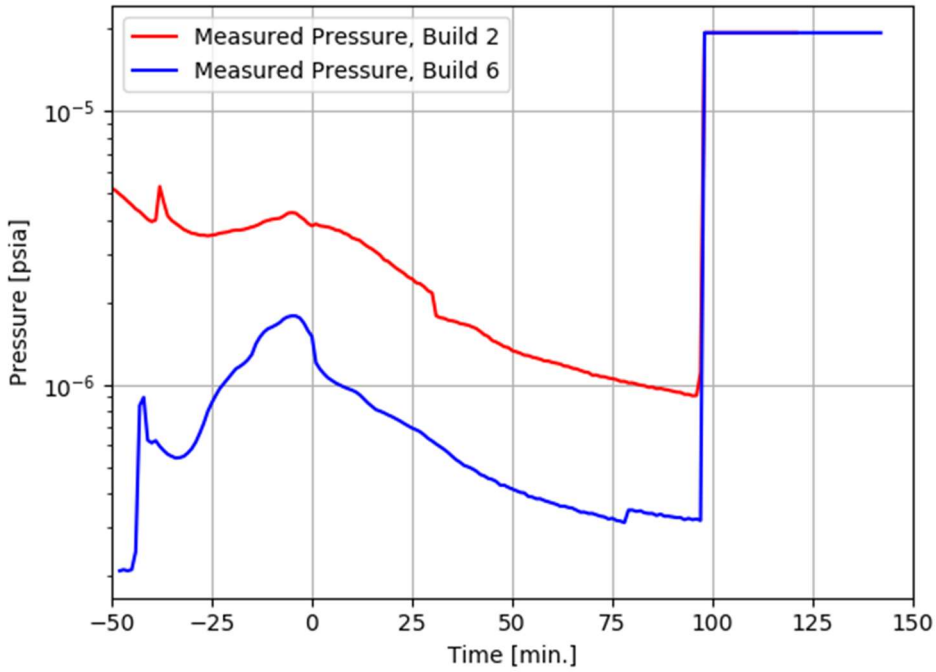

Figure 94. Stress Relief Pressure Profiles for Builds 2 and 6

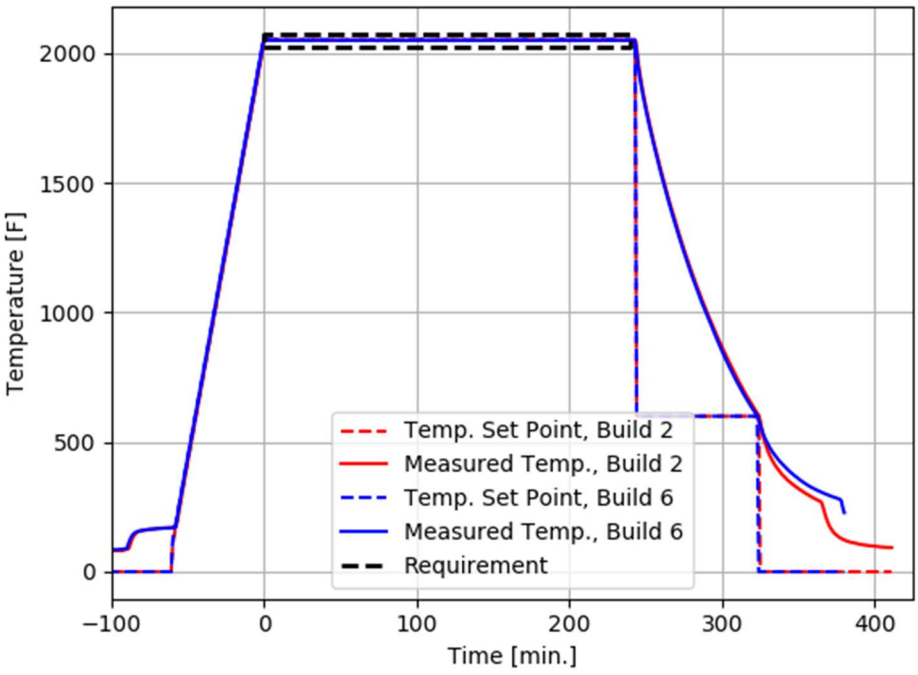

Figure 95. Hot Isostatic Pressing (HIP) Temperature Profiles for Builds 2 and 6

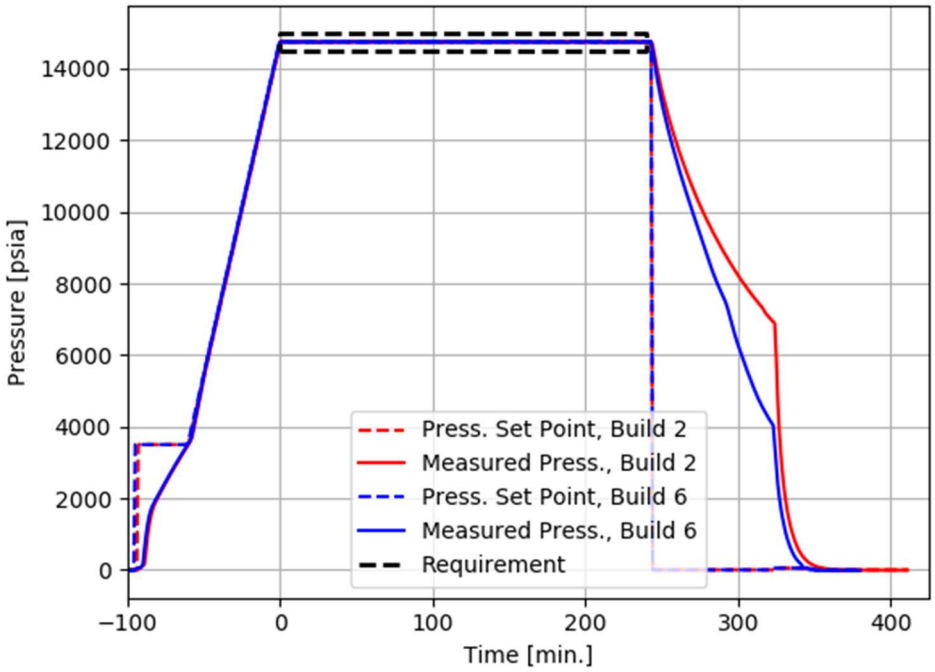

Figure 96. Hot Isostatic Pressing (HIP) Pressure Profiles for Builds 2 and 6

Figure 97. All samples from Builds 2 (left, paired with Build 1) and 6 (right, paired with Build 5) were Placed in the HIP Oven

Metallurgical analysis was performed on the tensile specimens to determine the physical basis for the difference in tensile properties between builds 2 and 6. Scanning electron microscopy (SEM) was used to classify the microstructure in the gage section of a tensile specimen from builds 2 and 6. Results are given in Figure 98 and Figure 99 for builds 2 and 6, respectively. Both image sets indicate a semi-cellular, re-solidified morphology with elongation parallel to the axis of the tensile bar. There is preferential distribution of precipitates along grain boundaries, and the precipitate size and density distribution is similar between the two builds. In other words, there are no discernable differences in the microstructures, which is consistent with them having been built according to identical parameters.

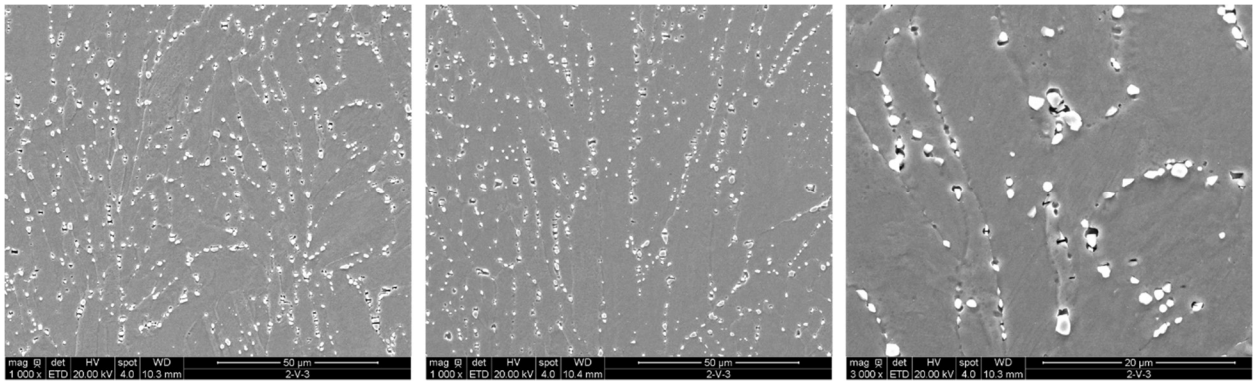

Figure 98. Scanning Electron Microscope Images of the Gage Section Microstructure of Build 2 Tensile Specimen #3

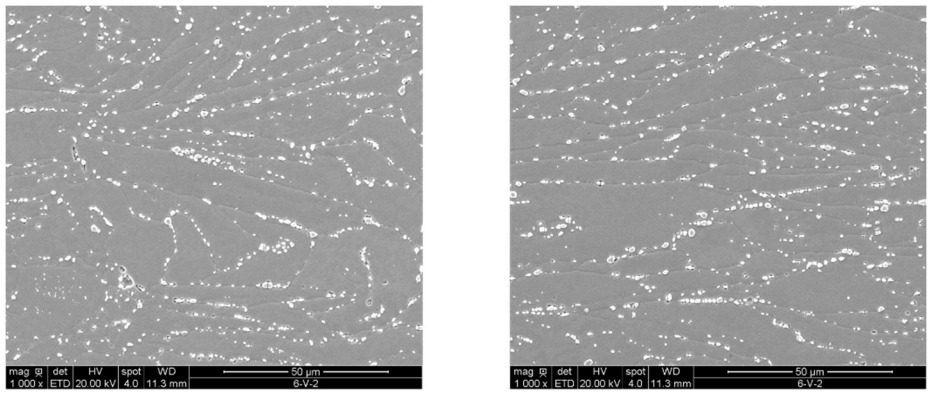

Figure 99. Scanning Electron Microscope Images of the Gage Section Microstructure of Build 6 Tensile Specimen #2

Stereoscopic imagery was then used to quantify porosity in the vicinity of the fracture surface. A review of the images shown in Figure 100 shows that both the build 2 and build 6 samples appear to have minimal porosity (0.185% and 0.024%, respectively), which is once again consistent with identical build parameters. Note that the sample with less elongation, build 6, is actually the one with less porosity.

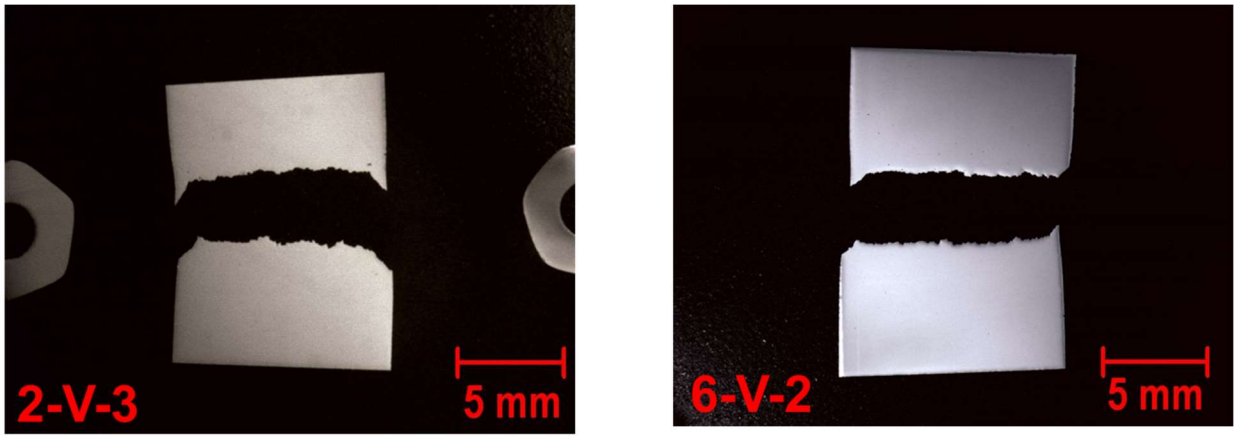

Figure 100. Stereoscopic images of polished samples to determine porosity of a tensile specimen from build 2 (left) and build 6 (right)

SEM analysis was performed on the fracture surfaces as shown in Figure 101 and Figure 102 for builds 2 and 6, respectively. These figures show SEM images at the locations marked in the overall view of the fracture surface. In both cases, the imaging indicates the fracture surface consists of equiaxed dimples that

are indicative of tensile overload. A limited amount of secondary cracks were also observed. However, the SEM does reveal a key difference between the two builds. The build 6 specimen failure contains faint directional features that indicate the fracture originated at a surface morphology anomaly on the outer diameter (location 1 in the figure). This anomaly is a pore that was created by incomplete fusion, meaning it was not melted together during the SLM process.

The HIP process reduces porosity internal to the part but is unable to correct surface defects. Figure 103 highlights a few of these surface defects that are visible in a build 6 tensile specimen after HIP but before final machining. All tensile specimens were lightly machined in the gage section for a consistent surface finish, but this operation was apparently too shallow to remove all surface defects. Therefore, the build 6 specimens failed at a lower elongation and correspondingly lower ultimate tensile strength because of slightly higher porosity that resulted in a greater concentration of surface defects.

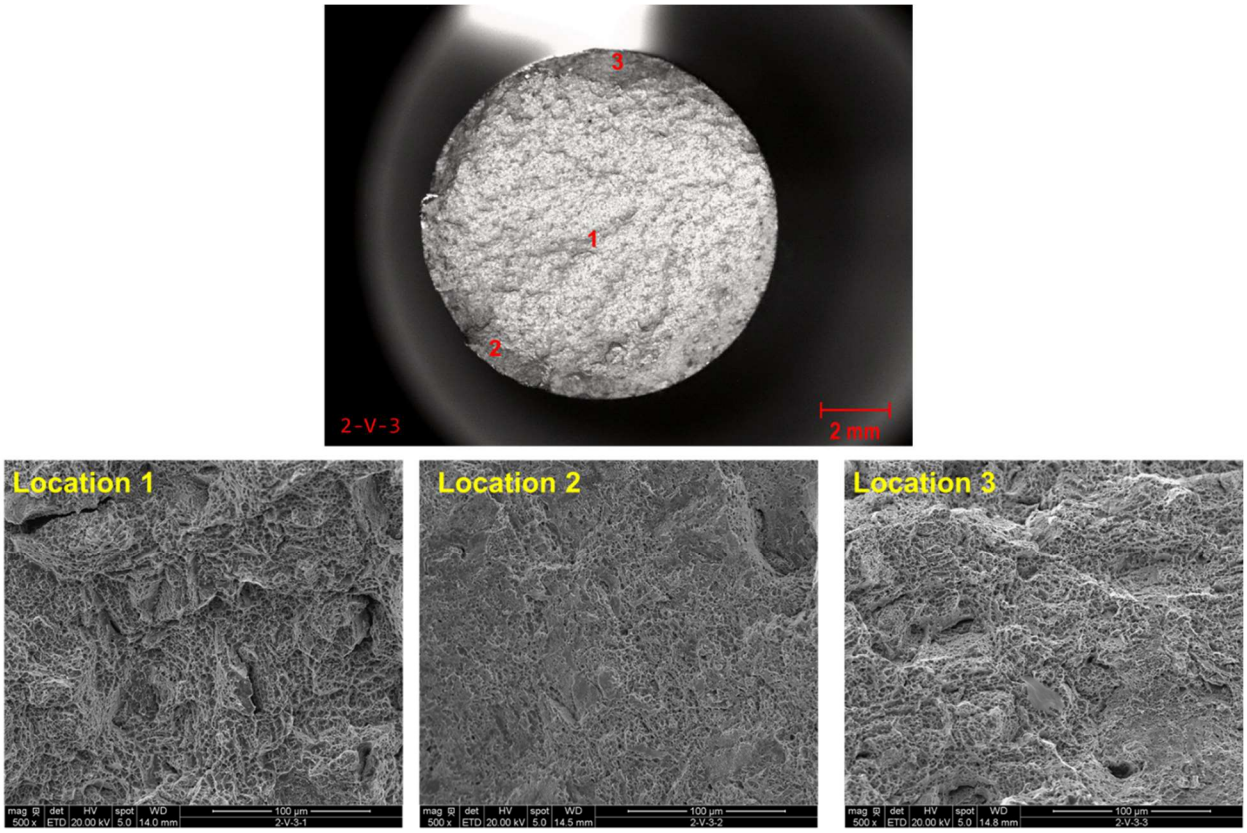

Figure 101. Scanning Electron Microscope Analysis of the Fracture Surface in Build 2 Specimen #3

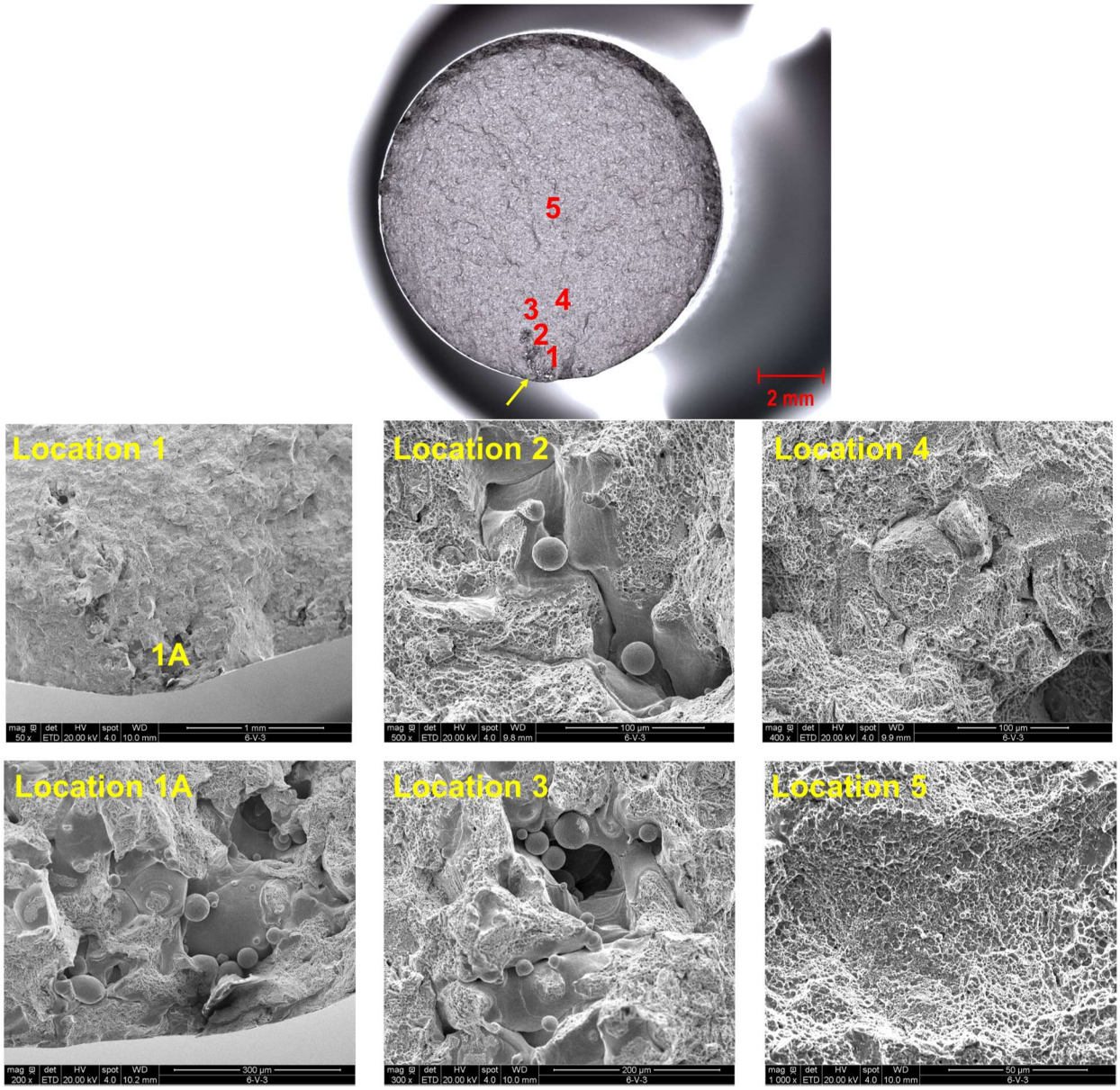

Figure 102. Scanning Electron Microscope Analysis of the Fracture Surface in Build 6 Tensile Specimen #3

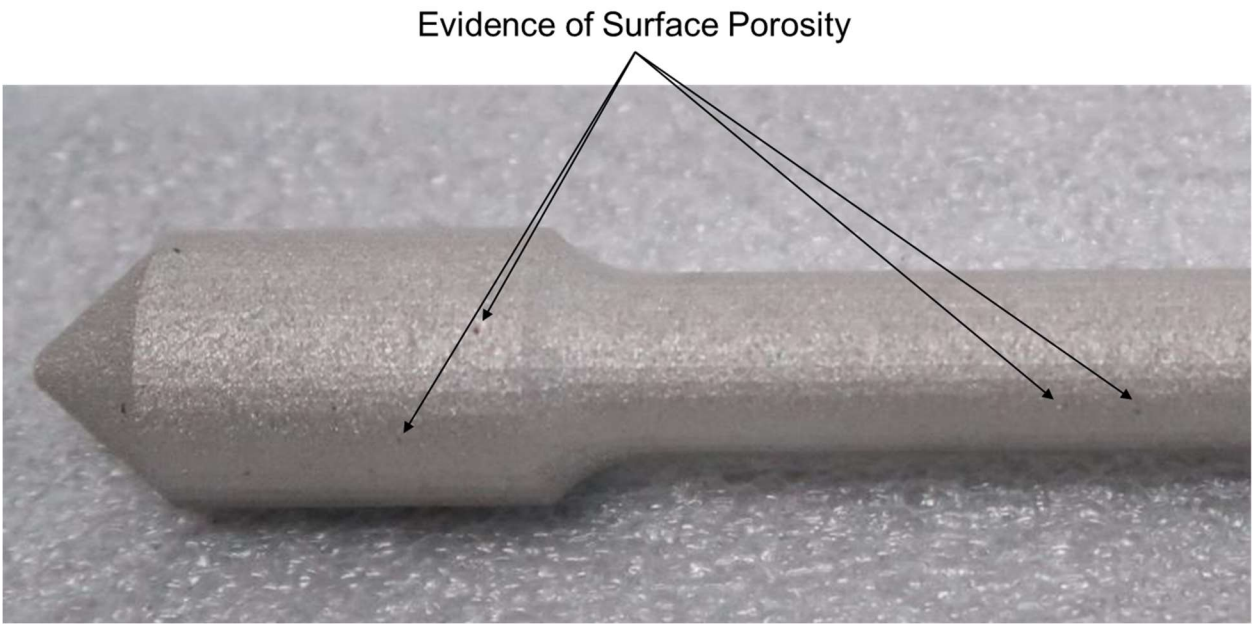

Figure 103. Surface Porosity Sites in a Build 6 Tensile Specimen before Final Machining

All data confirm that builds 2 and 6 were built on the same machine according to the same specifications, and the cause of the porosity variation remains unknown. There appear to be uncontrolled factors in the SLM process, such as minor drifts in delivered laser power for a given set point. One hypothesis is that SLM builds with low energy density are particularly sensitive to these fluctuations, as shown qualitatively in Figure 104. Builds 2 and 6 have the lowest energy density in the design of experiment, suggesting that they may be situated in the hypothesized zone of rapidly changing properties.

However, this explanation is unconvincing when the entire dataset is considered. As was shown in the previous section, Builds 2 and 6 have the most favorable tensile properties in the design of experiment – several higher energy density builds demonstrate degraded properties. Furthermore, an early trial build that was performed at energy densities above the levels included in the final design of experiment were terminated early because of severe defects that interfered with recoater operation. The only firm conclusion that can be made is that there is variability in the SLM process that is not yet controlled, and any robust characterization program must perform several repeats of all build samples to assess repeatability. Unfortunately, the budget for this program did not permit doing so, and this is left for future work.

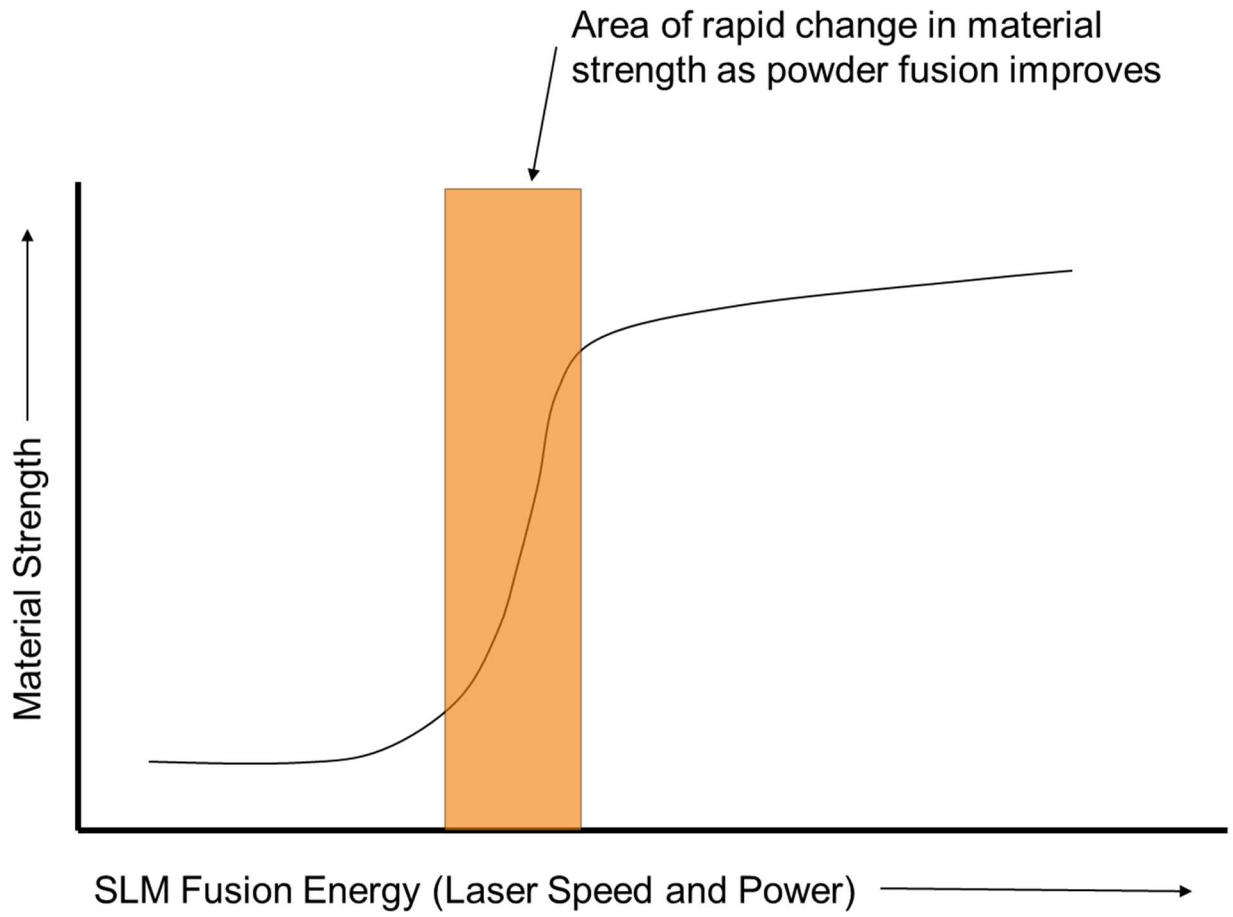

Figure 104. Hypothetical Relationship between Material Properties and Selective Laser Melting (SLM) Fusion Energy

The tensile specimens of build 5 (from AR) and build 9 (from SwRI) were similarly investigated to understand their different stress-strain curves. Both of these specimens failed in the grip section, unlike the build 2 and 6 specimens that failed in the expected gage section. Stereoscopic images, shown in Figure 105, display pronounced porosity near the fracture location in both samples. The tensile strengths of such defective builds are expected to be highly variable, and this partly explains the deviations between and within the two builds.

Of more interest are the microstructures of the two builds as shown in Figure 106 and Figure 107: they are completely different. Build 5 has a semi-cellular, resolidified morphology, similar to builds 2 and 6. Build 9, on the other hand, has an equiaxed, twinned structure whose precipitates are chemically distinct from the precipitates observed in build 5. These chemical variations are most likely a consequence of the different powder compositions used at AR vs. SwRI. These compositional differences are not publically available. For cost-share reasons, AR was required to use its proprietary version of Inconel 625 powder while SwRI used a standard Inconel 625 powder from a commercial vendor. These two compositions are known to be different in the minor alloying elements, but those differences remain undisclosed outside of AR. Aside from the chemical variations, the wholly distinct microstructures point to the specimens having unique thermal histories. This confirms the viewpoint that a SLM machine behaves as its own foundry, and nominally identical build parameters applied to two different machines can result in drastically different outcomes. Any material model must carry the particular SLM machine as an independent input variable.

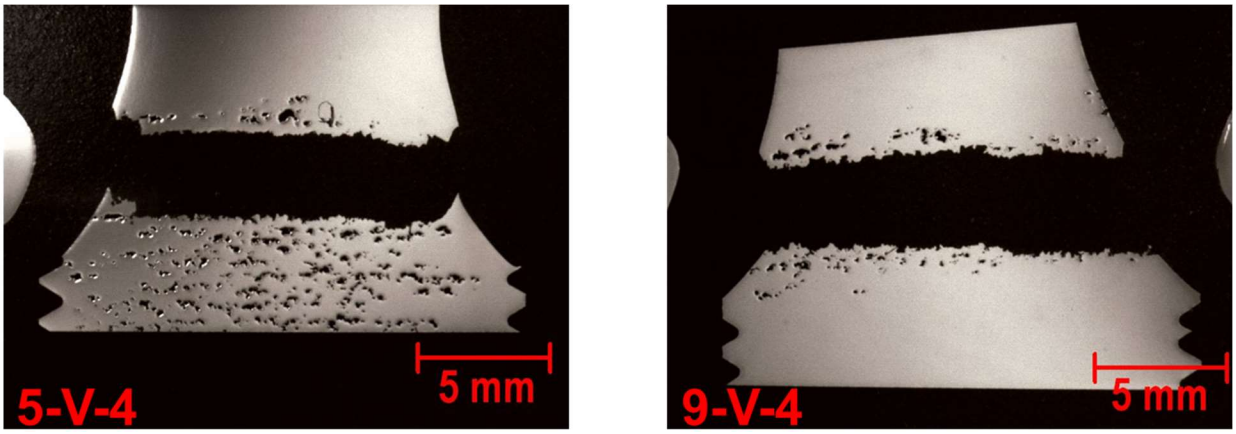

Figure 105. Stereoscopic Images of Polished Samples to Determine Porosity of a Tensile Specimen from Build 5 (left) and Build 9 (right)

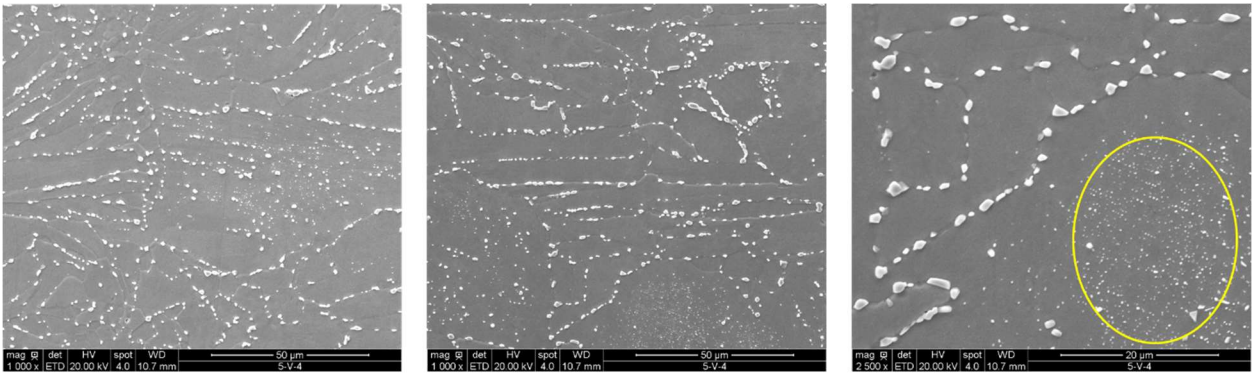

Figure 106. Scanning electron microscope images of the gage section microstructure of build 5 tensile specimen #4. Yellow circle shows an area of intragranular precipitates.

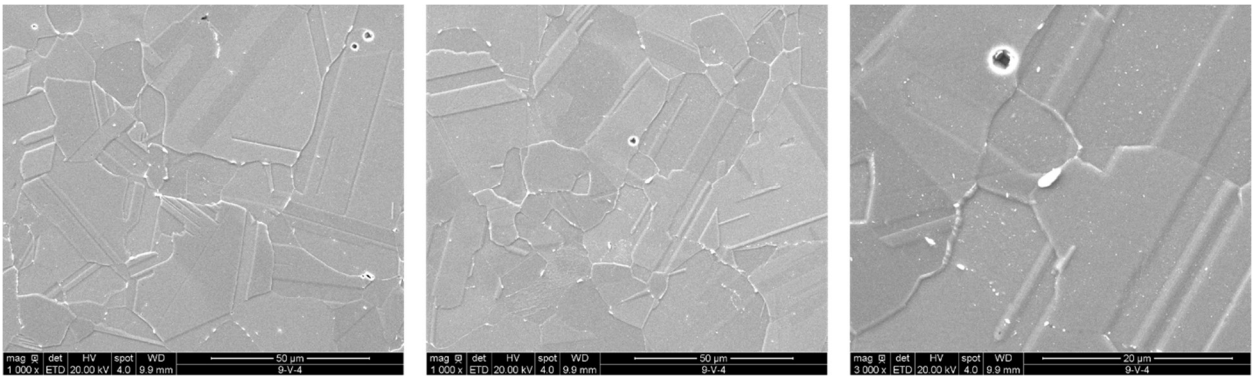

Figure 107. Scanning Electron Microscope Images of the Gage Section Microstructure of Build 9 Tensile Specimen #4

4. CONCLUSIONS

Pressure gain combustion has not seen practical application in either power generation or propulsion systems because of extra pressure losses upstream and downstream of the combustor element. There are pressure losses in the injector element that adds fuel and oxidizer to the combustion chamber, and there are pressure losses in the diffuser that transitions the combustor output to the turbine. Historically, these losses have more than cancelled the pressure gains generated in the combustion process itself.

The successful demonstration of sustained detonation with low injector pressure loss is, therefore, a significant advancement of RDE technology. The injector design developed in this project is the launching point for additional research into low-loss technology. Follow-on work could expand the operability and strengthen the detonation while retaining low losses. Such a second-generation design would then enable an operational RDE system, pending similar advancements in diffuser and turbine integration technology. This operational system could deliver on the promise of pressure gain combustion, namely higher efficiency gas turbines. This work brings that goal one step closer.

The injector fatigue test points to some success in the project's primary goal of successfully developing and applying the DTMM to a component design. Implementing the DTMM recommendations for optimal processing parameters led to a part with acceptable properties. The DTMM was also shown to be an efficient correlator of data and to provide insight on the relationship between process settings, microstructure, and property performance. However, the failure of the DTMM prediction to match the experimental result of the injector fatigue test and its limited accuracy in cross-validation also points to the need to include significantly more data in the model development.

As shown in the DTMM update, model predictions change and improve as more data is considered. In this project, coupons made with identical processing parameters exhibited drastically different properties from each other and from the injector part, which clearly influences the accuracy of a model that predicts performance based on parameters. Uncertainties in the build process must be quantified to develop more robust models. A denser and broader matrix of coupon process and geometry variations, several repeated builds of every point, more in-situ build process measurements, and direct observation of tensile and HCF sample microstructure (as opposed to separate microstructure specimens) are recommendations to improve future AM modeling efforts.

5. REFERENCES

[1] Abioye, T E, J Folkes, and A T Clare. 2013. “Journal of Materials Processing Technology A Parametric Study of Inconel 625 Wire Laser Deposition.” *Journal of Materials Processing Tech.* 213 (12): 2145–51. https://doi.org/10.1016/j.jmatprotec.2013.06.007.

[2] Alexandre, F., S. Deyber, and A. Pineau. 2004. “Modelling the Optimum Grain Size on the Low Cycle Fatigue Life of a Ni Based Superalloy in the Presence of Two Possible Crack Initiation Sites.” *Scripta Materialia* 50 (1): 25–30. https://doi.org/10.1016/j.scriptamat.2003.09.043.

[3] Anam, Ashabul. 2018. “Microstructure and Mechanical Properties of Selective Laser Melted Superalloy Inconel 625.” University of Louisville.

[4] Arisoy, Yigit M, Luis E Criales, and Tugrul Ozel. 2019. “Modeling and Simulation of Thermal Fi Eld and Solidi Fi Cation in Laser Powder Bed Fusion of Nickel Alloy IN625.” *Optics and Laser Technology* 109: 278–92. https://doi.org/10.1016/j.optlastec.2018.08.016.

[5] Arisoy, Yigit M, Luis E Criales, Tugrul Ozel, Brandon Lane, Shawn Moylan, and Alkan Donmez. 2017. “Influence of Scan Strategy and Process Parameters on Microstructure and Its Optimization in Additively Manufactured Nickel Alloy 625 via Laser Powder Bed Fusion.” *International Journal of Advanced Manufacturing Technology* 90: 1393–1417. https://doi.org/10.1007/s00170-016-9429-z.

[6] Avery, D.Z., O.G. Rivera, C.J.T. Mason, B.J. Phillips, J B Jordon, J Su, N Hardwick, and P G Allison. 2018. “Fatigue Behavior of Solid-State Additive Manufactured Inconel.” *Journal of Materials* 70 (11): 2475–84. https://doi.org/10.1007/s11837-018-3114-7.

[7] Bellows, R. S., S. Muju, and T. Nicholas, "Validation of the step test method for generating Haigh diagrams for Ti–6Al–4V." *International Journal of Fatigue* 21 (7): 687-697, 1999.

[8] Carter, Luke N, Moataz M Attallah, and Roger C Reed. 2012. “Laser Powder Bed Fabrication of Nickel-Base Superalloys: Influence of Parameters; Characterisation , Quantification and Mitigation of Cracking.” In *Superalloys 2012*, 577–86.

[9] Cecen, A., T. Fast, and S. R. Kalidindi, "Versatile algorithms for the computation of 2-point spatial correlations in quantifying material structure." *Integrating Materials and Manufacturing Innovation* 5 (1): 1-15, 2016.

[10] Composition, Chemical. n.d. “Ni 58, 69,” no. Alloy 625.

[11] Composition, Limiting Chemical, Publication Number Smc-, Special Metals Corporation, and Special Metals Corporation. 2013. “INCONEL Alloy 625.” *www.Specialmetals.Com* 625 (2): 1–28. https://doi.org/SMC-066.

[12] Criales, Luis E, Yigit M Arisoy, Brandon Lane, Shawn Moylan, Alkan Donmez, and Tugrul Ozel. 2017. “Laser Powder Bed Fusion of Nickel Alloy 625 : Experimental Investigations of e Ff Ects of Process Parameters on Melt Pool Size and Shape with Spatter.” *International Journal of Machine Tools and Manufacture* 121 (September 2016): 22–36. https://doi.org/10.1016/j.ijmachtools.2017.03.004.

[13] Debroy, T, H L Wei, J S Zuback, T Mukherjee, J W Elmer, J O Milewski, A M Beese, A Wilson-heid, A De, and W Zhang. 2018. “Progress in Materials Science Additive Manufacturing of Metallic Components – Process, Structure and Properties.” *Progress in Materials Science* 92: 112–224. https://doi.org/10.1016/j.pmatsci.2017.10.001.

[14] Dinda, G P, A K Dasgupta, and J Mazumder. 2012. “Texture Control during Laser Deposition of Nickel-Based Superalloy.” *Scripta Materialia* 67 (5): 503–6. https://doi.org/10.1016/j.scriptamat.2012.06.014.

[15] Dinda, G P, A K Dasgupta, and J Mazumder. 2009. “Laser Aided Direct Metal Deposition of Inconel 625 Superalloy: Microstructural Evolution and Thermal Stability.” *Materials Science & Engineering A* 509: 98–104. https://doi.org/10.1016/j.msea.2009.01.009.

[16] Eiselstein, H L, and D J Tillack. 1991. “The Invention and Definition of Alloy 625.” In *Superalloys 718, 625, and Various Derivatives*, edited by Edward A. Loria, 1–14.

[17] Fullwood, D. T., S. R. Niezgoda, B. L. Adams, and S. R. Kalidindi, "Microstructure sensitive design for performance optimization." *Progress in Materials Science* 55 (6): 477-562, 2010.

[18] Ganesh, P, R Kaul, C P Paul, Pragya Tiwari, S K Rai, R C Prasad, and L M Kukreja. 2010. “Fatigue and Fracture Toughness Characteristics of Laser Rapid Manufactured Inconel 625 Structures.” *Materials Science & Engineering A* 527 (29–30): 7490–97. https://doi.org/10.1016/j.msea.2010.08.034.

[19] Gorgannejad, S. "Data-Driven Process-Structure-Property Models for Additive Manufactured Ni-base Superalloy.," PhD Dissertation, Georgia Institute of Technology, 2020

[20] Graybill, Benjamin, Ming Li, David Malawey, Chao Ma, Juan-Manuel Alvarado-Orozco, and Enrique Martinez-franco. 2018. “Additive Manufacturing of Nickel-Based Superalloys.” In *Proceedings of ASME 2018 13th International Manufacturing Science and Engineering Conference*, 1–17. College Station, TX, USA.

[21] Koutiri, Imade, Etienne Pessard, Patrice Peyre, Ouafae Amlou, Thibaut De, Imade Koutiri, Etienne Pessard, Patrice Peyre, Ouafae Amlou, and Thibaut De Terris. 2018. “Influence of SLM Process Parameters on the Surface Finish, Porosity Rate and Fatigue Behavior of as-Built Inconel 625 Parts To Cite This Version: HAL Id : Hal-01826611.” *Journal of Materials Processing Tech.* 255: 536–46. https://doi.org/10.1016/j.jmatprotec.2017.12.043.

[22] Lass, Eric A, Mark R Stoudt, Maureen E Williams, Michael B Katz, Lyle E Levine, Thien Q Phan, Thomas H Gnaeupel-herold, and Daniel S Ng. 2017. “Formation of the Ni 3 Nb Delta - Phase in Stress-Relieved Inconel 625 Produced via Laser Powder-Bed Fusion Additive Manufacturing.” *Metallurgical and Materials Transactions A* 48 (11): 5547–58. https://doi.org/10.1007/s11661-017-4304-6.

[23] Lewandowski, John J., and Mohsen Seifi. 2016. “Metal Additive Manufacturing: A Review of Mechanical Properties.” *Annual Review of Materials Research* 46 (1): 151–86. https://doi.org/10.1146/annurev-matsci-070115-032024.

[24] Marchese, By Giulio, Xabier Garmendia Colera, Flaviana Calignano, Massimo Lorusso, Sara Biamino, Paolo Minetola, and Diego Manfredi. 2016. “Characterization and Comparison of Inconel 625 Processed by Selective Laser Melting and Laser Metal Deposition **.” *Advanced Engineering Materials* 19 (3): 1–9. https://doi.org/10.1002/adem.201600635.

[25] Montgomery, Colt, Jack Beuth, Luke Sheridan, and Nathan Klingbeil. 2015. “Process Mapping of Inconel 625 in Laser Powder Bed Additive Manufacturing.” In *Solid Freeform Fabrication 2015*, 1195–1204. Austin, TX, USA.

[26] Niezgoda, S. R., D. T. Fullwood, and S. R. Kalidindi, "Delineation of the space of 2-point correlations in a composite material system." *Acta Materialia* 56 (18): 5285-5292, 2008.

[27] Poulin, J, V Brailovski, and P Terriault. 2018. “Long Fatigue Crack Propagation Behavior of Inconel 625 Processed by Laser Powder Bed Fusion: In Fl Uence of Build Orientation and Post-Processing Conditions.” *International Journal of Fatigue* 116 (July): 634–47. https://doi.org/10.1016/j.ijfatigue.2018.07.008.

[28] Puppala, Ganesh, Aniruddha Moitra, S Sathyanarayanan, Rakesh Kaul, G Sasikala, Ram Chandra Prasad, and Lalit M Kukreja. 2013. “Evaluation of Fracture Toughness and Impact Toughness of

Laser Rapid Manufactured Inconel-625 Structures and Their Co-Relation." In *13th International Conference on Fracture*. Beijin, China.

[29] United States Department of Defense. 1998. "Military Handbook: Metallic Materials and Elements for Aerospace Vehicle Structures." MIL-HDBK-5H.

[30] Zhang, Fan, Lyle E. Levine, Andrew J. Allen, Mark R. Stoudt, Greta Lindwall, Eric A. Lass, Maureen E. Williams, Yaakov Idell, and Carelyn E. Campbell. 2018. "Effect of Heat Treatment on the Microstructural Evolution of a Nickel-Based Superalloy Additive-Manufactured by Laser Powder Bed Fusion." *Acta Materialia* 152: 200–214. https://doi.org/10.1016/j.actamat.2018.03.017.